

AFRL-SN-RS-TR-2004-125
Final Technical Report
May 2004



OPTO-ELECTRONIC AND INTERCONNECTS HIERARCHICAL DESIGN AUTOMATION SYSTEM (OE-IDEAS)

CFD Resesarch Corporation

APPROVED FOR PUBLIC RELEASE; DISTRIBUTION UNLIMITED.

**AIR FORCE RESEARCH LABORATORY
SENSORS DIRECTORATE
ROME RESEARCH SITE
ROME, NEW YORK**

STINFO FINAL REPORT

This report has been reviewed by the Air Force Research Laboratory, Information Directorate, Public Affairs Office (IFOIPA) and is releasable to the National Technical Information Service (NTIS). At NTIS it will be releasable to the general public, including foreign nations.

AFRL-SN-RS-TR-2004-125 has been reviewed and is approved for publication

APPROVED: /s/

JAMES NICHTER
Project Engineer

FOR THE DIRECTOR: /s/

RICHARD G. SHAUGHNESSY, Lt. Col., USAF
Chief, Rome Operations Office
Sensors Directorate

REPORT DOCUMENTATION PAGE			<i>Form Approved</i> <i>OMB No. 074-0188</i>	
Public reporting burden for this collection of information is estimated to average 1 hour per response, including the time for reviewing instructions, searching existing data sources, gathering and maintaining the data needed, and completing and reviewing this collection of information. Send comments regarding this burden estimate or any other aspect of this collection of information, including suggestions for reducing this burden to Washington Headquarters Services, Directorate for Information Operations and Reports, 1215 Jefferson Davis Highway, Suite 1204, Arlington, VA 22202-4302, and to the Office of Management and Budget, Paperwork Reduction Project (0704-0188), Washington, DC 20503				
1. AGENCY USE ONLY (Leave blank)		2. REPORT DATE MAY 2004	3. REPORT TYPE AND DATES COVERED Final Jun 01 – Dec 03	
4. TITLE AND SUBTITLE OPTO-ELECTRONIC AND INTERCONNECTS HIERARCHICAL DESIGN AUTOMATION SYSTEM (OE-IDEAS)			5. FUNDING NUMBERS C - F30602-01-2-0552 PE - 62712E PR - M064 TA - SN WU - 01	
6. AUTHOR(S) M. Turowski, A. Przekwas, R. Tramel, H. Q. Yang, H. Ding, Z. Sikorski, Y. Jiang, M. Furmanczyk, A. Fedoseyev, P. Wilkerson, A. Raman, T. Czystanowski, S. M. Kang, S. Wu, F. Kiamilev, X. Wang, and E. Kan				
7. PERFORMING ORGANIZATION NAME(S) AND ADDRESS(ES) CFD Research Corporation 215 Wynn Drive Huntsville Alabama 35805			8. PERFORMING ORGANIZATION REPORT NUMBER N/A	
9. SPONSORING / MONITORING AGENCY NAME(S) AND ADDRESS(ES) Air Force Research Laboratory/SNDP 25 Electronic Parkway Rome New York 13441-4515			10. SPONSORING / MONITORING AGENCY REPORT NUMBER AFRL-SN-RS-TR-2004-125	
11. SUPPLEMENTARY NOTES AFRL Project Engineer: James Nichter/SNDP/(315) 330 7423/ James.Nichter@rl.af.mil				
12a. DISTRIBUTION / AVAILABILITY STATEMENT APPROVED FOR PUBLIC RELEASE; DISTRIBUTION UNLIMITED.				12b. DISTRIBUTION CODE
13. ABSTRACT (Maximum 200 Words) As microelectronics technology continues to advance, the associated electrical interconnection technology is not likely to keep pace, due to many parasitic effects appearing in metallic interconnections. Hence, the optical interconnections and photonic-electronic chips seem to be the most viable technology for future multi-GHz mixed-signal electronics. Therefore, this project developed, demonstrated, and validated Design Tools for Opto-Electronic Integrated Circuits and Interconnects. The two crucial issues are the efficient and fast techniques of extraction of parasitics as well as revolutionary new methods of modeling parasitics in electrical interconnects, where high-frequency electromagnetic effects will not allow for using SPICE-type models anymore, and the new, comprehensive CAD tools for integrated opto-electronic (O/E) circuits and systems, which would allow designers to analyze and optimize the full-path signal characteristics, at all the stages of the optically communicating circuits.				
14. SUBJECT TERMS Modeling, Parasitics, Automated Synthesis, Opto-Electronic, O/E, Integrated Circuits, Computer Aided Design, CAD, Electromagnetic, EM, Simulation, Photonic, 3D Modeling				15. NUMBER OF PAGES 135
				16. PRICE CODE
17. SECURITY CLASSIFICATION OF REPORT UNCLASSIFIED	18. SECURITY CLASSIFICATION OF THIS PAGE UNCLASSIFIED	19. SECURITY CLASSIFICATION OF ABSTRACT UNCLASSIFIED	20. LIMITATION OF ABSTRACT UL	

TABLE OF CONTENTS

1	INTRODUCTION.....	1
1.1	BACKGROUND.....	1
1.2	PROJECT MOTIVATION	2
1.3	PROJECT OBJECTIVES AND SCOPE	3
1.4	SUMMARY OF ACCOMPLISHMENTS.....	5
2	OPTO-ELECTRONIC DEVICE MODELS CONSOLIDATION FOR BEHAVIOR MODEL EXTRACTION	8
2.1	ENHANCEMENT OF HIGH-FIDELITY ELECTRO-OPTICAL VCSEL MODEL	8
2.2	COUPLED MULTIPHYSICS MODELING OF SEMICONDUCTOR LASERS	10
2.3	QUANTUM MECHANICAL MODEL ENHANCEMENT OF ELECTRONIC AND PHOTONIC DEVICES	13
3	IMPLEMENTATION OF HIGH ACCURACY ROBUST 3-D EM SOLVERS.....	16
3.1	FINITE-DIFFERENCE TIME-DOMAIN (FDTD) SOLVER: CFD-MAXWELL.....	16
3.1.1	<i>FDTD Solver Adaptation and Verification for RF Interconnects</i>	<i>16</i>
3.1.2	<i>FDTD Solver Applications for Optical Modeling.....</i>	<i>25</i>
3.2	FINITE-VOLUME MAGNETIC-VECTOR-POTENTIAL BASED 3D SOLVER: EMAG	28
3.2.1	<i>EMAG Solver Modifications (Voltage, Current, Impedance, S-Parameters)</i>	<i>28</i>
3.2.2	<i>Coupling of 3D EMAG Simulator with SPICE</i>	<i>29</i>
3.2.3	<i>3D EMAG Simulation of a Parasitic Hanging Stub at Vias in RF PCB Interconnects</i>	<i>33</i>
4	IMPLEMENTATION OF FILAMENT AND WIRE MODELS	37
4.1	LOCAL SUBCELL MODEL OF FILAMENT IN ELECTROMAGNETIC MODULE	37
4.2	MODELING OF INTERACTION BETWEEN FILAMENT AND 3D EM FIELD	45
5	AUTOMATIC 3D MODELING AND MESHING FROM IC LAYOUTS: CFD-MICROMESH	49
6	VHDL-AMS COMPACT MODELS OF O/E DEVICES	56
6.1	VCSEL AND TRANSMITTER (VCSEL AND A CMOS DRIVING CIRCUIT)	56
6.2	METAL-SEMICONDUCTOR-METAL (MSM) PHOTODETECTOR	57
6.3	RAMAN AMPLIFIER	57
6.4	ERBIUM DOPED FIBER AMPLIFIER (EDFA)	57
7	DESIGN AND FABRICATION OF TEST STRUCTURES AND VALIDATION FOR RF INTERCONNECTS AND OPTO-ELECTRONIC SYSTEMS	57
7.1	DESIGN, FABRICATION, AND TESTING OF OE AND RF CHIPS AND PCBs	57
7.2	CHARACTERIZATION AND MODELING OF ON-CHIP INTERCONNECT WITH REALISTIC LOADS AND DRIVES...62	62
8	NEOCAD TEST STRUCTURES AND BENCHMARKS SIMULATIONS.....	71
8.1	NEOCAD BENCHMARKS FROM THE DAVINCI NETBOOK WEBSITE.....	71
8.2	SIMULATION OF CRITICAL PATH FROM THE MAYO “10G” SYSTEM MCM BOARD	80
9	CONCLUSIONS, COMMERCIALIZATION, TECHNOLOGY TRANSFER	88
9.1	CONCLUSIONS AND SUMMARY OF ACHIEVEMENTS	88
9.2	COMMERCIALIZATION AND TECHNOLOGY TRANSFER	90
9.3	RECOMMENDATIONS AND PLANS FOR FURTHER RESEARCH.....	95
10	REFERENCES.....	95
10.1	PUBLICATIONS RESULTING FROM THIS PROJECT.....	95
10.2	OTHER REFERENCES	97
	APPENDIX A - Compact Model Extraction for Opto-Electronic Devices.....	99

TABLE OF FIGURES

Figure 1. SPICE-type equivalent-circuit models of ULSI ICs, interconnects, and mixed-signal RF circuits become computationally inefficient and often prohibitive for higher frequencies.	2
Figure 2. Example of a hybrid 3D opto-electronic design with a communication waveguide.	3
Figure 3. Extended Design Flow of electrical-optical circuits and printed circuit boards, with indicated scope of this project.	4
Figure 4. Examples of photonic VLSI integrated circuits and interconnections for future high-bandwidth communication systems, developed under DARPA FSOI and VLSI Photonics programs.	5
Figure 5. Parasitic Extraction of 100 GHz InP circuit, a NeoCAD benchmark from Mayo.	6
Figure 6. Extraction of OE behavioral models for mixed-level system simulation.	8
Figure 7. High-fidelity multiple Quantum Well (QW) model.	9
Figure 8. Energy Band Diagram of the Multiple-QW structure.	10
Figure 9. Carrier Density near the Multiple-QW structure.	10
Figure 10. Current flow and electron density distributions inside an intra-cavity VCSEL device.	12
Figure 11. Transient behavior of multi-transverse-mode VCSEL. Photon numbers in single modes and total number of photons in the cavity.	12
Figure 12. Steady-state radial distribution of intensity in different transverse modes for VCSEL with 6 micrometer oxide aperture.	12
Figure 13. Steady-state axial distribution of intensity in transverse modes for VCSEL with 6 micrometer oxide aperture.	12
Figure 14. Selected snapshots of transient behavior of total optical intensity during the multi-transverse-mode VCSEL switching (cf. Figure 11).	12
Figure 15. Quantum transport modeling procedure, and sample results of the stress tensor in a tunneling barrier under equilibrium (0 V) and 1 V bias.	15
Figure 16. The coupled microstrip line. The strips are 0.05 by 0.3 mm and separated by 0.3 mm, the dielectric slab is 0.25 mm thick and has a relative dielectric constant ϵ_r of 4.5.	16
Figure 17. Propagation of an even mode Gaussian pulses (Pulse Width 10^{-11} s) along a coupled microstrip line.	17
Figure 18. CFD-Maxwell impedances for even and odd mode excitation in a frequency range between 5GHz and 25GHz in comparison with the results from Becker, Harm and Mittra (<i>IEEE Trans. on MTT</i> , 1992)	17
Figure 19. Test case of interconnects: five-line signal bus over a ground mesh (a) and its transfer function from near to far end node of leftmost signal line, calculated with different equivalent circuit models in [Beattie, 2000].	18
Figure 20. Our meshed model of the solid (Cu) parts of the 5-line bus interconnects from Figure 19a. The mesh was built automatically in CFD-Micromesh within a few seconds.	19

Figure 21. Two cross-sections showing meshed insulator parts of the 5-line interconnect structure (the copper parts are blanked for better visualization). The full mesh, built automatically in CFD-Micromesh, has about 46,000 cells.	19
Figure 22. Several selected snapshots from CFD-Maxwell transient simulation of a propagating Gaussian pulse of 1ps width, after 1000 time steps (5 ps of the simulated time), 1500 steps (7.5 ps), 2000 steps (10 ps), and 2500 steps (12.5 ps). The last snapshot shows a reflected wave from the un-matched line termination.	20
Figure 23. Voltages (left plot) and currents (right plot) varying in time in the middle line of the 5-line bus, with a short circuit ($R=0$) at the line termination. The values were monitored at the near end of the line ($v1$ and $i1$, at 0.1 of the length – red curves) and at the far end of the line ($v2$ and $i2$, at 0.9 of the length – green curves). 1000 time steps corresponds to 5 ps of simulated time.	21
Figure 24. Time-dependent voltages (left) and currents (right) in the middle line of the 5-line bus, with a matching impedance ($R = 38.7 \Omega$) at the line termination.	21
Figure 25. Time-dependent voltages (left) and currents (right) in the middle line of the 5-line bus, with a matching impedance ($R = 38.7 \Omega$) at the line termination, with a trapezoidal pulse applied to the input of the middle line. 1000 time steps corresponds to 5 ps of simulated time.	21
Figure 26. Plot of S-parameters calculated from the transient simulation of Gaussian pulse.	22
Figure 27. Time-dependent voltages (left) and currents (right) in the middle line of the 5-line bus, with a 10ps-wide Gaussian pulse (a) and 10ps-wide trapezoidal pulse (b) applied to the input of the middle line. On the time scale, 1000 time steps corresponds to 5 ps of simulated time.	23
Figure 28. Example of five parallel signal lines driven by resistive voltage sources and terminated by load capacitances.	24
Figure 29. Theoretical transient response of a transmission line with a characteristic impedance of 50Ω , loaded by a capacitance of 2 pF, to an applied step voltage of 5V.	24
Figure 30. CFD-Maxwell results for a transmission line with capacitive termination: time dependent voltages (left) and currents (right).	25
Figure 31. TM wave propagation test in 2D domain, $\lambda / \Delta x = 12$ [Δx = cell edge length], solver in total field formulation mode, $E_z(x,y)$ plotted at arbitrary time, Left: unstructured mesh, left and right boundary ABC, strong distortion of wave fronts; Right: unstructured mesh + Cartesian buffer zone, left and right boundary: extrapolation, wave fronts are preserved.	26
Figure 32. TM wave propagation test in narrowing 2D domain, $\lambda / \Delta x \approx 20$, wave fronts are preserved.	26
Figure 33. Initial TM wave scattering test on a dielectric square with $\epsilon_r=4$, solver in total field formulation mode.	26
Figure 34. Scattering of a plane electromagnetic wave on an infinite dielectric cylinder with $\epsilon_r=4$, diameter d (normal incident, TM^z polarization, +x-propagation); $\lambda/d=1.5$; (solver in scattered field mode, scattered field plotted) left: FDTD simulation, contour plot of $ E^s(r, \phi, 2\pi \tau/T) $ at constant, random phase angle τ after steady state is reached; middle: 2D mapping of the analytical solution for	

	$ E^s(r, \phi, 2\pi \tau/T) $ at same phase angle; right: surface plot of analytical solution for $ E^s(r, \phi, 2\pi \tau/T) $	27
Figure 35.	Left: Comparison of analytical and FDTD solution for $E_z^s(x) _{y=0}$; middle: FDTD simulation, contour plot of total field $ E^t(r, \phi, 2\pi \tau/T) $; right: 2D mapping of the analytical solution for total field $ E^t(r, \phi, 2\pi \tau/T) $	27
Figure 36.	Scattering of a plane electromagnetic wave on an infinite PEC cylinder with diameter d (normal incident, TE^z polarization, +x-propagation); $\lambda/d=1.5$; (solver in scattered field mode, scattered field plotted) left: FDTD simulation, contour plot of $ _sB(r, \phi, 2\pi \tau/T) $ at constant, random phase angle τ after steady state is reached; middle: comparison of analytical and FDTD solution for $_sB_z(x) _{y=0}$ at same phase angle; right: 2D mapping of the analytical solution for $ _sB(r, \phi, 2\pi \tau/T) $	27
Figure 37.	3D FDTD simulation of the scattering of a TM^x plane wave packet (propagating in +z direction coming from the bottom of the image, gray area) through a 2×2 square aperture array (each aperture's size is $\lambda \times \lambda$); walls: contour plot of $ E^t(x, y, z, t) $, volume: iso-surfaces of $ E^t(x, y, z, t) =0.4V/m$ illustrating the beam-lets exiting the apertures, notice the formation of the main diffraction maxima in the middle.....	28
Figure 38.	Schematic illustrating voltage lines, current loops, and current faces (basic equations for voltage, current, and impedance are included).	29
Figure 39.	Illustration of the coupling mechanism of CFDR3D EMAG simulator with SPICE.....	30
Figure 40.	Flow-chart of the SPICE to ACE+EMAG coupling algorithm.....	31
Figure 41.	An example of a 3D EMAG model of a transmission line with SPICE modeling the source (driver) and the line termination.....	32
Figure 42.	Schematic side-view drawing of a PCB via with hanging stub.....	33
Figure 43.	Measured transfer characteristics (S21) of via with hanging stub [ISSC 2003]. The resonance dip in the blue curve is caused by a long (240 mils) hanging via.....	33
Figure 44.	Layout of two transmission lines and via (similar to Fig. 1), drawn in Micromesh.	34
Figure 45.	A fragment of the 3D meshed computational model generated by Micromesh. There is a ground plane between signal traces 1 and 2, not shown in Figure 42.....	35
Figure 46.	The model of via with the hanging stub (240 mils), with overlaid results of the electric potential distribution at $t = 1$ ns, calculated by transient EMAG simulation. The ground plane and dielectric materials are not shown here for better visibility of the transmission lines.	36
Figure 47.	Comparison of the S21 transfer characteristics for the cases without-stub and with-stub, calculated from the full-wave transient results of EMAG simulator from CFDR3D.....	37
Figure 48.	Computational Model of a Conductive Wire in Time Varying Magnetic Field	39
Figure 49.	Distribution of a Magnetic Vector Potential Around a Conducting Wire under a Time Varying Magnetic Field.....	40
Figure 50.	Comparison of Field with Wire Treated as (a) Perfect Conductor and (b) Lossy Conductor	41

Figure 51. Computational Model for a Straight Wire.....	44
Figure 52. Magnetic Vector Around a Current Carrying Wire.....	44
Figure 53. Comparison of Magnetic Field.....	45
Figure 54. a) Distribution of voltage due to conduction current in a wire. b) Magnetic field vectors resulting from the conduction current in a wire.	46
Figure 55. A geometrical setup to investigate inductive influence of one wire on its neighbors.....	46
Figure 56. Computed current vectors induced by the current flow in the top wire.	47
Figure 57. Typical magnetic field induced by one of 3 wires in a transmission line.	48
Figure 58. Comparison of simulation results of magnetic fields along x-axis for 5 cases of single- and multi-filament models, with fine and coarse grids.....	48
Figure 59. Example from the new Micromesh Tutorial, the Spiral Transformer (built of two spiral inductors): two separate GDSII layouts imported into Micromesh from <i>coupled.gds</i> file provided by NCSU as a NeoCAD benchmark.	50
Figure 60. 3D solid model of the NCSU Spiral Transformer, built automatically from layout in Micromesh.	51
Figure 61. 3D prism-hex mesh built automatically from layout in Micromesh.	51
Figure 62. Overall progress of the CFD-Micromesh tool during the DARPA NeoCAD program.....	54
Figure 63. NeoCAD Benchmark layout: UW-SOI-QVCO from University of Washington.	55
Figure 64. The UW-SOI-QVCO benchmark 3D model, automatically built from the GDSII layout, using the new Micromesh capabilities.	55
Figure 65. A 3D structured mesh generated automatically by Micromesh from UW layout.....	56
Figure 66. Chip with Bonding Wires.....	58
Figure 67. Mayo 10G system MCM layout, in Cadence-Allegro (left) and CFD-Micromesh (right).	60
Figure 68. Dual-Rate Current Mode Logic Electrical Interconnects test chip.	62
Figure 69. Interconnect structures fabricated in Cornell Nanofab.....	63
Figure 70. Results of initial measurements of the interconnect structures fabricated at Cornell University.....	63
Figure 71. Approximation of input waveform.....	64
Figure 72. Measured and simulated results. (a) Output power. The square is the simulated points, and the triangles are measured points; (b) Simulated output voltage waveforms.	64
Figure 73. An interconnect circuit with an input power source, an input network with s-parameter S_{in} , and an output network with S_{out} . Z_s is the source impedance. The input and output networks provide connections between the power source and the load. Γ_s and Γ_L denote the source and load reflection coefficient in the frequency domain.....	65
Figure 74. Approximation of input waveform.	66
Figure 75. (a) A signal flow graph of the circuit in Fig. 1. A Z_0 (reference impedance of the s-parameters) is splitted from the source impedance, Z_s , in Fig.1. The rest of the sources impedance is combined with the input network, and represented by S_{in} . The separation is not necessary, but convenient for analysis formula	

simplifications. (b) Simplified signal flow graph by cascading the s -parameters of all the elements in (a).	67
Figure 76. A flow chart of the frequency-domain algorithm.	68
Figure 77. (a) Schematic of the magnetic coupling test structures; (b) part of the fabricated test structures	70
Figure 78. S_{12} of the coupled transmission lines.	71
Figure 79. Layouts of several test structures on the Mayo test chip “ic_hrl_tc1”.	72
Figure 80. Layout of the CP1 structure, imported in CFD-Micromesh from GDSII file, and the computational grid generated automatically by CFD-Micromesh from the layout.	73
Figure 81. An example snapshot of steady-state electric simulation results of CFD-ACE+, with 3.3 V applied to the ground pads A and C, and zero volts to all the other pads.	74
Figure 82. Simulated Gaussian Pulse Propagation in Time in the CP1 Benchmark Structure.	75
Figure 83. Voltage and Current Monitors at the CP1 line beginning (red) and end (green).	76
Figure 84. Measured and Calculated S-Parameters for the CP1 Test Structure.	76
Figure 85. The 2OG test structure from NCSU-B2B: basic parameters and cross-section photo.	77
Figure 86. Computational mesh built in CFD-Micromesh for 2OG structure from NCSU.	78
Figure 87. S-parameters computed by CFD-Maxwell for the 2OG structure.	79
Figure 88. S-parameters of the 2OG structure, measured by NCSU.	79
Figure 89. Sketch of the “10G” FSOI System, accepted as the NeoCAD benchmark. The MCM board is at the bottom.	80
Figure 90. 10G MCM board layout (4 chips = 4 clusters of SPAs).	81
Figure 91. Single chip layout on the 10G MCM board.	82
Figure 92. Some signal traces in the layer “signal_2 chip_U4”	83
Figure 93. The C4out signal-path layout, and a 3D model built in Micromesh.	84
Figure 94. Mesh details of the C4out Line, with static differential electric potential	85
Figure 95. Snapshot of the steady-state electric simulation results from CFD-ACE+, with +3 V and -3 V applied to the differential lines C4out and N_C4out.	86
Figure 96. Several selected snapshots of that transient simulation for a differential signal (Gaussian pulse) of +0.4 and -0.4 volt applied to the input of the differential lines C4out and N_C4out.	88
Figure 97. Analog/RF Design Flow with related Orora tools, and the new <i>Coupled EM+Circuit</i> tools to be implemented in the next CFDRC SBIR project (starting Spring 2004).	91

ACKNOWLEDGEMENTS

During the course of this project, the authors received help, encouragement and advice from a number of individuals without which this project would not have been a success.

The authors would like to thank the DARPA NeoCAD Program Manager, Dr. Anantha Krishnan, for his support, guidance, and patience, and also Mr. Greg Creech for his guidance and helpful suggestions. Thanks are also due to Mr. Norman Bernstein of AFRL Rome Labs for his work in the role of the progress monitor and for helpful suggestions for improvements.

This work would not have been possible without the extensive support and help provided by a number of CFDRC personnel. Thanks are due to Dr. Ashok Singhal for technical direction and help in synergizing this effort with other programs. Various individuals provided valuable help with different aspects of the projects: Dr. Bill Coirier with the DTF libraries and new DTF functions, Dr. Sami Bayyuk with the electromagnetic solver, Dr. Hui Ding with the filament models, and Dr. Z. J. Chen with the ACE+ parametric procedures. Software group personnel, including Mr. Richard Thoms, Mr. Winston Jiang, and Mr. Fanglin Zhu helped out with GUI and software control. Finally, the Graphics group worked on the pre- and post-processing tools, including CFD-VIEW, and thanks are due to Drs. Vincent Harrand, Jerone Van der Zijp, and Mr. Vadim Uchitel and others.

A number of people from various academic and industrial organizations supplied us with advice on RF circuit and device design, as well as data of optoelectronic/photonic structures for code validation and testing. They include University of Washington (Prof. R. Shi, Prof. V. Jandhyala, Dr. P. Nikitin), SUNY (Prof. A. Pacelli), Georgia Tech (Prof. G. Cassinovi), Univ. of Cincinnati (Prof. R. Vemuri), Univ. of Illinois Urbana-Champaign (Prof. A. Cangellaris), NCSU (Prof. M. Steer), Rockwell Scientific (Dr. R. Chow), Mixed Technology Associates (Dr. D. Yergeau), LSI Logic (Dr. K. Doniger), Eastman Kodak (Dr. E. Furlani), and Agilent R&D Center (Dr. D.Burak).

The authors also wish to thank the OE-IDEAS academic partners from University of Delaware (Dr. Fouad Kiamilev, Mr. Xingle Wang), UC Santa Cruz (Prof. Steve Kang, Mr. Shu Wu), and Cornell University (Prof. Edwin Kan) for valuable inputs and fruitful collaboration during the three years of this joint project.

1 INTRODUCTION

1.1 Background

This project was a team effort, originally scheduled two years, from July 2001 to June 2003, then extended till 12/31/2003, led by CFD Research Corporation (CFDRC), with participation of University of California Santa Cruz (UCSC), Cornell University (CU), and University of Delaware (UD).

The objective of this project was to develop, demonstrate, and validate Design Tools for Opto-Electronic Integrated Circuits and Interconnects. The new tools include several innovative ideas in the following Technical Areas:

- EDA Interfaces and Front End for Automation,
- Efficient Extraction of Parasitics in Electrical Interconnects,
- New Methods of Electrical Interconnects Modeling for High Frequencies,
- New Methods of Optical Interconnects Modeling,
- Model-Order Reduction and Behavioral Models for Electronic-Photonic Devices and Circuits,
- Integration of the New Methods and Software into EDA Tools for Opto-Electronic (O/E) Design Flow and Automated Synthesis.

Major activities in this program were organized to take advantage of the expertise of all the team members and their respective PI's:

- **CFDRC** (Dr. Marek Turowski, Dr. Andrzej Przekwas, Dr. Robert Tramel, Dr. H.Q Yang): Computational Microelectronics, Semiconductor Physics, Electromagnetics, Photonics, O/E Interconnects, Computational Physics, Appl. Math.; Numerical Methods and Algorithms, Multi-Disciplinary CAD, TCAD, project coordination, software development, validation, demonstration and applications.
- **University of California Santa Cruz** (Dr. Steve Kang): VLSI CAD; High-performance VLSI Systems; Modeling and simulation of high-speed electronic and optoelectronic integrated circuits and systems; Reduced/behavioral models of O/E devices and systems.
- **Cornell University** (Dr. Edwin Kan): Nanoscale electronic devices and interconnects; Technology CAD and intelligence abstraction for VLSI systems; Computational quantum-electronics for quantum-well photonic devices.
- **University of Delaware** (Dr. Fouad Kiamilev): Design and Test of high-performance Digital and Analog CMOS and BiCMOS VLSI Circuits for: Photonics, Optoelectronic Integrated Circuits (OEIC), and Optoelectronic VLSI; RF IC Design, Fabrication and Measurements for Verification and Validation the newly developed software.

This report documents the work performed during the 30 months of the project.

1.2 Project Motivation

Decreasing feature sizes of very deep submicron ULSI (Ultra Large Scale Integration) as well as increased operating frequencies of mixed-signal (digital/analog/RF) and mixed-technology (electronics, photonics, etc.) systems make it necessary to precisely predict parasitic as well as intended electromagnetic (EM) and optical effects of interconnects. Equally important becomes the accurate simulation of the interaction between active devices (MOSFETs, VCSELs, etc.) and interconnects.

High-frequency and high-bandwidth circuits can only be achieved through nano-scale devices due to the upper limit of information propagation speed. Above 30GHz, the wavelength of EM waves becomes 1cm, and the distinction between processing unit (on the order of 2cm chip) and transmission units (antenna or optical fiber connection) becomes blurred. To support new system design in this domain, not only the CAD system needs to deal with the ever-increasing complexity and component interconnect coupling, but also new nano-scale effects need to be included in a more rigorous and universal way. It is then possible to integrate the nonlinear characteristics into the system design validation and optimization.

Limitations of the methods and tools existing before NeoCAD Program:

- Few EM solvers applicable for interconnects (no automatic model building, limited model area).
- No existing inductance extraction tools (identifying low-impedance return path requires analysis of the global circuit, which was prohibitively compute-intensive with the existing field solvers).
- Equivalent-circuit models of ULSI interconnects, used with SPICE, become computationally inefficient and often prohibitive because of their size and lack of circuit matrix sparsity due to distributed nature of inductive and capacitive coupling (Figure 1)
- No available optoelectronic (O/E) electric-optical device and system simulators.
- No coupled Device+EM modeling capability, e.g. for RF SiGe HBT, BiCMOS, HEMT, etc.

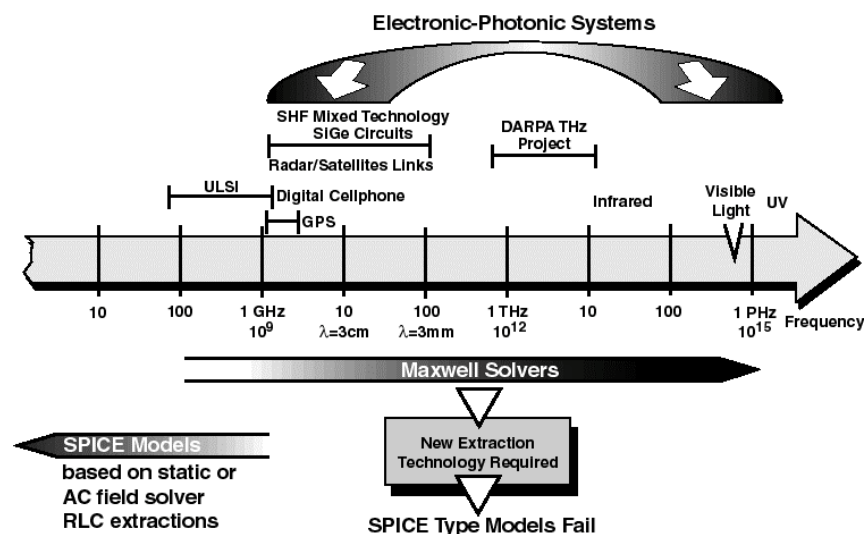


Figure 1. SPICE-type equivalent-circuit models of ULSI ICs, interconnects, and mixed-signal RF circuits become computationally inefficient and often prohibitive for higher frequencies.

Need for relevant TCAD and EDA tools for opto-electronic (O/E) circuits and systems

The increasing design complexity of the current and future ICs on each design level (component, module, package, system) is enhanced even more by introduction of optical elements on chip and printed circuit board. This calls for new modeling and simulation approaches allowing a fast and accurate interconnect modeling where a comprehensive treatment of all relevant physical effects has to be considered. Simply speaking, such comprehensive simulation and design tools for O/E circuits and systems do not exist yet. Some of the reasons are as follows:

- the comprehensive analysis of O/E circuits require coupled simulations in mixed domains, like electrical, mechanical, thermal, and of course full-vector electromagnetic;
- three-dimensional (3D) and spatially-dependent behavior of optical systems (Fig. 16, 12, and 15) can not be directly captured by standard EDA tools based mostly on 2D-layout approach;

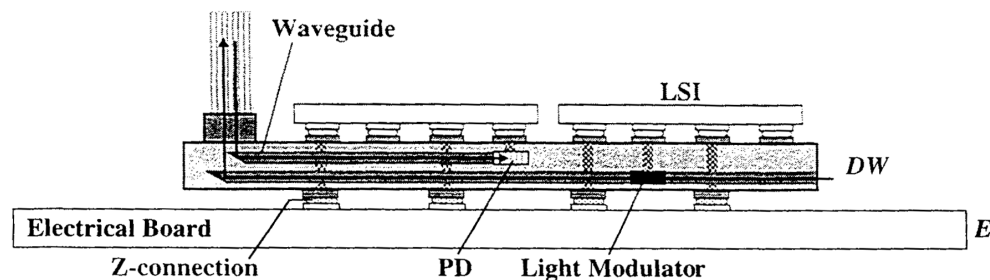


Figure 2. Example of a hybrid 3D opto-electronic design with a communication waveguide.

- the wave nature of optics and high-frequency electronics requires wave-based and vector-based description and modeling, which makes SPICE-type equivalent-circuit modeling very difficult or sometimes impossible;
- no comprehensive, reliable behavioral or equivalent-circuit models of photonic devices and next-generation electronic compound heterojunction devices;
- no available electric-optical device simulators for new optoelectronic devices (see below).

Why the existing TCAD tools could not efficiently handle O/E devices...

Before NeoCAD, there was no commercial TCAD tools on the market which would handle all the complexity of the photonic device operation, such as for example VCSEL. No existing device simulator contained fully coupled Device + Electromagnetic modeling capability (for accurate light propagation modeling), enhanced with satisfactory model of quantum well physics as well as thermal phenomena influencing both electrical and optical behavior. The only existing tools on the market had only partial components for optical devices simulations, like for example Crosslight software from Canada, or ISE TCAD tools from Switzerland.

1.3 Project Objectives and Scope

The overall objective of the OE-IDEAS project was:

- ❖ Design Automation Tools for Opto-Electronic Integrated Circuits and Interconnects

Our intension was to develop, implement, and demonstrate several innovative ideas in the following Technical Areas:

- EDA Interfaces and Front End for Automation
- Efficient Extraction of Parasitics in Electrical Interconnects
- New Methods of Electrical Interconnects Modeling for High Frequencies
- New Methods of Optical Interconnects Modeling
- Model-Order Reduction and Behavioral Models for Electronic-Photonic Devices and Circuits
- Integration of the New Methods and Software into EDA Tools for Opto-Electronic Design Flow and Automated Synthesis

The scope of this project in the overall Design Flow Methodology for mixed-signal electronic-photonic circuits is illustrated in the figure below.

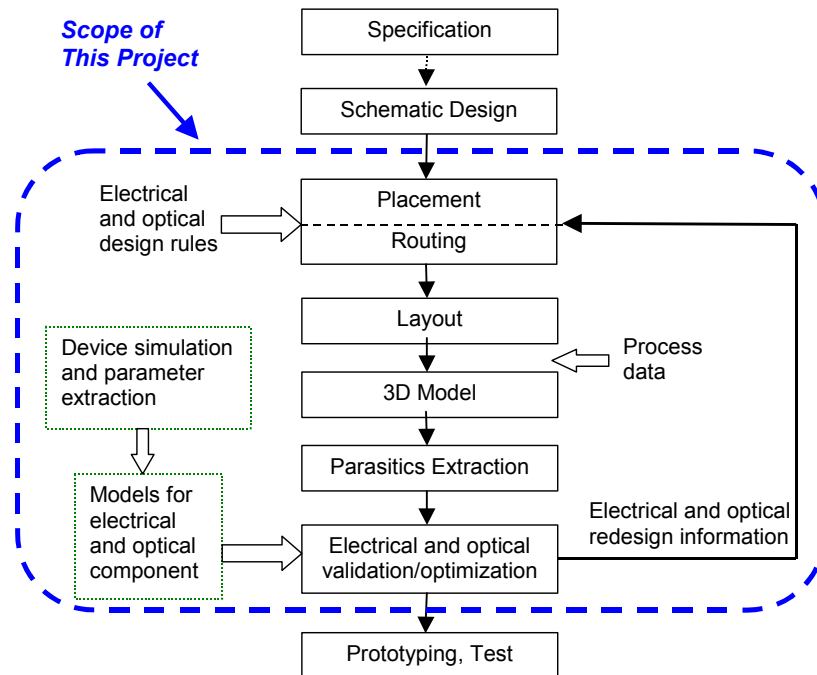


Figure 3. Extended Design Flow of electrical-optical circuits and printed circuit boards, with indicated scope of this project.

As microelectronics technology continues to advance, the associated electrical interconnection technology is not likely to keep pace, due to many parasitic effects appearing in metallic interconnections. Hence, the optical interconnections and photonic-electronic chips seem to be the most viable technology for future multi-GHz mixed-signal electronics [Li 2000]. Therefore, this projects focused on the following crucial issues in this domain:

1. Efficient and fast techniques of extraction of parasitics as well as revolutionary new methods of modeling parasitics in electrical interconnects, where high-frequency electromagnetic effects will not allow for using SPICE-type models anymore (cf. Figure 1);

2. New, comprehensive CAD tools for integrated opto-electronic (O/E) circuits and systems, which would allow designers to analyze and optimize the full-path signal characteristics, at all the stages of the optically communicating circuits (Figure 4).

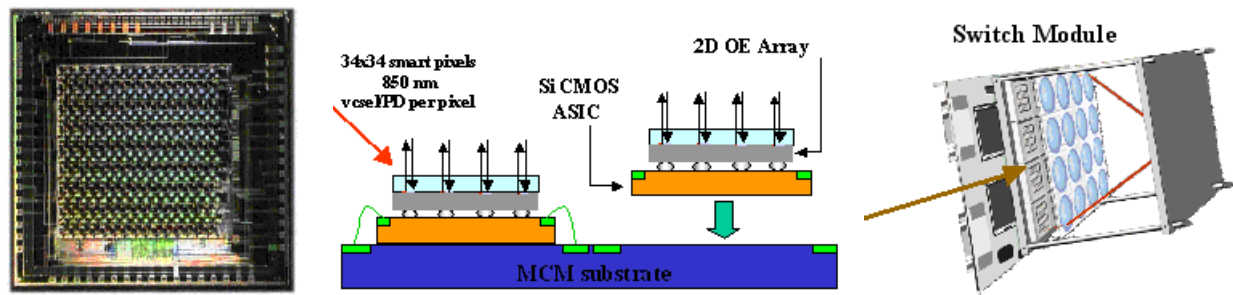


Figure 4. Examples of photonic VLSI integrated circuits and interconnections for future high-bandwidth communication systems, developed under DARPA FSOI and VLSI Photonics programs.

Such a comprehensive O/E CAD tool will allow to obtain the entire signal characteristics of:

- “Electrons to Photons” Path: from electrical signal drivers through all the complex interconnects and bonds of multi-chip setup up to optical wave characteristics at the output;
- Optical Path: through lenses, waveguides, fibers, resonators, etc.;
- “Photons to Electrons” Path: from optical flux input through all the complex interconnects and bonds down to electrical analog-to-digital (A/D) converters and amplifiers.

1.4 Summary of Accomplishments

All of the accomplishments aimed for fulfillment of the main objective of this project and its components, as described in the previous section. Following subsections list the most important accomplishments.

- **First in the U.S. commercial software for high-fidelity multi-mode simulation of Lasers (VCSELs, edge-emit.) and Photodetectors, O’SEMI from CFDRC:**
 - new Optical Gain Model, with quantum-physics and thermal phenomena;
 - implemented Effective Index Method for Edge-Emitting Laser optics;
 - new Tunneling Current Model, based on quantum model of heterojunction;
 - currently installed and used by AFRL/WL, ARL (Adelphi, MD), NRL, UCSB, UC Santa Cruz, U. Florida, U. Arizona, U. Waterloo, Vanderbilt Univ., and others;
 - inquiries from: Sandia National Labs, LLNL, McMaster University, et al.
- **New capabilities in CFDRC’s Full-Wave Electromagnetic Simulators for RF and Optical Interconnects:**
 - Signal monitoring and postprocessing: $V(t)$, $I(t)$, $Z(w)$, $S\text{-param}(w)$;
 - Electromagnetic filament model implemented and initially tested;
 - CFDRC full-wave EM solvers offered to NeoCAD Community, and used by Univ. of Delaware, U. of Washington, and U. of Cincinnati.
- **CFDRC’s Full-Wave 3D Simulator EMAG coupled with SPICE;**

- **Demonstrated Photonics Applications and provided Tutorials for EMAG users:**

- 1) Optical waveguide coupling;
- 2) Optical ring resonator;
- 3) Photonic crystal waveguide;
- 4) Photonic bandgap 2D matrix.

- **Simulated several NeoCAD benchmark structures:**

- 1) CP1 waveguide from HRL-Mayo,
- 2) 2OG transmission line from NCSU,
- 3) MIT-CLine01 coplanar waveguide,
- 4) NCSU-2BA Coupled Spiral-Inductor Transformer,
- 5) 100 GHz 100 GHz InP circuit from Mayo (see illustration below).

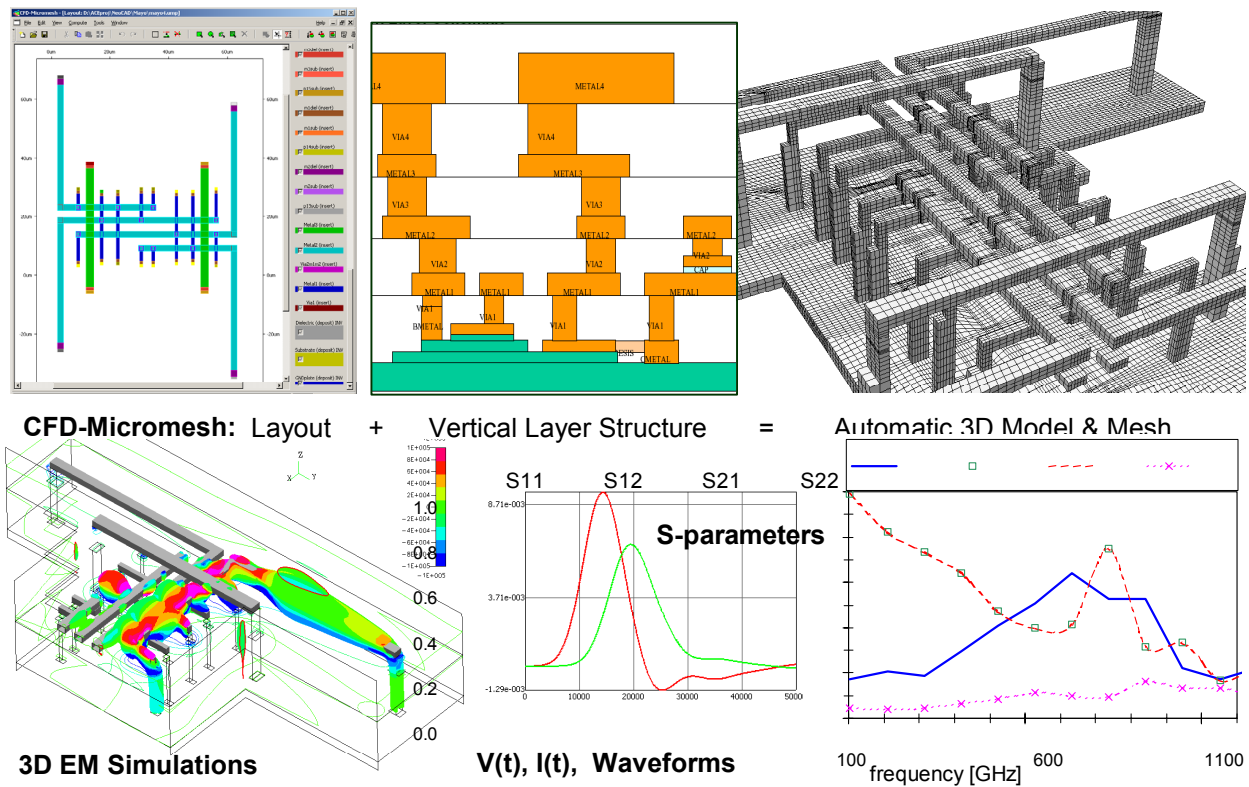


Figure 5. Parasitic Extraction of 100 GHz InP circuit, a NeoCAD benchmark from Mayo.

CFD-Micromesh - a unique, automated 3D mesher from IC layouts – **enhanced, offered to NeoCAD Community; new tutorials provided.**

Tasks led by University of Delaware:

- **Designed, fabricated, tested and measured an optical transceiver chip**, and built a 3D model (with CFD-Micromesh).
- Characterized and built a **3D model (with CFD-Micromesh) of the Mayo 10G system multi-chip module (MCM)**.
- Formulated the **transmission-line model and the π -model of via-stub resonance** on system PCB's; with CFDRC simulated the model performance .

- **Designed, fabricated, and tested** Dual-Rate Current Mode Logic electrical IO's.
- Tasks led by Cornell University:
 - Established the **quantum transport model hierarchy** in density gradient, quantum hydrodynamic, full Wigner, and NEGF on large barrier tunneling problems. The benchmark problems are RTD and MOSFET gate tunneling.
 - Established **large-signal transient analysis from S-parameters on nonlinear circuits**. The benchmark problems include high-power/high frequency transistors, nonlinear transmission lines, and buffer-insertion interconnect.
 - Proposed and analyzed **pulse-based interconnect architecture and circuit implementation**, based on the large-signal transient analysis.
 - Designed and verified the use of **patterned permalloy to control the on-chip magnetic fields** for accurate partial inductance extraction.
 - Designed and verified the **use of undergrids to control CMOS interconnect dispersion on transmission lines** and co-planar waveguides.
- Tasks led by UC Santa Cruz:

Developed, implemented, and tested compact models for OE devices for mixed-level mixed-technology simulation, and demonstrated in VHDL-AMS (Figure 6).

Modeling VCSEL and transmitter:

 - Developed a behavioral VHDL-AMS model of VCSEL;
 - Implemented the model into SMASHTM from Dolphin Integration;
 - Tested the VCSEL model by time domain simulation of different devices;
 - Simulated a simple transmitter consisting of CMOS driving circuit and VCSEL.

Modeling Metal-Semiconductor-Metal photodetector:

 - Developed a behavioral VHDL-AMS model of MSM photodetector;
 - Implemented the model into hAMsterTM provided by AnSoft;
 - Validated the model by comparing simulation results with experimental data.

Modeling Raman Amplifier:

 - Developed a behavioral VHDL-AMS model of Raman Amplifier;
 - Implemented the model into hAMster from AnSoft;
 - Validated the model by comparing simulation results with experimental data.

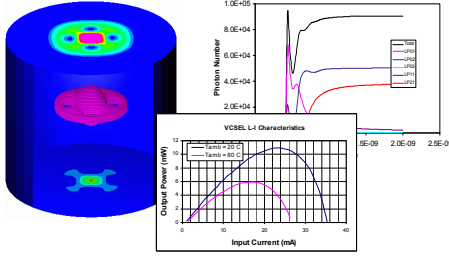
Modeling Erbium Doped Fiber Amplifier (EDFA):

 - Developed a behavioral VHDL-AMS model of EDFA;
 - Implemented the model into hAMster from AnSoft;
 - Validated the model by comparing with the experimental data.

Automation of O/E behavioral model parameters extraction:

 - Finished the linear part of VCSEL behavioral model parameter extraction using Python;
 - Implemented a nonlinear behavior model parameter extraction algorithms for Python.

High-Fidelity CFDRC Models



Behavioral VHDL-AMS Models

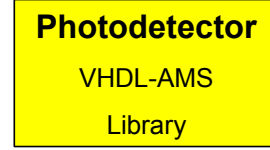
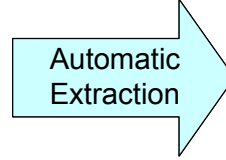
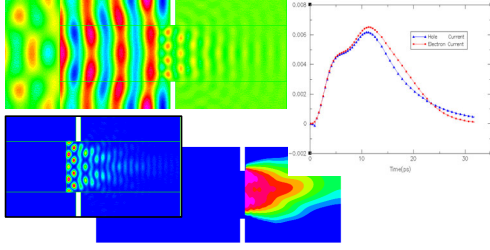
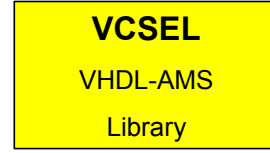
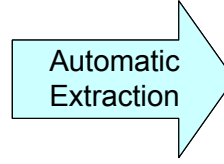


Figure 6. Extraction of OE behavioral models for mixed-level system simulation.

2 OPTO-ELECTRONIC DEVICE MODELS CONSOLIDATION FOR BEHAVIOR MODEL EXTRACTION

2.1 Enhancement of High-Fidelity Electro-Optical VCSEL Model

During this project CFDRC was working on enhancement of the high-fidelity model of semiconductor devices to take into account the complex phenomena inside Vertical-Cavity Surface-Emitting Lasers (VCSELs). This will allow for more realistic modeling and simulation of VCSELs and other photonic devices, also for better quality compact model extraction.

The new, enhanced electro-optical model includes the following equations:

Electric Potential (Poisson's) Equation

$$\nabla \cdot (-\epsilon \nabla \phi) = q(p - n + N_D^+ - N_A^-)$$

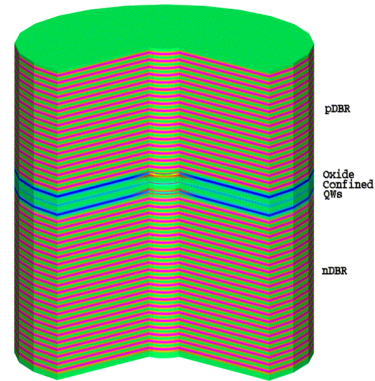
Carrier Continuity Equations

$$q \frac{\partial n}{\partial t} - \nabla \cdot \vec{J}_n = q(G - R)$$

$$q \frac{\partial p}{\partial t} + \nabla \cdot \vec{J}_p = q(G - R)$$

where the current densities are:

$$\vec{J}_n = qD_n \nabla n + qn \left\{ \mu_n \nabla \left(-\phi + \frac{E_c}{q} \right) + D_n \nabla T_n - \frac{3}{2} D_n \nabla \ln m_n \right\}$$



High-Fidelity VCSEL Model

$$\bar{J}_p = -qD_p \nabla p + qp \left\{ \mu_p \nabla \left(-\phi + \frac{E_v}{q} \right) + D_p \nabla T_p - \frac{3}{2} D_p \nabla \ln m_p \right\}$$

Carrier Energy Equations

$$\frac{\partial n w_n}{\partial t} + \nabla \cdot \bar{S}_n - \nabla \left(-\phi + \frac{E_c}{q} \right) \cdot \bar{J}_n + n \frac{w_n - w_L}{\tau_{wn}} = w_n (G - R)$$

$$\frac{\partial p w_p}{\partial t} + \nabla \cdot \bar{S}_p - \nabla \left(-\phi + \frac{E_v}{q} \right) \cdot \bar{J}_p + p \frac{w_p - w_L}{\tau_{wp}} = w_p (G - R)$$

where energy fluxes are

$$\bar{S}_n = -k_n \nabla T_n - \frac{1}{q} (w_n + k T_n) \bar{J}_n$$

$$\bar{S}_p = -k_p \nabla T_p + \frac{1}{q} (w_p + k T_p) \bar{J}_p$$

Photon Number (Rate) Equation

$$\frac{C}{\beta} \left\{ g_m - \frac{1}{2L} \ln(1/r_m) \right\} S + C_m \int R_{sp} dv = 0$$

Optical Wave Equation

$$\nabla^2 W + k_o^2 (\epsilon - \beta^2) W = 0$$

Example results of Quantum Well (QW) modeling are shown in the figures below. Such QW structures are typical for photonic devices, including VCSELs. The n and p regions at the ends of the structure in Figure 7 represent lumped models of the Distributed Bragg Reflectors (DBR).

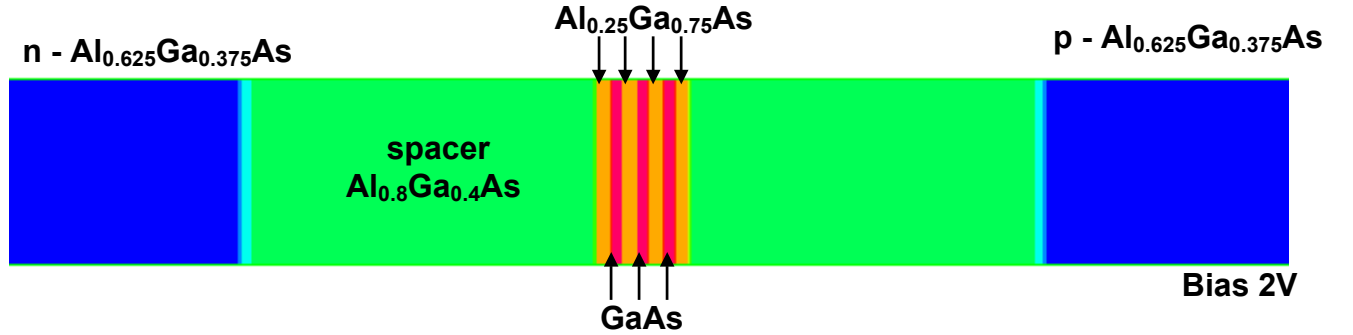


Figure 7. High-fidelity multiple Quantum Well (QW) model.

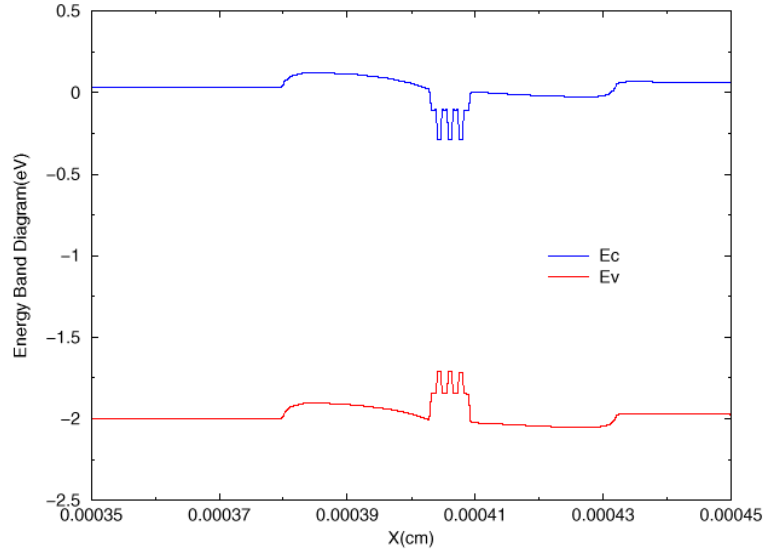


Figure 8. Energy Band Diagram of the Multiple-QW structure.

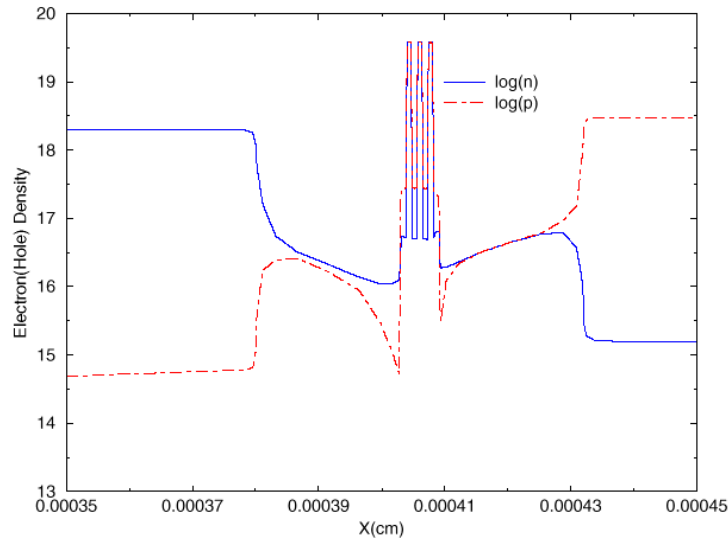


Figure 9. Carrier Density near the Multiple-QW structure.

The results shown above include the following **new OE-IDEAS developments**:

- Heterostructure Model (Energy Band Gap, Thermionic Current)
- Quantum Well Model (Tunneling Current)
- Full Newton Iterative Algorithm

2.2 Coupled Multiphysics Modeling of Semiconductor Lasers

Comprehensive models of semiconductor lasers are required to predict realistic behavior of various laser devices for the spatially nonuniform gain that results due to current crowding. Nonuniform gain has visible effect on laser dynamics and parameters, like threshold gain. Consistent solution of

coupled electrical, thermal, gain and optical problems was achieved by CFD-ACE+ integrated solver. Integration of multiphysics into a single computational environment allowed for high-efficiency, high-fidelity modeling of modern semiconductor lasers, including vertical-cavity surface-emitting lasers (VCSELs) and edge-emitting lasers (EELs).

This work allowed for the first time a full self-consistent coupling of the most-advanced-physics models of spatially dependent current flow, temperature effects, gain, and optical modes development and competition. Three coupled modules of CFD-ACE+: Semiconductor Device, Thermal, and Optics are used in the present study. The Semiconductor Device module solves electric model based on drift-diffusion (DD) equations for carrier densities, and energy balance (EB) equations for carrier temperatures. It has many advanced capabilities required by VCSEL simulations, such as quantum well (QW), heterostructure interface, etc. Figure 10 shows an example of simulation results of current flow and electron density distribution for an intracavity VCSEL problem.

Optical models include Weighted Index Method (scalar) and Method of Lines (scalar and vectorial). Both edge-emitting lasers and VCSELs can be efficiently modeled. The code allows to study transient behavior of lasers with time-dependent and spatially inhomogeneous gain. Multiple quantum wells and multiple transverse modes are included, as illustrated in Figure 11 through Figure 14. For each time step, a calculation loop over electrical, thermal, gain, and optical solvers is performed.

Solution for VCSEL transverse and axial field distribution in the modes as well as their lasing frequencies consists of solution of an eigenvalue problem for Helmholtz equation in cylindrical coordinates, and boundary value problem set by the boundary conditions at VCSEL layer and radial region interfaces. For each mode photon rate equation is solved including optical losses, and spontaneous and stimulated emission terms taking into account spatially and time-dependent material gain. Corresponding stimulated and spontaneous emission terms are responsible for carrier relaxation in the electrical model.

The simulation results were validated through comparison with experimental data obtained from U.S. Army Research Laboratory (ARL, Adelphi, MD). This kind of modeling is crucial for comprehensive analysis design, and optimization of new architectures of semiconductor lasers, as well as for reliable extraction of compact model parameters for system-level simulations.

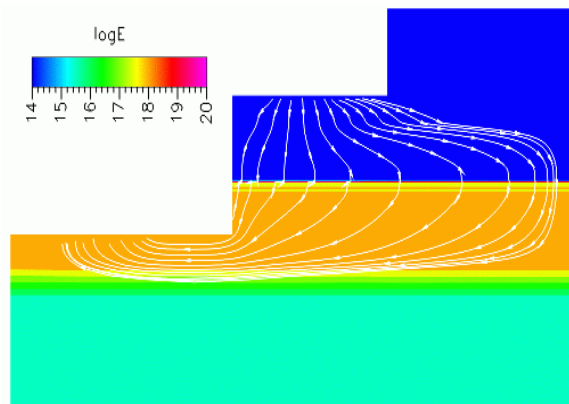


Figure 10. Current flow and electron density distributions inside an intra-cavity VCSEL device

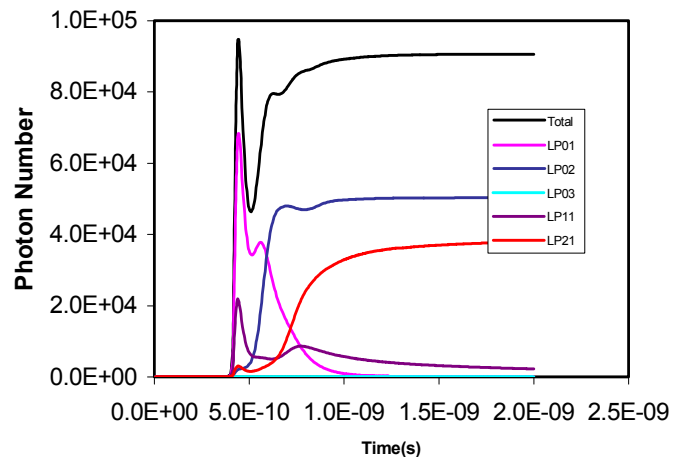


Figure 11. Transient behavior of multi-transverse-mode VCSEL. Photon numbers in single modes and total number of photons in the cavity.

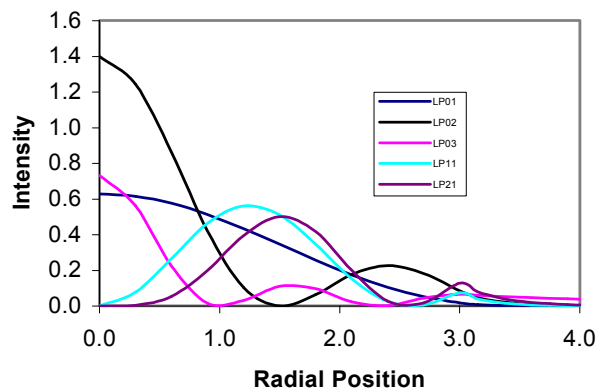


Figure 12. Steady-state radial distribution of intensity in different transverse modes for VCSEL with 6 micrometer oxide aperture.

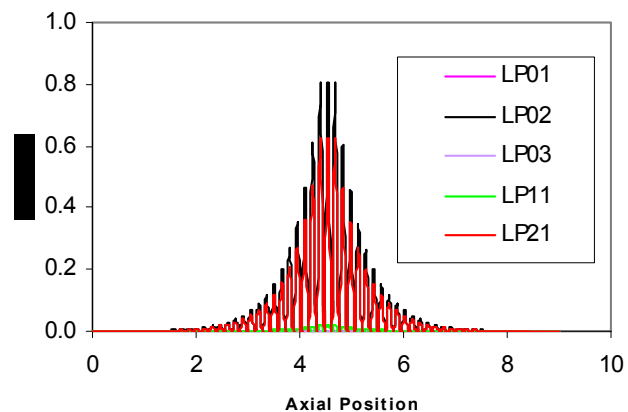


Figure 13. Steady-state axial distribution of intensity in transverse modes for VCSEL with 6 micrometer oxide aperture.

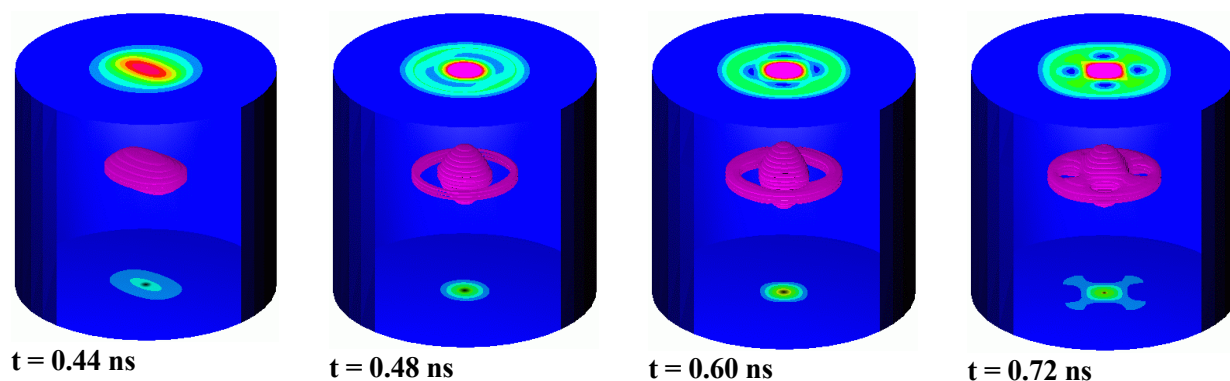


Figure 14. Selected snapshots of transient behavior of total optical intensity during the multi-transverse-mode VCSEL switching (cf. Figure 11)

The above simulations demonstrate **the first in the U.S. commercial software for high-fidelity multi-mode simulation of lasers** (VCSELs and edge-emitting lasers), by optical-electrical coupling of CFD-ACE+ Multiphysics Simulator from CFDRC with WIMP Optics from AFRL.

- The **first training course for DoD users** was held at WP-AFB on Oct.1-3, 2002.
- **Two new tutorials** (one for VCSEL, one for GaN EEL) have been developed and printed. This makes already 4 different O'SEMI tutorials available for users.
- **Two separate licenses** of the O'SEMI Package have been **shipped to University California at Santa Barbara** (one to Prof. Joachim Piprek, and second to Prof. Larry Coldren). UCSB is the leading U.S. institution in the R&D efforts for new lasers (VCSELs) and optoelectronic materials.

2.3 Quantum mechanical model enhancement of electronic and photonic devices

Lead: Cornell University, PI: Edwin Kan

Partial-differential-equation (PDE) level inclusion of quantum mechanical effects in nano-scale electronic and photonic devices is difficult in direct formulation, mainly due to nonlocality and coherence in phase space. The problem has been attempted early in the development history of quantum mechanics, in particular Feynman's effective potential smoothing based on Nonequilibrium Green's Function (NEGF). At Cornell, the effective potential formalism and several other recent proposals such as quantum potentials and transmission matrix have been compared analytically and numerically (on PROPHET platform). All formalisms need to couple to Poisson equation and carrier statistics on the boundary to be meaningful for device operational modeling. Self-consistent solution was attempted in the first year of the project, to understand its physical accuracy and numerical properties.

For a general semiconductor device we can split the potential into the sum of a smooth function and a discontinuous function. A key point to note here is that the discontinuous part (or large perturbation in terms of the thermal wavelength) of the potential is caused by an abrupt material interface and is known a priori once the device structure is known. It is independent of any self-consistent calculation required to calculate the total potential by iterating the transport equations with the Poisson equation. We can therefore in principle calculate the effect of the large potential variations exactly using the integral form given above. In other words, the Bloch equation now becomes $U_{tot} = U_{sm} + U_{dis}$. For any simple 1-D barrier given by, such as for example found in a MOS transistor or a quantum well, we can now solve for the Wigner function in equilibrium. Alternatively, we can try to Fourier transform the whole Bloch equation with respect to momentum (in effect transforming the equation to that for the density matrix in the difference coordinate).

We can then take moments on this equilibrium Wigner function to obtain self-consistent solutions with the Poisson equation and inclusion of scattering.

$$\begin{aligned}\frac{\partial n}{\partial t} + \frac{1}{m} \nabla \cdot \mathbf{\Pi} &= 0 \\ \frac{\partial \mathbf{\Pi}}{\partial t} + \nabla \cdot (\mathbf{u} \mathbf{\Pi} - \mathbf{P}) &= -n \nabla U - \frac{\mathbf{\Pi}}{\tau_m} \\ \frac{\partial W}{\partial t} + \nabla \cdot (\mathbf{u} W - \mathbf{u} \cdot \mathbf{P} - \mathbf{Q}) &= \mathbf{u} \cdot \nabla U - \frac{(W - W_0)}{\tau_w}\end{aligned}$$

In the moment equation, the only different term from the conventional Boltzmann transport is at the stress tensor:

$$\begin{aligned}P &= -\left\langle \frac{p^2}{m} \right\rangle = \frac{\hbar^2}{m} \frac{\partial^2 \rho}{\partial \eta^2} = -nk_b T - \frac{\hbar^2 \beta}{12m} (n + f(x+a)) \nabla \nabla U + C(x+a) \\ C(x+a) &= -f(x+a) e^{-\beta U} k_b T \left[1 - \frac{\hbar^2 \beta^2}{8m} \left(\nabla^2 U - \frac{\beta}{3} \nabla U \cdot \nabla U \right) \right]\end{aligned}$$

This can be seen as the density gradient theory with a position-dependent correction term, which captures the drop in density of carriers near the barrier due to barrier repulsion. The tunneling current in finite barrier and temperature can thus be self-consistently included. We are now trying to generalize this formalism to multi-dimension cases in realistic device structures. The goal is to obtain a tangible PDE form, and later on, further reduce to compact models for quantum electronic and photonic devices.

In next step, we obtained a full set of novel Wigner moment equations shown above. The equation is not a simple addition of the quantum correction, but by moment generation from an exact Wigner function in equilibrium in the presence of a large potential barrier resulted from material heterojunctions. We have compared this approach with the density gradient theory and have found significant improvement in modeling the carrier behavior inside the barrier (tunneling by the evanescent mode). Then, we formulated various measurable operators, including carrier concentration and carrier flux. Details of the equation are presented in the two papers on Quantum Hydrodynamic Modeling of Semiconductor Transport (listed in References section), by Venkat Narayanan and Edwin Kan from Cornell University.

As a final stage of corroboration of the Wigner-based moment equation, we have composed a nonequilibrium Green function (NEGF) solver, which provides information in the dimensions of space, momentum and energy. For a 1-D case with only optical and acoustic phonon scattering, the solver can be put together in relatively straightforward manner instead of re-engineer software from elsewhere. The computational efficiency for NEGF is however only good for corroboration since any realistic device structure will take unrealistic time. The full Wigner solver we have obtained last term is also functioning and provide another benchmark. We have used these solvers to compute the explicit formula of stress tensors and energy flow in the Wigner-based moment equation and the density gradient algorithm in order to understand the underlined assumption and accuracy. The figures below show the stress tensor comparison in a tunneling barrier under equilibrium and 0.5V bias.

Quantum Transport

- Quantum hydrodynamic (QHD) equations are the same as classical ones in the first three moments, and the only difference is at the **closure**.

Construct the density matrix from NEGF, then construct the pressure tensor from definition (closure for 2nd moment)

$$P = \lim_{\eta \rightarrow 0} \frac{\hbar^2}{m} \frac{\partial^2 \rho(x, \eta)}{\partial \eta^2}$$



Evaluate pressure tensor from the kinetics (inspired by the equilibrium guess) (QHD)

$$P = n(U(x) - E(x))$$

$$E(x) = \int dk |\psi_k(x)|^2 \frac{\hbar^2 k^2}{2m} e^{-\frac{\beta \hbar^2 k^2}{2m}}$$



Further simplification to n only (QDD)

$$P = -nk_bT + \frac{\hbar^2}{4m} \frac{\partial^2 n}{\partial x^2}$$

- Add **phenomenological scattering** (required at boundaries)
- Use NEGF to obtain QHD or QDD closure conditions
- Benchmark with existing approaches such as density gradients

Stress Tensor Comparison (2nd Moment Closure)

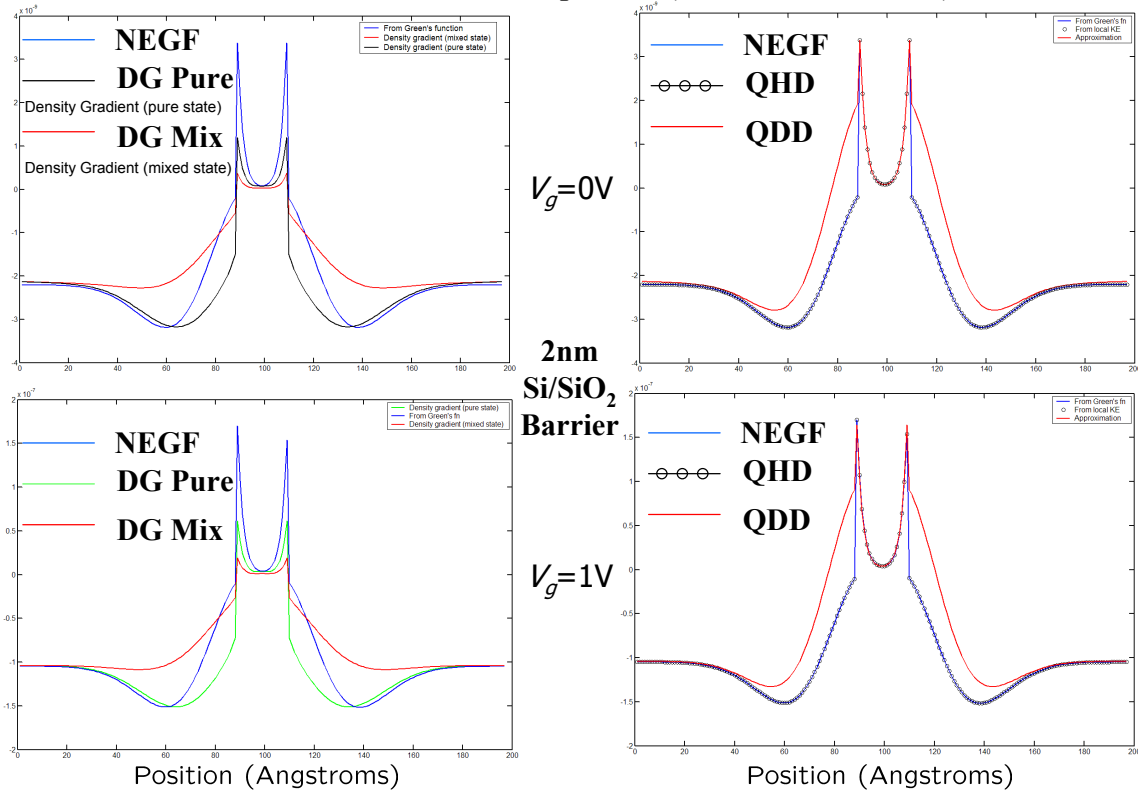


Figure 15. Quantum transport modeling procedure, and sample results of the stress tensor in a tunneling barrier under equilibrium (0 V) and 1 V bias.

3 IMPLEMENTATION OF HIGH ACCURACY ROBUST 3-D EM SOLVERS

CFDRC worked on two different 3-D Electromagnetic Maxwell equation solvers:

- Finite-Difference Time-Domain (FDTD) Solver: CFD-Maxwell, and
- Finite-Volume Magnetic-Vector-Potential based solver (EMAG)

They were modified and enhanced to be maximally efficient when used with Cartesian grids, new types of unstructured grids, as well as with Filament and Wire models. There are cases when implicit code (EMAG) is better, and in other cases explicit FDTD code (CFD-Maxwell) may be more efficient. Examples are:

- * CFD-Maxwell scales linearly with the number of mesh cells, which is a big advantage over the implicit electromagnetic solver (EMAG). For very large problems (millions of mesh cells), the explicit FDTD code will be probably the only available option.
- * CFD-Maxwell is intrinsically suited for parallelization.
- * EMAG is good for coupled multi-physics problems, e.g. with thermal, mechanical, etc., as an integral part of the Multi-Physics Suite CFD-ACE+. Also, it should be more efficient for stiff problems, like solving conductive currents in wires together with electromagnetic fields in surrounding insulators.

Therefore, we continued to develop, improve, and test both the electromagnetic codes at CFDRC, because we had seen a big potential for both of them in the future comprehensive CAD package for Opto-Electronic Interconnects.

3.1 Finite-Difference Time-Domain (FDTD) Solver: CFD-Maxwell

3.1.1 FDTD Solver Adaptation and Verification for RF Interconnects

Primary target was to obtain sufficient trust in the reliability and accuracy of CFDRC's electromagnetic 3D full-wave FDTD solver, CFD-Maxwell. This was an essential foundation for future developments. Therefore, we performed several validation studies, described below.

Example 1

The first validation case was a shielded coupled microstrip line problem, as shown below.

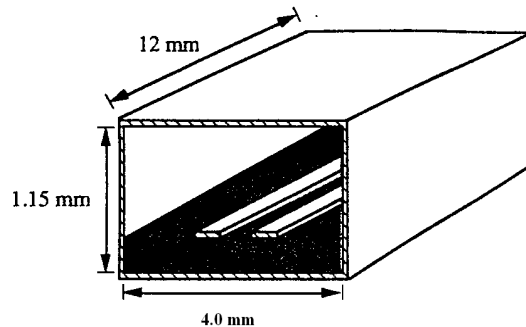


Figure 16. The coupled microstrip line. The strips are 0.05 by 0.3 mm and separated by 0.3 mm, the dielectric slab is 0.25 mm thick and has a relative dielectric constant ϵ_r of 4.5.

Results from earlier supercomputer simulations for this specific case have been published by Becker, Harm and Mittra in: “Time-Domain Electromagnetic Analysis of Interconnects in a Computer Chip Package”, *IEEE Transactions on Microwave Theory and Techniques*, Vol. 40, No. 12, Dec. 1992. The results obtained with CFD-Maxwell (Figure 17 and Figure 18) match these previously published numbers with discrepancies on the order of 1% to 2%.

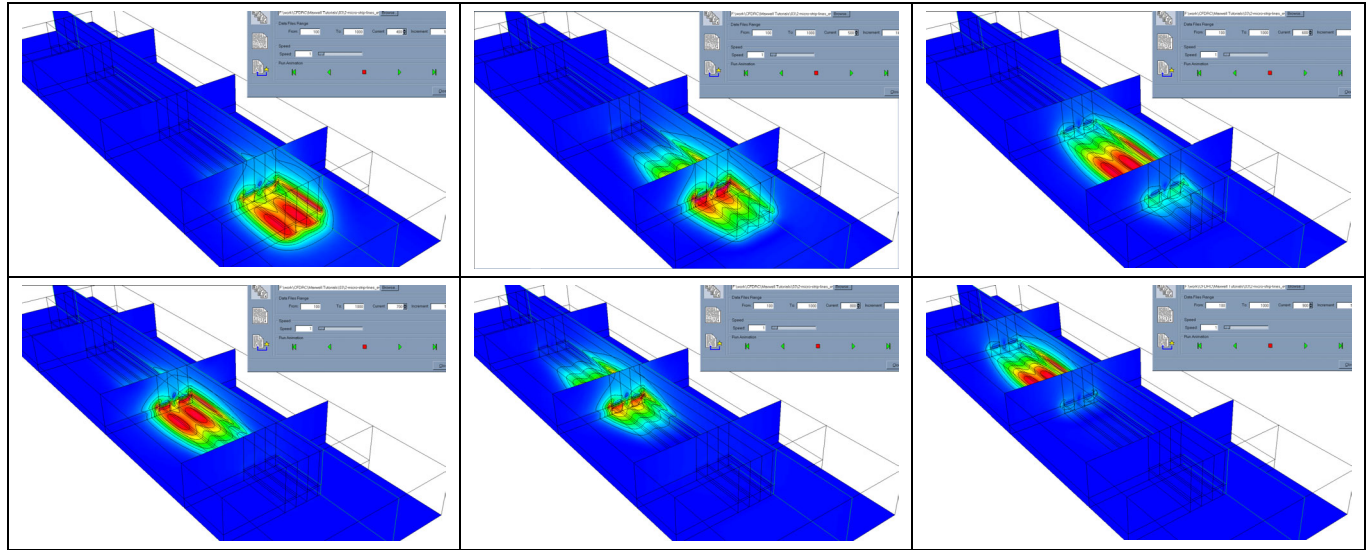


Figure 17. Propagation of an even mode Gaussian pulses (Pulse Width 10^{-11} s) along a coupled microstrip line.

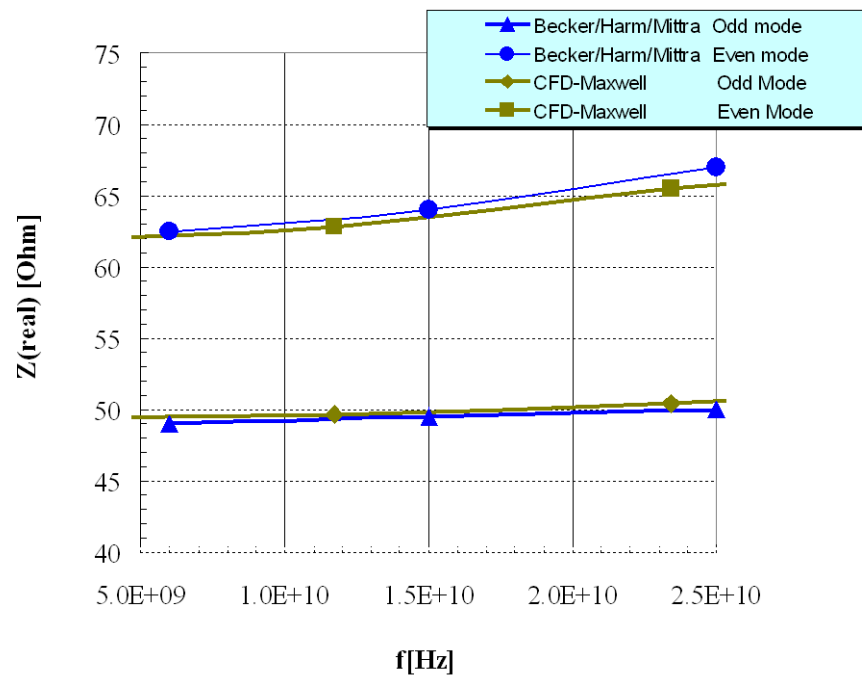


Figure 18. CFD-Maxwell impedances for even and odd mode excitation in a frequency range between 5GHz and 25GHz in comparison with the results from Becker, Harm and Mittra (*IEEE Trans. on MTT*, 1992)

Example 2

As a second example we chose a 5-line interconnect structure published in [Beattie, 2000], and shown in Figure 19. It is a five line signal bus over a ground mesh. For all signal lines driver resistance is $50\ \Omega$, load capacitance $2\ \text{fF}$, thickness $3.5\ \mu\text{m}$, spacing $10\ \mu\text{m}$, length $1000\ \mu\text{m}$ and width $10\ \mu\text{m}$. Spacing to ground plane is $5\ \mu\text{m}$. System size is about $1005\ \mu\text{m}$. Materials are copper ($\rho = 17.5\ \text{n}\Omega\text{m}$) and SiO_2 ($\epsilon_r = 3.9$, $\mu_r = 1.0$). The middle signal line is active. In CFD-Maxwell at that time we didn't have yet available a lumped capacitance model (it was developed later), so we used a resistive line terminations on the far end.

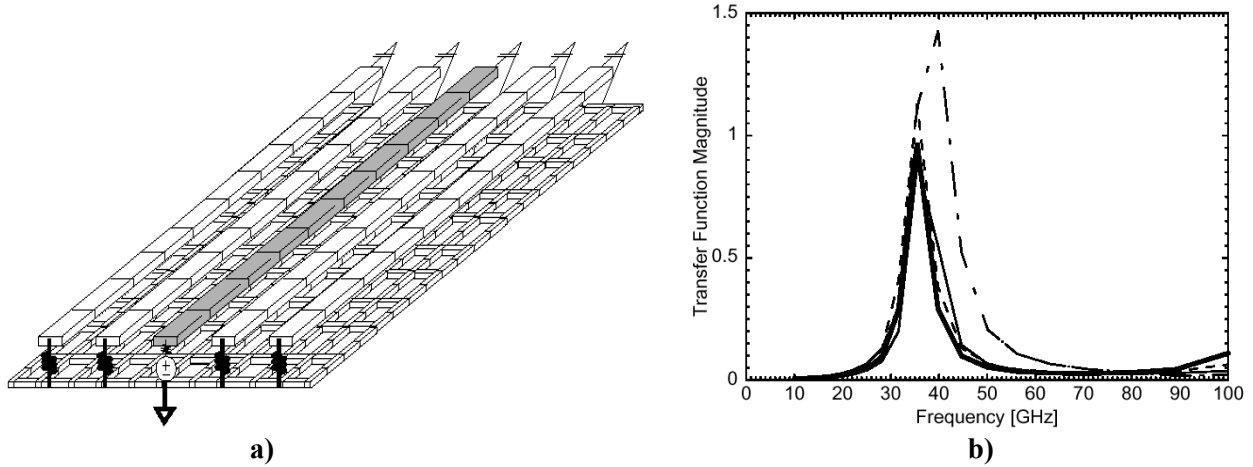


Figure 19. Test case of interconnects: five-line signal bus over a ground mesh (a) and its transfer function from near to far end node of leftmost signal line, calculated with different equivalent circuit models in [Beattie, 2000].

A 3D computational meshed model for CFD-Maxwell, built automatically using CFD-Micromesh, is shown in Figure 20.

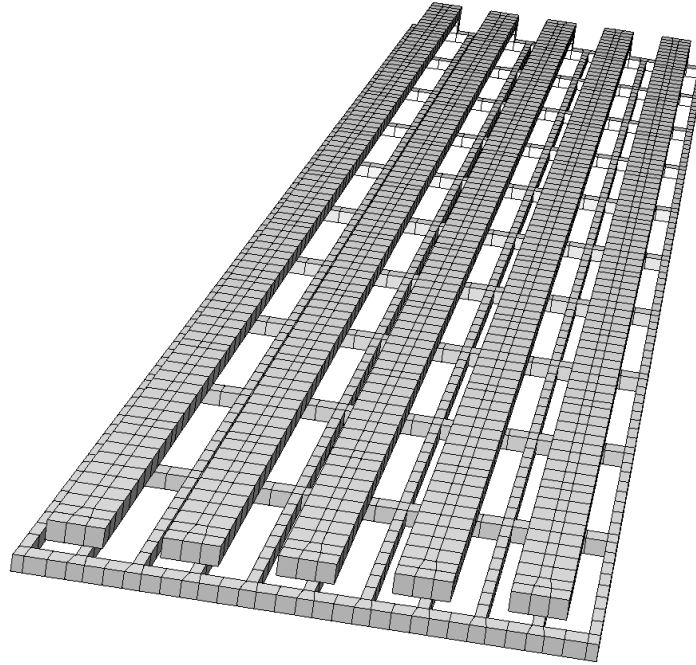


Figure 20. Our meshed model of the solid (Cu) parts of the 5-line bus interconnects from Figure 19a. The mesh was built automatically in CFD-Micromesh within a few seconds.

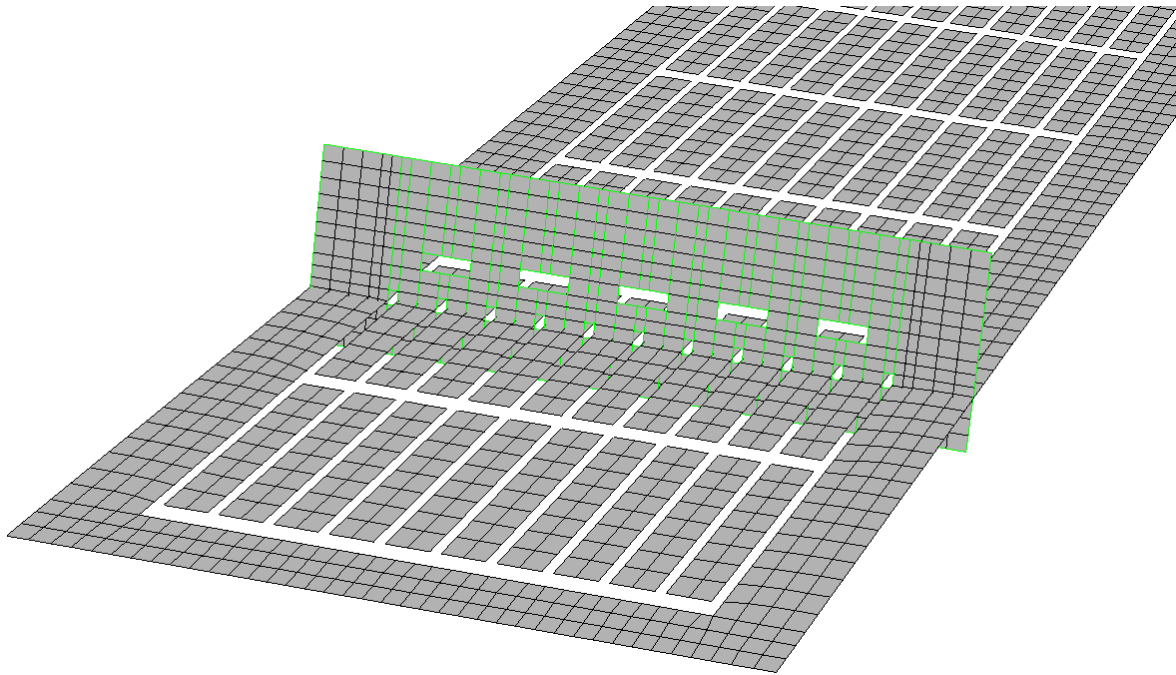


Figure 21. Two cross-sections showing meshed insulator parts of the 5-line interconnect structure (the copper parts are blanked for better visualization). The full mesh, built automatically in CFD-Micromesh, has about 46,000 cells.

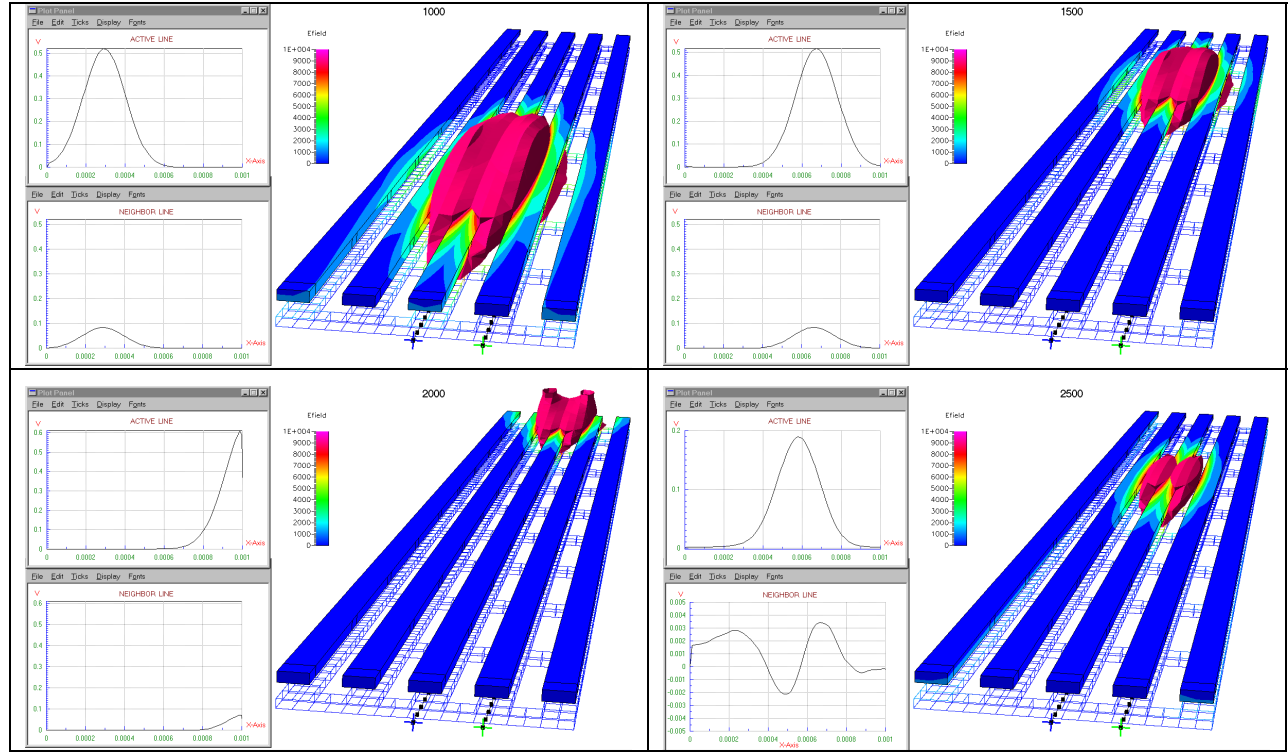


Figure 22. Several selected snapshots from CFD-Maxwell transient simulation of a propagating Gaussian pulse of 1ps width, after 1000 time steps (5 ps of the simulated time), 1500 steps (7.5 ps), 2000 steps (10 ps), and 2500 steps (12.5 ps). The last snapshot shows a reflected wave from the unmatched line termination.

An electric signal pulse was applied to the middle line, from a voltage source with internal resistance $50\ \Omega$, as illustrated in Figure 19a. Two types of pulses were applied: Gaussian and trapezoidal (which is closer to the shape of digital signals). Several selected snapshots of CFD-Maxwell simulation of a propagating Gaussian pulse of 1ps width are shown in Figure 22. The plots on the left side of each case show voltage distribution along the active line (upper plot) and along the neighbor line (lower plot) for each time instant. This allows for cross-talk analysis in the interconnect structure. For example, in the first (upper-left) snapshot in Figure 22, at time step 1000 (which corresponds to 5 ps of the simulated time) the cross-talk voltage on the neighbor line reaches about 20% of the active voltage.

To calculate the characteristic impedance of the line, first we terminated all the lines with a short circuit ($R = 0$). We monitored the voltage and current values in the middle line at the near end of the line ($v1$ and $i1$, at 0.1 of the length) and at the far end of the line ($v2$ and $i2$, at 0.9 of the length). Time dependent waveforms of these monitored voltage and current values are presented in Figure 23. On the time scale, 1000 time steps corresponds to 5 ps of simulated time. In this case, due to the short circuit at the line termination, the voltage pulse is reflected with the opposite sign from the far end, and comes back to the near end of the line.

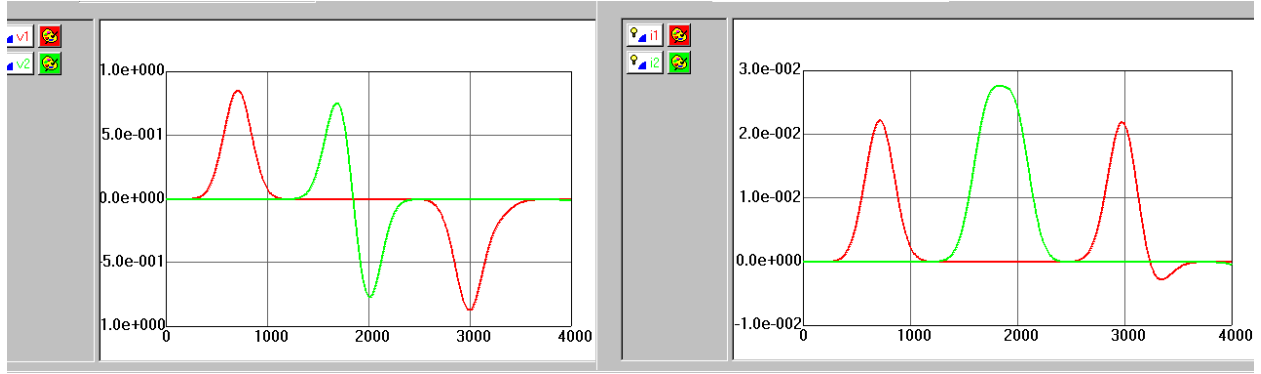


Figure 23. Voltages (left plot) and currents (right plot) varying in time in the middle line of the 5-line bus, with a short circuit ($R=0$) at the line termination. The values were monitored at the near end of the line ($v1$ and $i1$, at 0.1 of the length – red curves) and at the far end of the line ($v2$ and $i2$, at 0.9 of the length – green curves). 1000 time steps corresponds to 5 ps of simulated time.

From the first simulation we determined the characteristic impedance of the line to be 38.7Ω . When we applied $R = 38.7 \Omega$ as the line termination, to ensure the matching impedance at the end, the signals were not reflected anymore, as illustrated in Figure 24 and Figure 25.

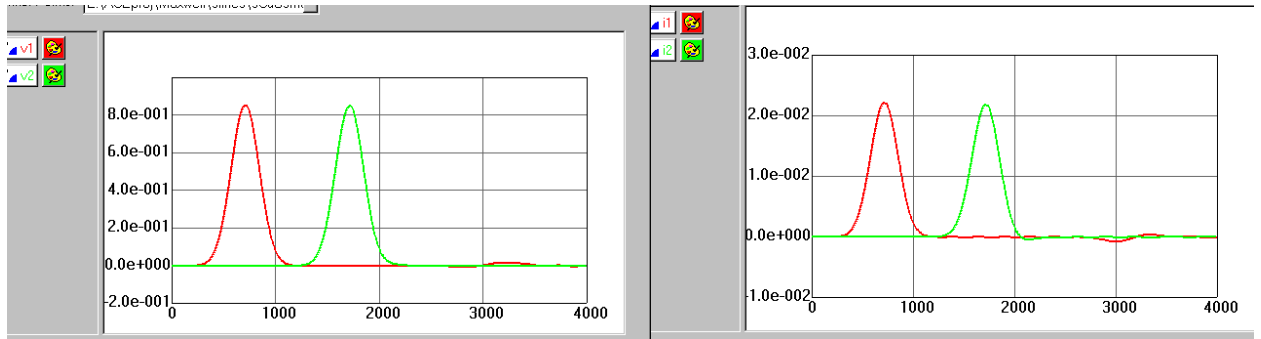


Figure 24. Time-dependent voltages (left) and currents (right) in the middle line of the 5-line bus, with a matching impedance ($R = 38.7 \Omega$) at the line termination.

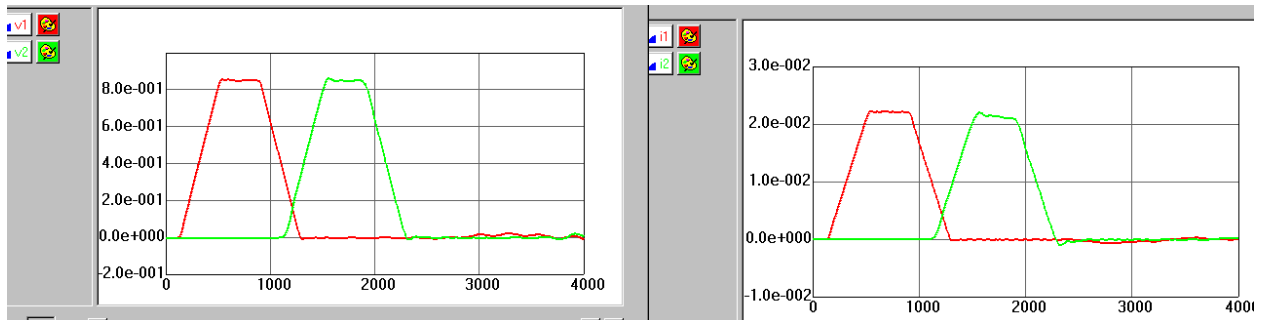


Figure 25. Time-dependent voltages (left) and currents (right) in the middle line of the 5-line bus, with a matching impedance ($R = 38.7 \Omega$) at the line termination, with a trapezoidal pulse applied to the input of the middle line. 1000 time steps corresponds to 5 ps of simulated time.

From the Gaussian pulse simulation, illustrated in Figure 24, we calculated the S-parameters of the middle line of the 5-line bus, to obtain among others the transfer characteristic similar to the one presented in Figure 19b. Our calculated S-parameters for the middle line are shown in Figure 26.

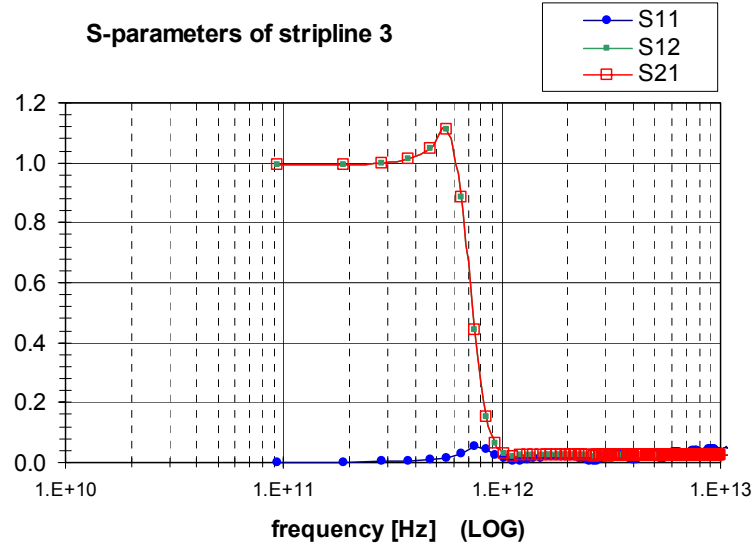


Figure 26. Plot of S-parameters calculated from the transient simulation of Gaussian pulse.

The problem with our calculation of S-parameters as a function of frequency from transient results (through Fast Fourier Transform, or FFT) is that the lowest calculated frequency is proportional to the extent of sampling time of the time-domain signal. Since our first transient calculations featured very fast signal (1ps wide pulse) and very short covered time (total of 20 ps), the lowest frequency value obtained from the FFT was $9.3E10$ Hz, or 93 GHz (Figure 26), which was high above the range in which we would like to obtain the S-parameters (cf. Figure 19b). To cover the lower frequency range, we should run a longer signal pulse, in a longer simulated time range. However, the time step in the FDTD method is limited by the smallest mesh cell size (Courant condition), so we could not increase time step for this particular structure (since the smallest mesh cell size was determined by the smallest physical dimension of the line, that is its thickness of $3.5\ \mu\text{m}$). Therefore, we had to use the same time step, but just to run the simulation for much more time steps, going into thousands. Sample results of such simulation of a longer Gaussian pulse (10 ps wide) are presented in Figure 27a, and for a trapezoidal pulse 10 ps wide – in Figure 27b.

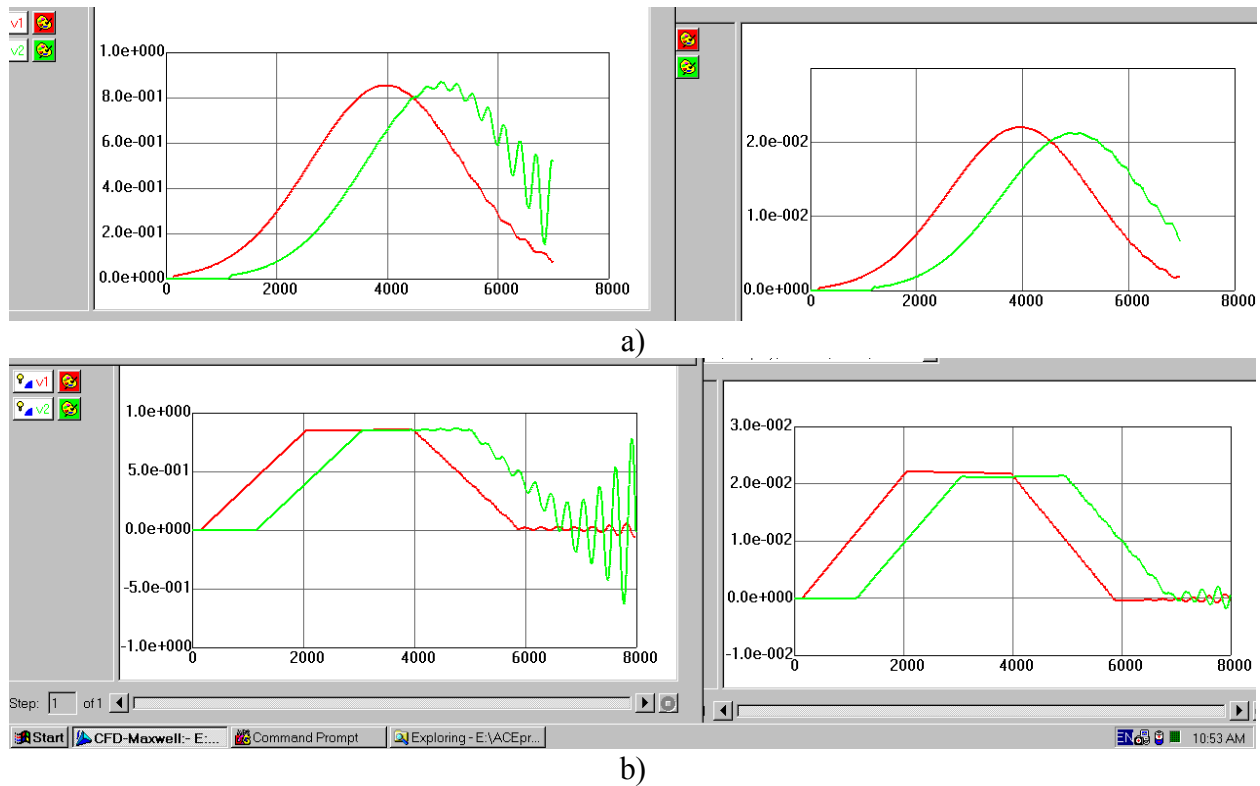


Figure 27. Time-dependent voltages (left) and currents (right) in the middle line of the 5-line bus, with a 10ps-wide Gaussian pulse (a) and 10ps-wide trapezoidal pulse (b) applied to the input of the middle line. On the time scale, 1000 time steps corresponds to 5 ps of simulated time.

In the cases illustrated in Figure 27 we hit the known generic problem of the explicit FDTD method, called “late time instability”, which causes FDTD simulations on not perfectly rectangular meshes (which is our case) with many thousands of time steps to diverge and prevents one from obtaining a stable solution for longer simulated time intervals. Since the time step can not be increased due to the Courant condition, as explained above, this poses a serious problem for longer times, or lower frequencies, or EM simulations of structures containing very small geometrical features (which force a very small time step).

An alternative would be using CFDRC’s implicit electromagnetic solver (EMAG module in ACE+) which does not impose such strict limits on the time step length. The EMAG solver during the NeoCAD Program was enhanced with special features for electrical interconnect simulations, like extracting and displaying time-varying voltages and currents in metal lines, calculating characteristic impedance, S-parameters, etc. They are described in later sections of this report.

New Capability in CFD-Maxwell: Capacitive Line Termination

In many cases in integrated circuits, the termination of an interconnecting line may have capacitive character. In particular, for signal lines it can be gate of a MOSFET. Quite often it is the most appropriate to model the interconnect transmission lines as driven by a resistive voltage source at the input, and terminated by load capacitances, as illustrated in Figure 28.

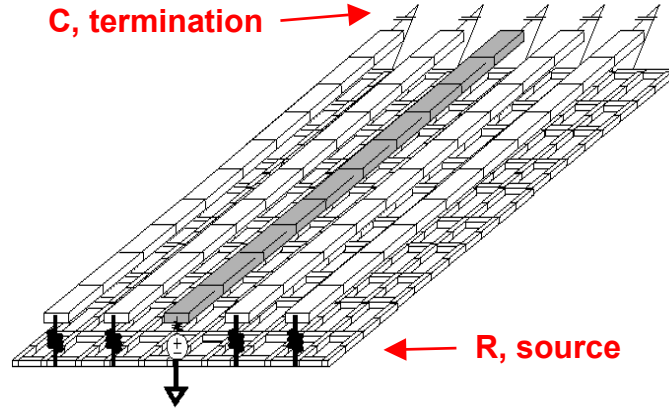


Figure 28. Example of five parallel signal lines driven by resistive voltage sources and terminated by load capacitances.

The characteristic impedance of the transmission line determines the current that can be supplied to charge capacitive load C_L . From the load's point of view, the line behaves as a resistance with value Z_0 . The transient response at the capacitor node, therefore, displays a time constant $Z_0 C_L$. This is illustrated in Figure 29, which shows the simulated analytical transient response of a transmission line with a characteristic impedance of $50\ \Omega$ loaded by a capacitance of $2\ \text{pF}$. The response shows how the output rises to its final value with a time-constant of $100\ \text{psec}$ ($= 50\ \Omega \times 2\ \text{pF}$) after a delay equal to the time-of-flight of the line.

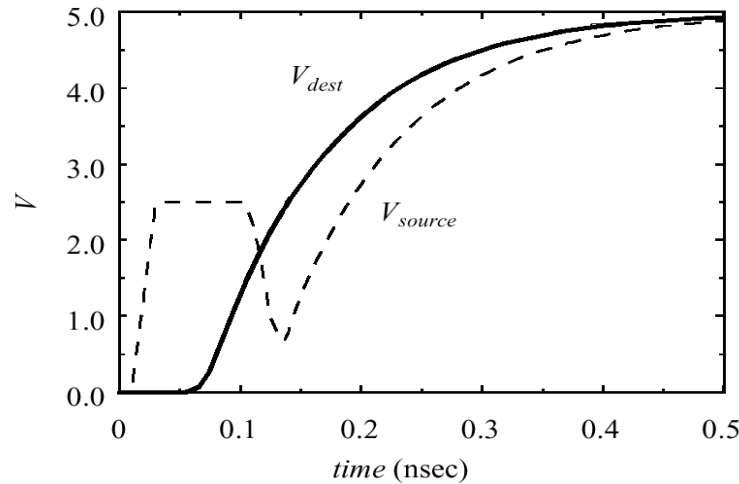


Figure 29. Theoretical transient response of a transmission line with a characteristic impedance of $50\ \Omega$, loaded by a capacitance of $2\ \text{pF}$, to an applied step voltage of 5V .

To verify the newly implemented capacitive-termination capability in CFD-Maxwell, we have performed simulations of an applied 5V step voltage to calculate transient response of a transmission line loaded by a capacitance and by a matching impedance (resistance). The obtained waveforms of input voltage (V_{in}), output voltage (V_{out}), input current (I_{in}), and output current (I_{out}) for the line with capacitive termination are shown in Figure 30. Our FDTD results of voltage

waveforms are very similar to the expected theoretical results from Figure 29. This confirms proper implementation of the new capacitive line termination model in CFD-Maxwell.

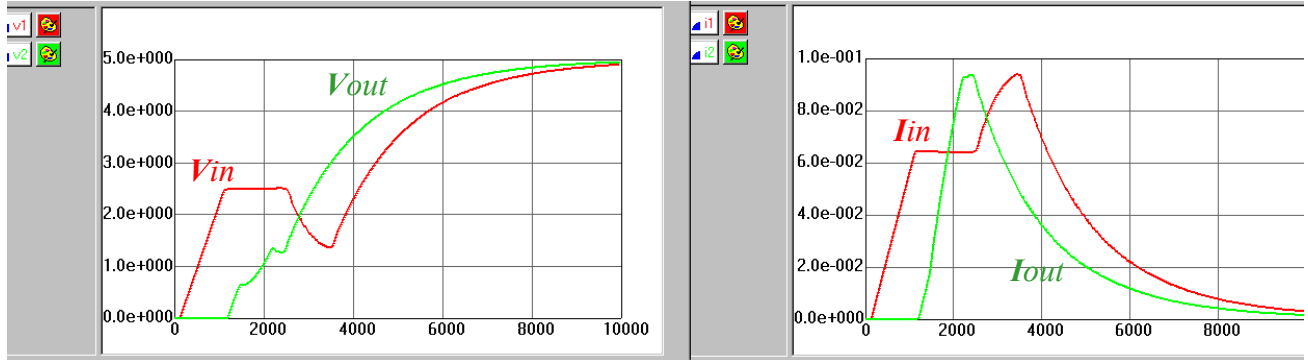


Figure 30. CFD-Maxwell results for a transmission line with capacitive termination: time dependent voltages (left) and currents (right).

3.1.2 FDTD Solver Applications for Optical Modeling

The tests reported above focused on examples verifying the validity of solutions for basic, high frequency electronic building blocks (transmission lines.) Equally important, however more complicated, is the validation of pure wave propagation problems since in those cases not single quantities (such as impedance) or one-dimensional functions (such impedance as a function of frequency) are the results of simulations, but in many cases 2D or 3D wave propagation patterns and/or energy propagation distributions. Such solutions are inherently sensitive to mesh imperfections and numerical stability issues have to be observed carefully.

Moreover, beside obvious cases of instability, FDTD simulations can yield reasonably appearing results that are inaccurate. Rules have been established for acceptable mesh configurations and aspect ratio changes, including guidelines concerning the mixed application of structured and unstructured meshes, since such rules are not yet incorporated in intelligent agents that would control the meshing process (Figure 31 through Figure 33). Simulation results must be trusted sufficiently that they can form the basis for devices to be fabricated.

The application of shape-conformal meshes is imperative for precise wave scattering solutions. This capability is one of the key features provided by CFD-Maxwell and was utilized for the OE-IDEAS developments. In order to confirm proper operation of the code, examples with analytical solutions are invaluable. EM wave scattering on dielectric and perfectly electrically conducting cylinders are two of the few known cases for which analytical solution involving infinite series of Bessel and Hankel functions and satisfying Maxwell's equations can be found.

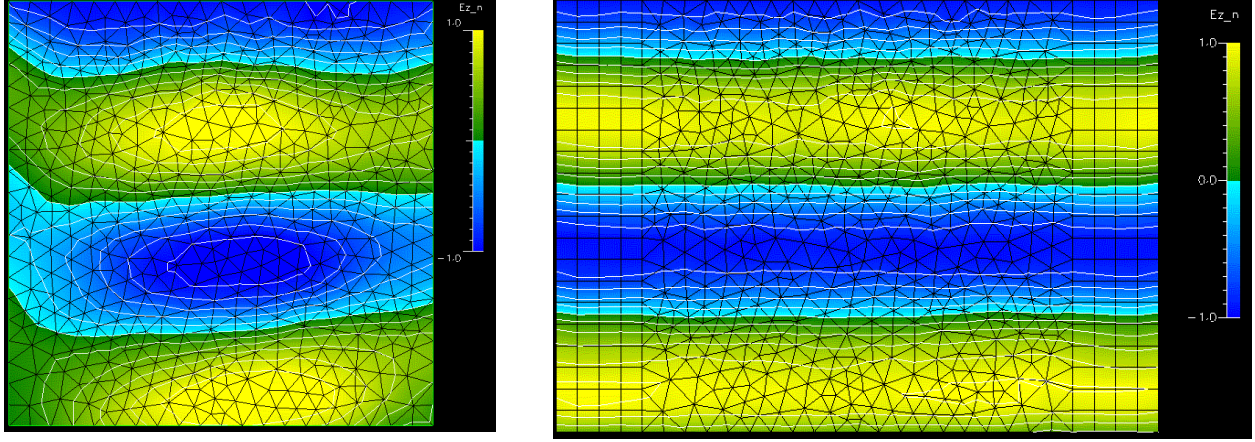


Figure 31. TM wave propagation test in 2D domain, $\lambda / \Delta x = 12$ [Δx = cell edge length], solver in total field formulation mode, $E_z(x,y)$ plotted at arbitrary time, Left: unstructured mesh, left and right boundary ABC, strong distortion of wave fronts; Right: unstructured mesh + Cartesian buffer zone, left and right boundary: extrapolation, wave fronts are preserved.

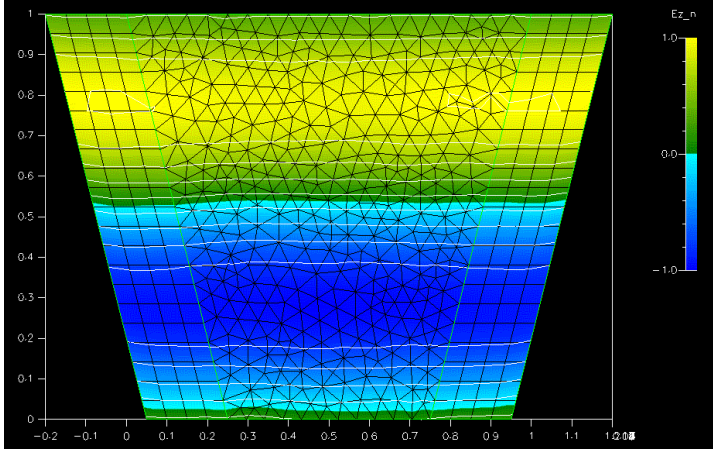


Figure 32. TM wave propagation test in narrowing 2D domain, $\lambda / \Delta x \approx 20$, wave fronts are preserved.

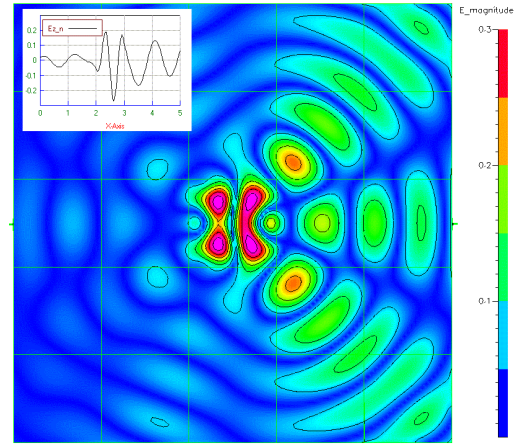


Figure 33. Initial TM wave scattering test on a dielectric square with $\epsilon_r = 4$, solver in total field formulation mode.

Cylinders provide, therefore, an important initial object to study the accuracy of scattering solutions. Ultimately, the systems of interest may contain a large number of scatterers. It is, therefore, of value to find the minimal required mesh density for a desired level of accuracy.

Using a computer algebra system, it is possible to map time-dependent analytical wave solution for complete 2D spaces, including inside materials, and compare these results to FDTD data (Figure 34 through Figure 36). Due to the use of shape-conformal meshes, accuracies on the order of 2% for the steady state field values have been found for a number of cases involving different wavelength-to-scatterer size ratios and permittivities. Gradually, using larger and more complex examples, strong confidence in the solver has been established. A true 3D scattering problem with over 10^6 cells is shown in Figure 37.

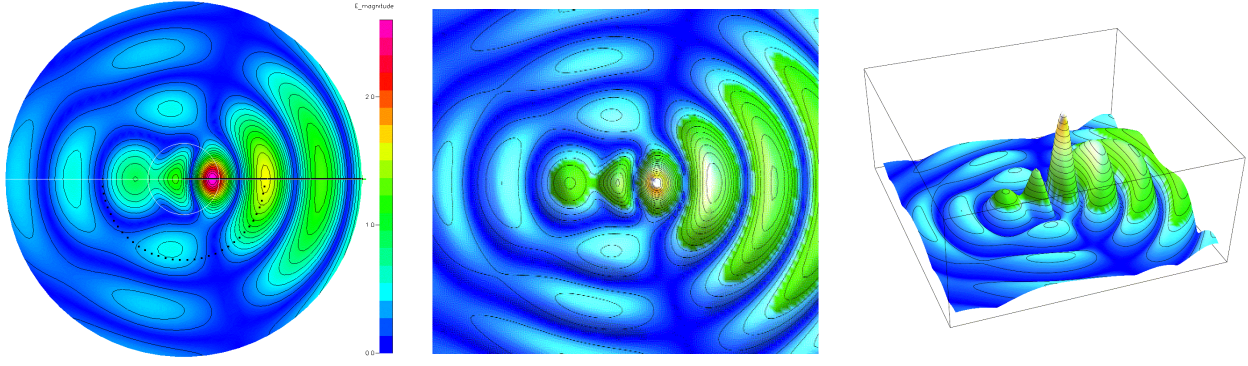


Figure 34. Scattering of a plane electromagnetic wave on an infinite dielectric cylinder with $\epsilon_r=4$, diameter d (normal incident, TM^z polarization, +x-propagation); $\lambda/d=1.5$; (solver in scattered field mode, scattered field plotted) left: FDTD simulation, contour plot of $|E^s(r, \phi, 2\pi \tau/T)|$ at constant, random phase angle τ after steady state is reached; middle: 2D mapping of the analytical solution for $|E^s(r, \phi, 2\pi \tau/T)|$ at same phase angle; right: surface plot of analytical solution for $|E^s(r, \phi, 2\pi \tau/T)|$

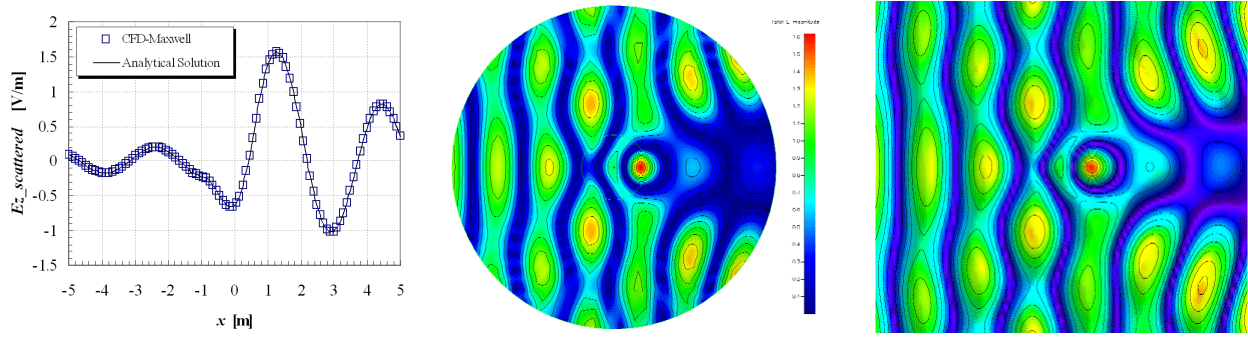


Figure 35. Left: Comparison of analytical and FDTD solution for $E_z^s(x)|_{y=0}$; middle: FDTD simulation, contour plot of total field $|E^t(r, \phi, 2\pi \tau/T)|$; right: 2D mapping of the analytical solution for total field $|E^t(r, \phi, 2\pi \tau/T)|$

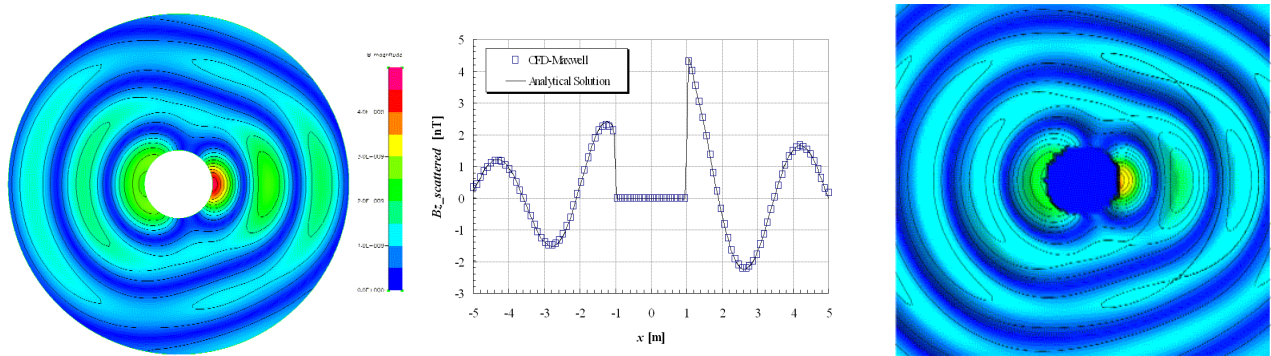


Figure 36. Scattering of a plane electromagnetic wave on an infinite PEC cylinder with diameter d (normal incident, TE^z polarization, +x-propagation); $\lambda/d=1.5$; (solver in scattered field mode, scattered field plotted) left: FDTD simulation, contour plot of $|B_z(r, \phi, 2\pi \tau/T)|$ at constant, random phase angle τ after steady state is reached; middle: comparison of analytical and FDTD solution for $B_z^s(x)|_{y=0}$ at same phase angle; right: 2D mapping of the analytical solution for $|B_z(r, \phi, 2\pi \tau/T)|$

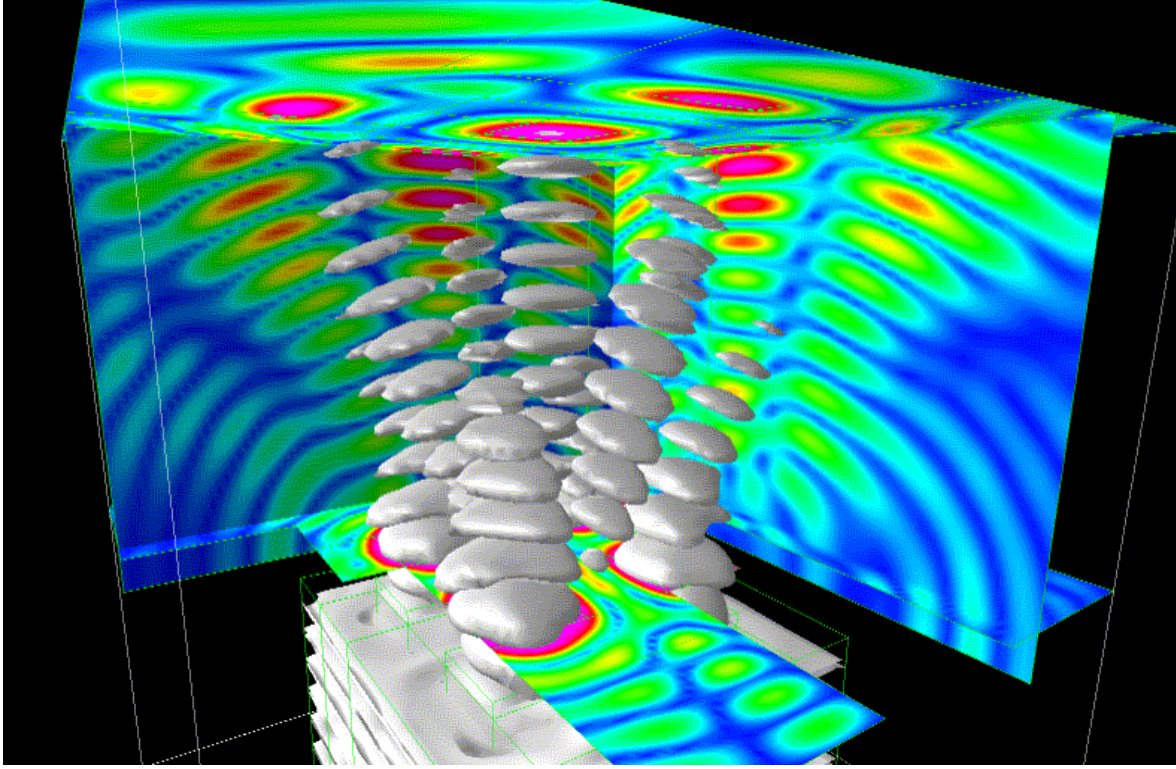


Figure 37. 3D FDTD simulation of the scattering of a TM^x plane wave packet (propagating in $+z$ direction coming from the bottom of the image, gray area) through a 2×2 square aperture array (each aperture's size is $\lambda \times \lambda$); walls: contour plot of $|E'(x,y,z,t)|$, volume: iso-surfaces of $|E'(x,y,z,t)| = 0.4 \text{ V/m}$ illustrating the beam-lets exiting the apertures, notice the formation of the main diffraction maxima in the middle.

3.2 Finite-Volume Magnetic-Vector-Potential based 3D Solver: EMAG

3.2.1 EMAG Solver Modifications (Voltage, Current, Impedance, S-Parameters)

Modifications to the EMAG module in CFD-ACE+ were accomplished, allowing for the monitoring of voltage and current values in three-dimensional simulations. The voltage and current calculations, when activated, are output at the end of each time step in a transient simulation and at the end of a steady state simulation. The output voltage and current values may then be used for impedance and S-parameter calculations.

The voltage and current output may be activated through DTF file updates, activating the voltage and current output capabilities. Voltage is calculated by integrating the total electric field along a line connecting the users desired measurement point and a reference ground point. The current can be calculated in two ways. The current loop technique integrates the magnetic field vector along a loop around the region of interest. The current face technique integrates the total current density vector across an interface. The impedance and S-parameter calculations are calculated using CFD-Maxwell's post processing executables. The techniques are schematically illustrated (along with their basic equations) in Figure 38.

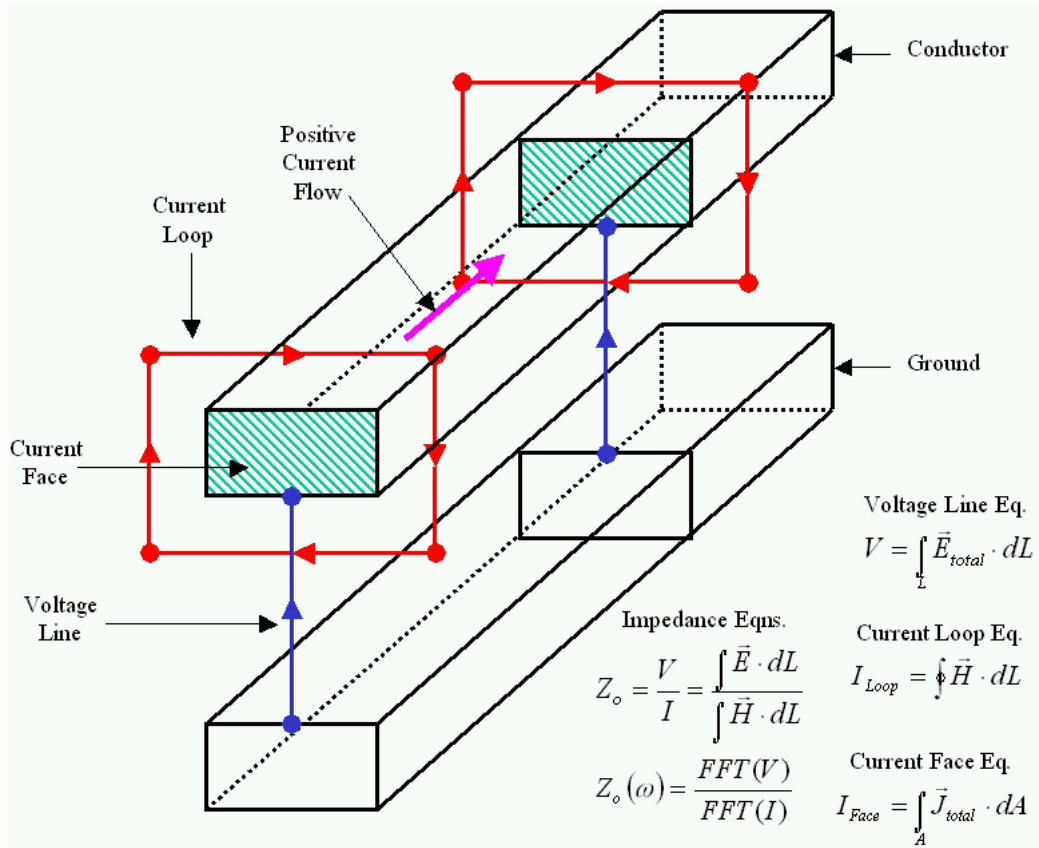


Figure 38. Schematic illustrating voltage lines, current loops, and current faces (basic equations for voltage, current, and impedance are included).

3.2.2 Coupling of 3D EMAG Simulator with SPICE

Under the NeoCAD funding, the new numerical procedures allowing for direct coupling of CFDRC's 3D Electromagnetic Solver (EMAG) with the SPICE circuit simulator were developed, implemented, and tested. The coupling mechanism is illustrated below.

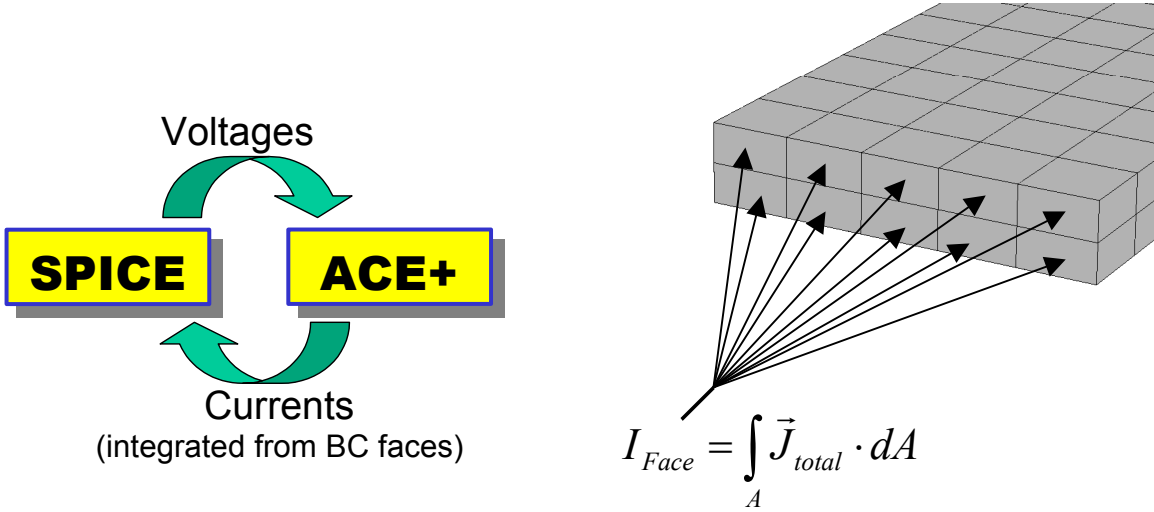


Figure 39. Illustration of the coupling mechanism of CFDRC 3D EMAG simulator with SPICE.

Coupling Algorithm

The coupling of SPICE3 (from UC Berkeley) with CFD-ACE+ Multiphysics Simulator was achieved through a **two-level Newton algorithm**. All ACE models become a new type of element in the SPICE *netlist*. Linearized models of ACE devices are computed by the **CFD-AceSpice** program (described below) at each step. The Jacobian is obtained by numerical perturbations of the ACE solution, or from previous steps.

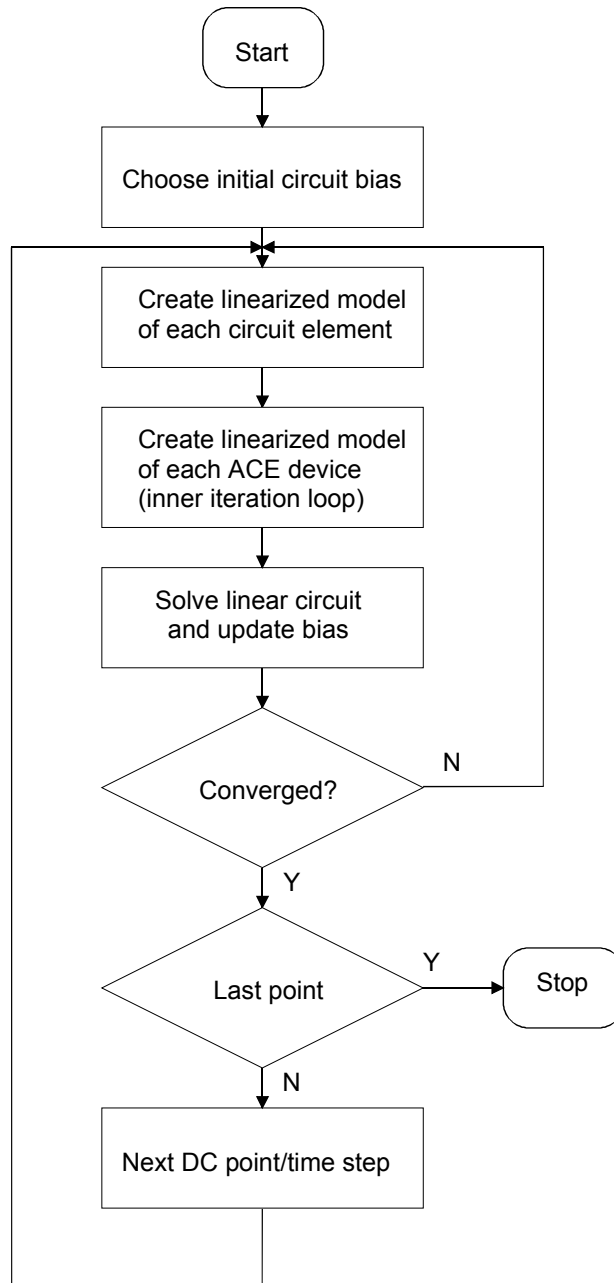


Figure 40. Flow-chart of the SPICE to ACE+EMAG coupling algorithm.

CFD-AceSpice program or “controller”

CFD-AceSpice is the name given to the interface between the CFD-ACE+ and SPICE3 programs. It starts instances of both solvers, co-ordinates information exchange between the two solvers, and directs the progress of the simulation based on the convergence criteria, tolerances etc. specified in the input circuit (.cir) file.

The simulation proceeds as follows:

- CFD-AceSpice starts SPICE3 and ACE solvers. Only one instance of SPICE3 and one ACE instance per A-type device is used in the SPICE netlist.
- The SPICE3 process is always started on the local machine, while ACE programs can be started locally or on a remote server.
- For every time step in a transient analysis (.TRAN), or DC operating point in a DC sweep point analysis (.DC), a Newton-Raphson iteration loop is run until convergence.

This mechanism allows to run simulations of complex circuits described by a SPICE netlist directly coupled with a 3D full-wave EM solution of critical parts (e.g. interconnects, vias, connectors, etc.) of an RF integrated circuits or device. This idea is schematically illustrated below, where driver and termination are represented by SPICE circuit, while the transmission line interconnects are modeled by a 3D EMAG model.

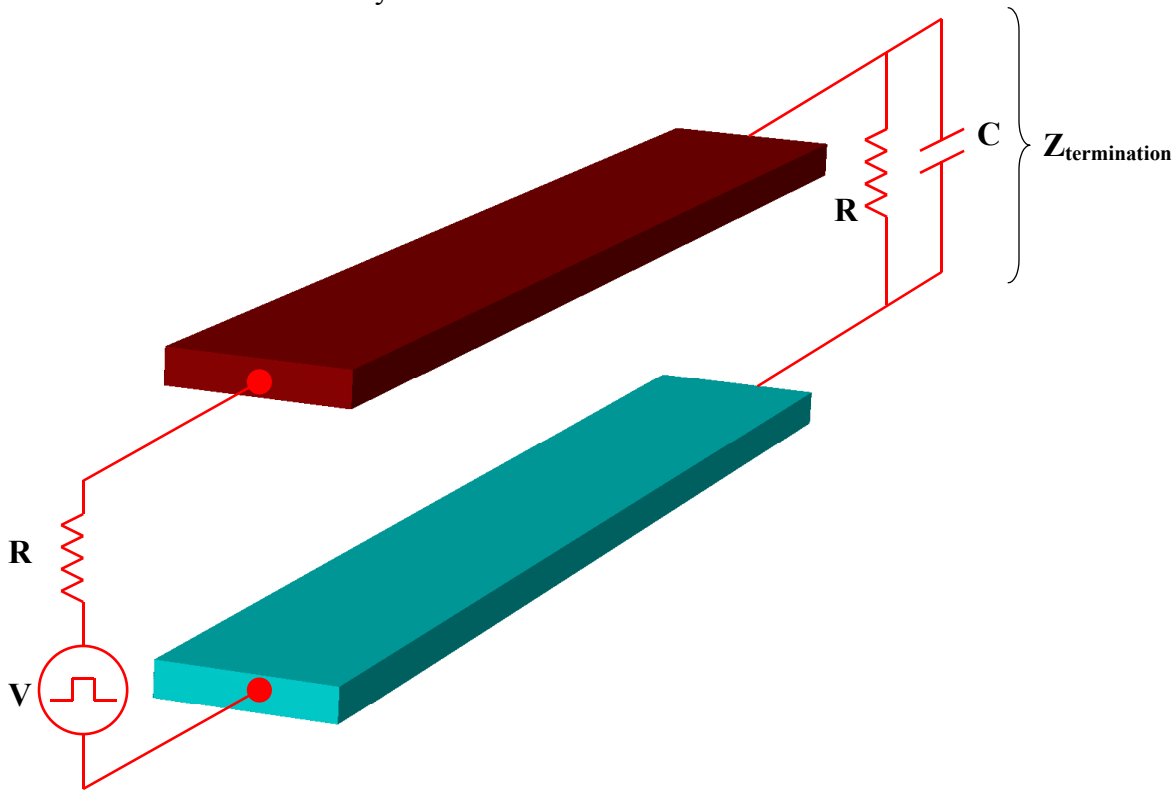


Figure 41. An example of a 3D EMAG model of a transmission line with SPICE modeling the source (driver) and the line termination.

This new EMAG-SPICE coupling software was offered to partners in the NeoCAD program for testing and evaluation.

3.2.3 3D EMAG Simulation of a Parasitic Hanging Stub at Vias in RF PCB Interconnects

The phenomenon: the transfer function of an interconnect trace on a printed-circuit board (PCB) backplane of an electrical system can be severely dumped at some frequency due to a floating via stub which is part of a through-hole via. Most fabricated PCB transition types leave an open via stub (see Figure 42). The problems caused by this parasitic stubs were shown on experimental data of PCB transfer function, presented at 2003 IEEE International Solid-State Circuits (ISSC) Conference in San Francisco, Feb 2003 (Figure 43).

This problem was analyzed in detail during the OE-IDEAS project by the University of Delaware group. A detailed description of different approaches in approximate modeling of the via-stub structure using HSpice models was presented in one of the quarterly reports.

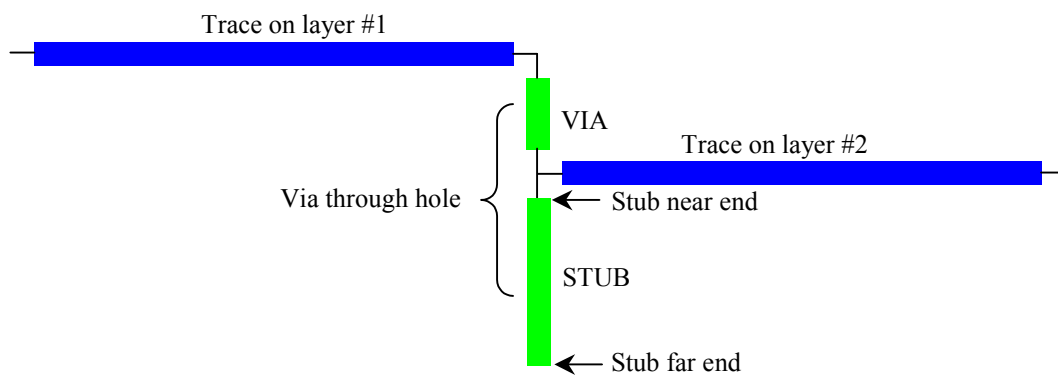
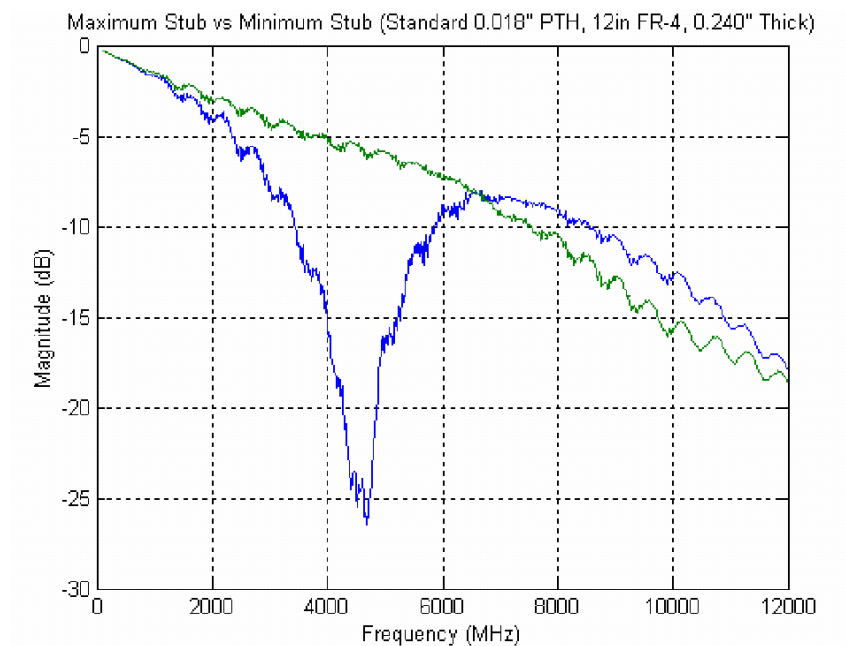


Figure 42. Schematic side-view drawing of a PCB via with hanging stub.



**Figure 43. Measured transfer characteristics (S₂₁) of via with hanging stub [ISSC 2003].
The resonance dip in the blue curve is caused by a long (240 mils) hanging via.**

In this section, we summarize a full-wave 3D electromagnetic modeling of the PCB via with and without parasitic-stub structure using the EMAG tool at CFDRC.

First, a layout of the PCB structure with two transmission lines and via (similar to Figure 42) was drawn in CFD-Micromesh layout editor; see Figure 44.

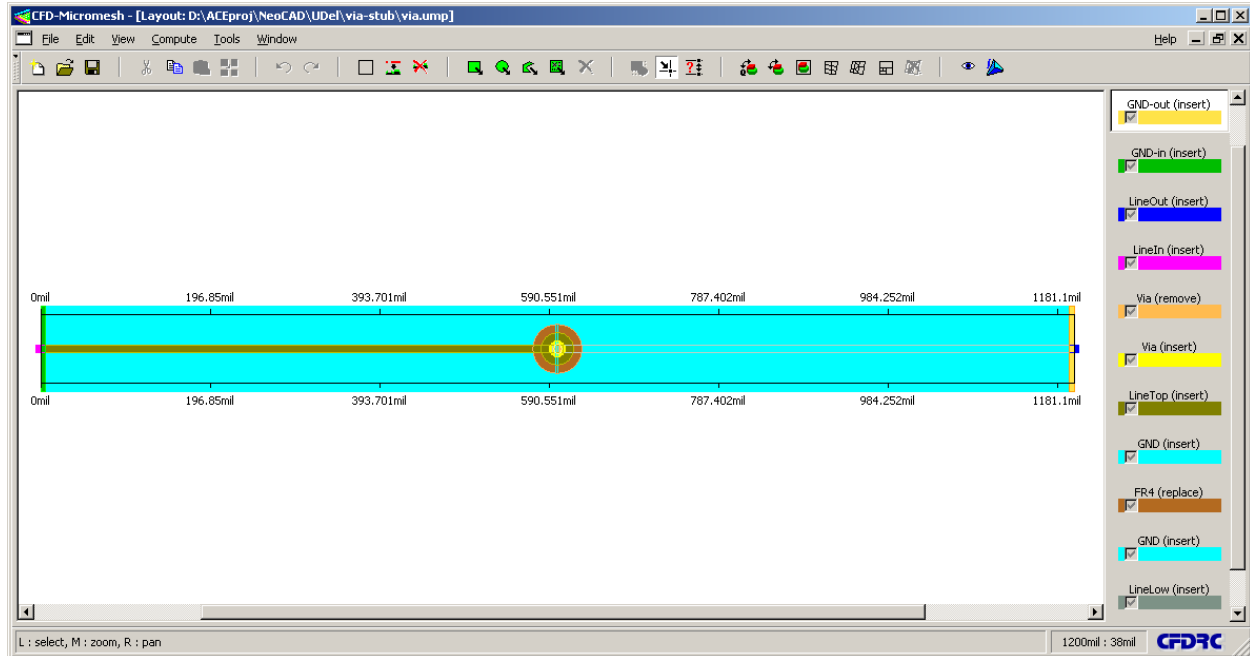
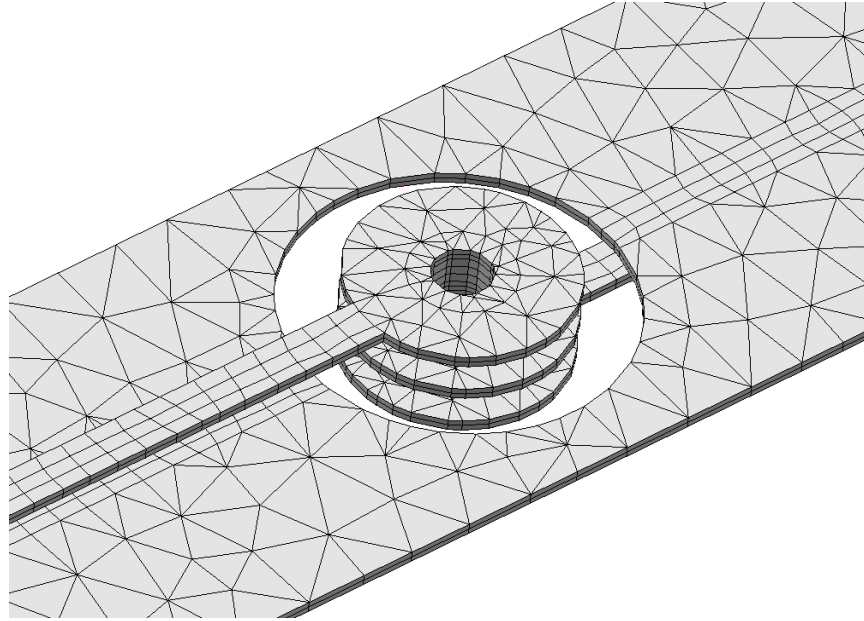


Figure 44. Layout of two transmission lines and via (similar to Fig. 1), drawn in Micromesh.

From this layout, Micromesh built automatically a 3D computational model and 3D mesh from the technology data of the PCB, signal traces, and via, provided by University of Delaware. A close-up view of a fragment of the meshed model is shown in Figure 45.



**Figure 45. A fragment of the 3D meshed computational model generated by Micromesh.
There is a ground plane between signal traces 1 and 2, not shown in Figure 42.**

A Gaussian pulse of 100 ps duration was applied to the beginning of the top transmission line, and transient simulation of signal propagation was performed using the CFDRC EMAG solver. The simulation took about 1 hour on a 2GHz Pentium PC. The resulting voltage and current waveforms were used to calculate the characteristic impedance and S-parameters of the total transmission line, including the via.

Next, we built another model of the structure, this time with the hanging stub below the via. A view of this model with sample results of the electric potential distribution at $t = 1$ ns, are shown in the figure below. This 3D model was much larger, and the simulation with the hanging stub of 240 mils took about 2.5 hours on a 2GHz Pentium PC.

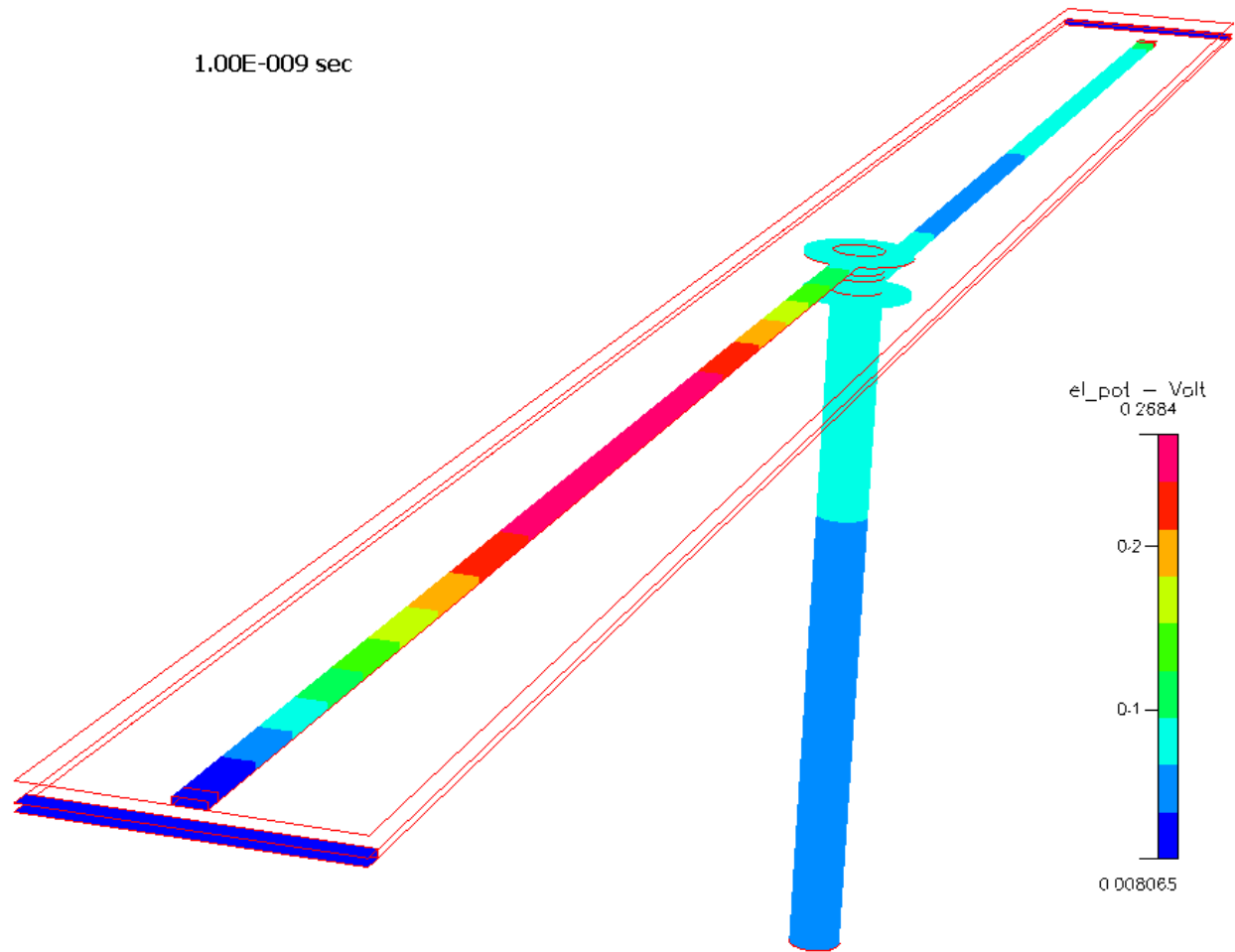


Figure 46. The model of via with the hanging stub (240 mils), with overlaid results of the electric potential distribution at $t = 1$ ns, calculated by transient EMAG simulation. The ground plane and dielectric materials are not shown here for better visibility of the transmission lines.

Also for the second structure, with the hanging parasitic stub, the resulting voltage and current waveforms were used to calculate S-parameters of the entire transmission line. Comparison of the computed S21 transfer characteristics for the cases without-stub and with-stub are shown in Figure 47. The character of the simulated transfer characteristics is similar to the measured ones (Figure 43), however we still need to investigate why our EMAG simulator calculates S21 values greater than 1, which are not physical. The correctness of detailed physical results of EMAG solver is being analyzed now at CFDRC.

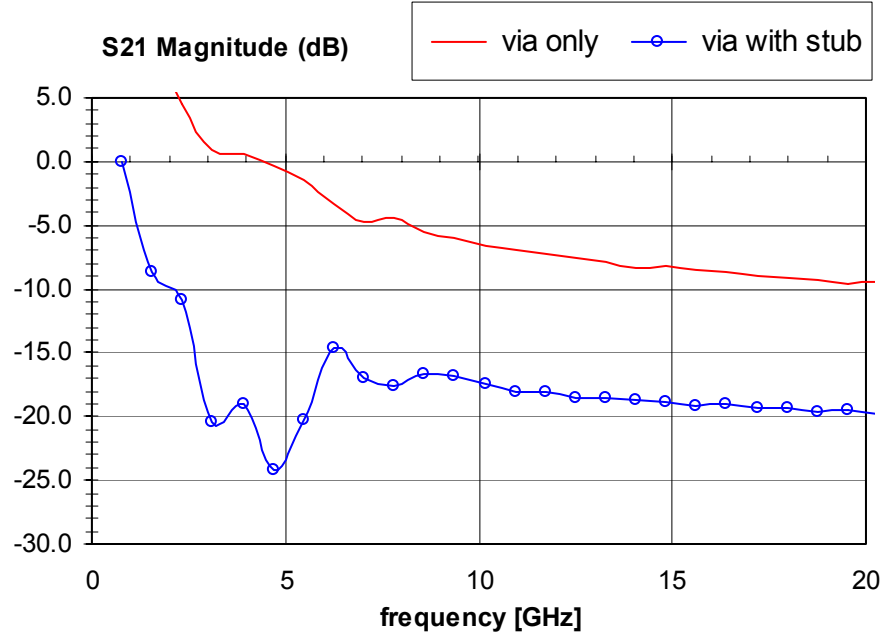


Figure 47. Comparison of the S21 transfer characteristics for the cases without-stub and with-stub, calculated from the full-wave transient results of EMAG simulator from CFDRC.

4 IMPLEMENTATION OF FILAMENT AND WIRE MODELS

In this task, the proposed filament and wire models were being implemented into EMAG, the 3D electromagnetic module of CFD-ACE+. The electric potential is solved in each wire/filament, and their contribution to the magnetic field is fed into the magnetic solver as source.

4.1 Local Subcell Model of Filament in Electromagnetic Module

One of the challenges facing the grid-based numerical model is the distance scale over which physical processes or material properties must be resolved ranging over several orders of magnitude. One has to either

- use a mesh with globally variable array of cells to precisely model the shape and feature of a structure; or
- use a more uniform mesh and approximate the physical properties of the fine spatial details by somehow binding them into the local mesh cells.

The filament model belongs to the second type. The following is to provide insight on how to model the contribution of fine filament to the much larger grid system.

Contribution of Conducting Wire to the Neighbor Cells

To understand the interaction of a current carrying wire or a conductive wire (not active current) with the surrounding meshing, we can start with Maxwell equation

$$\nabla \times \vec{H} = \epsilon \frac{\partial \vec{E}}{\partial t} + \vec{J}$$

where \vec{J} is the total current density, and is equal to $\sigma \vec{E}$ where \vec{E} is

$$\vec{E} = -\nabla \phi - \frac{\partial \vec{A}}{\partial t}$$

where \vec{A} as magnetic vector potential.

For a current carrying wire, the contribution is a source to the local cell with: $\vec{J}_s = -\sigma \nabla \phi$.

For a wire not carrying current, it could behave as an inductor and an capacitor represented by $\sigma \frac{\partial \vec{A}}{\partial t}$ and $\epsilon \frac{\partial^2 \vec{A}}{\partial t^2}$. There is no obvious solution as how the \vec{A} field in the wire and the \vec{A} field in the surrounding medium interacts.

Role as an Inductor

The contribution of inductive property of a conductive wire to the surrounding medium is represented by $\sigma \frac{\partial \vec{A}}{\partial t}$. It is dependent on

- (a) conductivity of the wire, which is typically very high, $6.6 \times 10^6 / \Omega m$ for copper; and
- (b) frequency range $\frac{\partial A}{\partial t}$.

Apparently for high frequencies the inductive contribution can be significant.

Role as a Capacitor

The contribution is $\epsilon \frac{\partial^2 A}{\partial t^2}$ and has more to do with the traveling speed of light. It is significant only if the wave length is compatible with the wire length and when one is interested in the radiation of RF for the connectors. If the interconnect is 1 mm the frequency has to be 300 GHz before this term becomes significant. From this point of view, we can negate the contribution of capacitor of the wire.

How to Solve Vector Magnetic Potential in a Filament

Solving magnetic field inside the conductive wire is not trivial. All boundaries have to exchange information with it neighboring cells. This exchange is diffusive (not convective as in flow or heat). In the convective exchange a source can be applied as

$$a(\vec{A}_{wire} - \vec{A}_{air})$$

For diffusive links it is very difficult to set an accurate link. A good approach is to gain some insight by studying detailed behavior of a wire in a constant time varying magnetic field.

Computational Model

The computational model and grid are shown in Figure 48. The wire has a 50 μm radius and a conductivity of $\sigma = 6.66 \times 10^6/\Omega\text{m}$. The side wall is symmetric and top wall is applied a time varying vector potential of

$$A_z = \sin\omega t$$

and the bottom wall

$$A_z = 0.5\sin\omega t$$

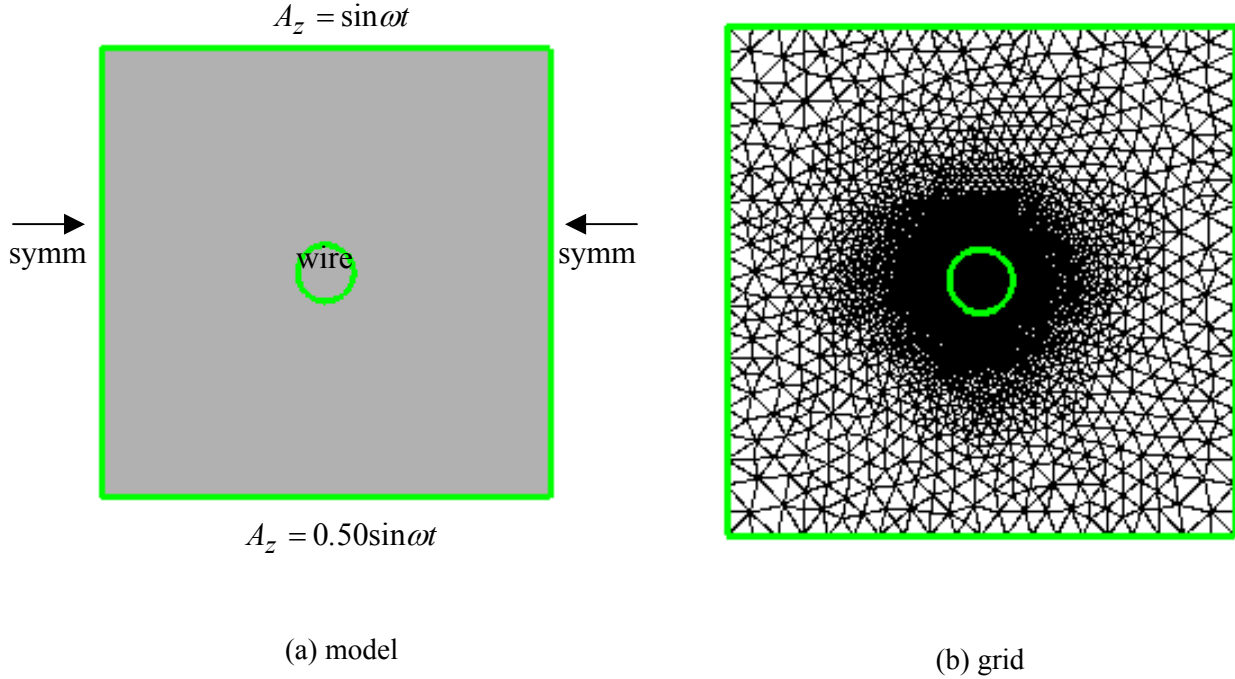


Figure 48. Computational Model of a Conductive Wire in Time Varying Magnetic Field

Figure 49 shows the distribution of vector potential due to the existence of the wire. At low frequency the wire has no affect on the neighboring media. This suggests that we do not need to solve for A in the filament and whole cells can be treated as homogeneous. The \vec{A} value in the filament is the local value.

With increasing frequency, the field around the wire starts to change. What is significant is that at 1MHz the \vec{A} field in the wire is uniform and has value of zero. Filaments with high conductivity and in high frequency conditions behave as “perfect” conductors. The same case was run with the wire removed from the domain, and the boundary specified as perfect conductor. The result shows favorable agreement with those where the wire is included (see Figure 50).

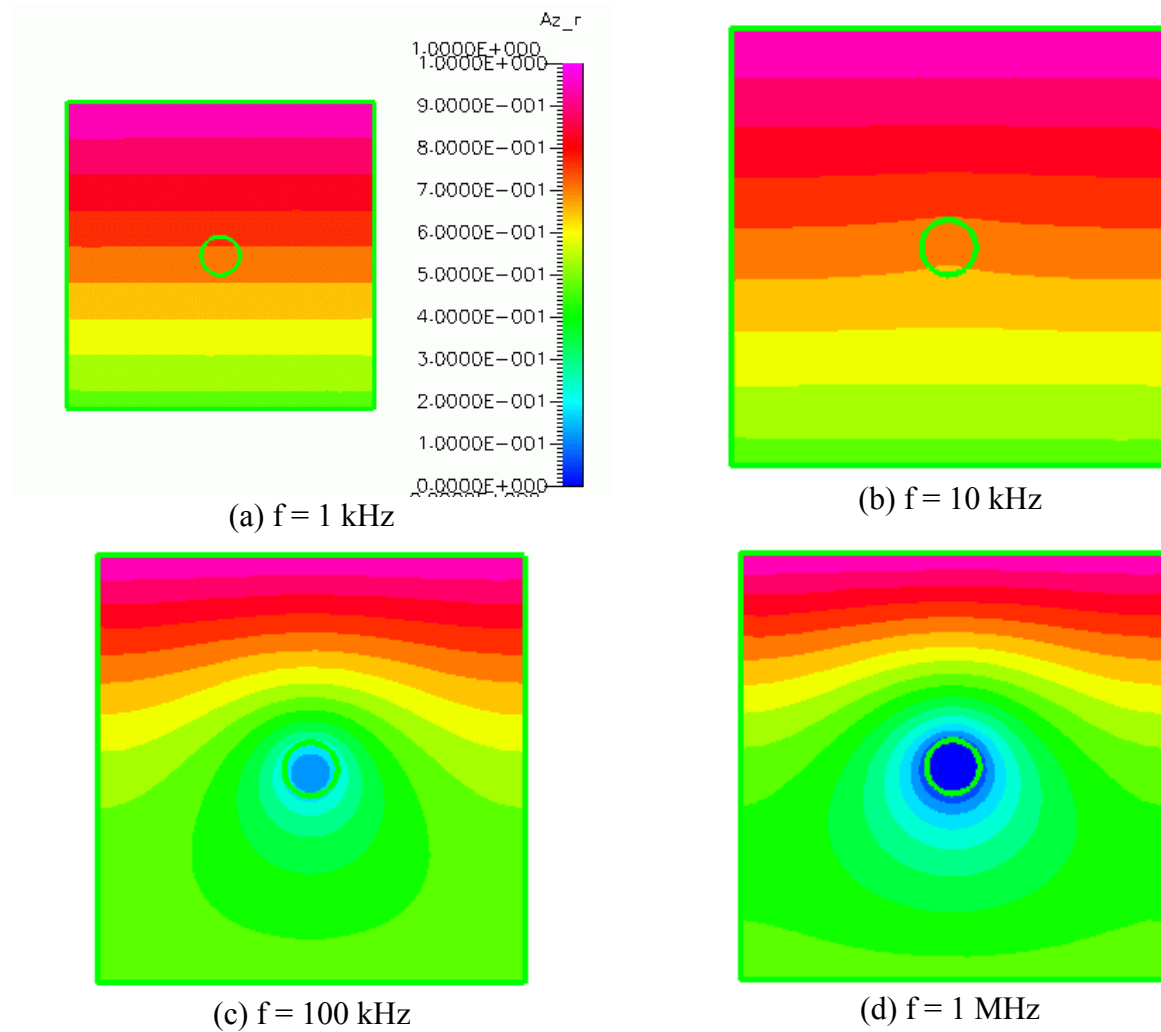


Figure 49. Distribution of a Magnetic Vector Potential Around a Conducting Wire under a Time Varying Magnetic Field

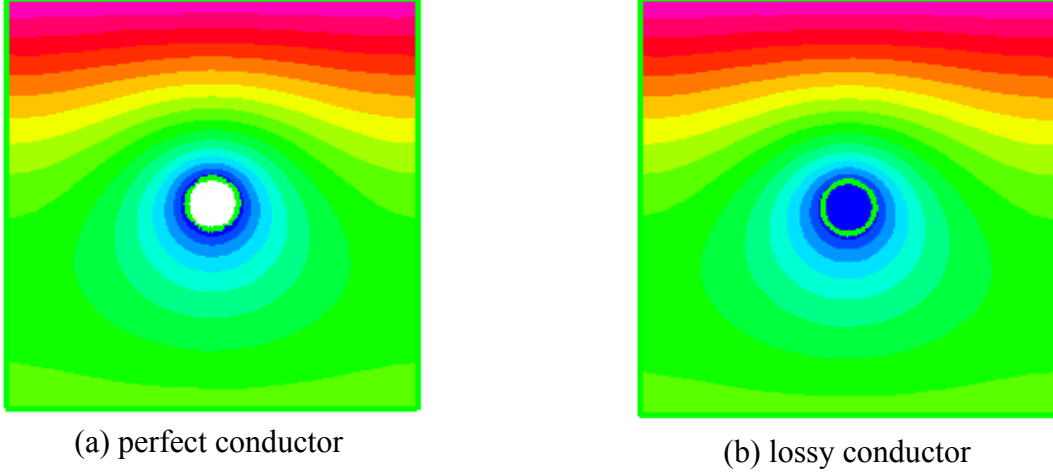


Figure 50. Comparison of Field with Wire Treated as (a) Perfect Conductor and (b) Lossy Conductor

Subcell Modeling of Filament

For the above analysis we can conclude that there is no need to solve \vec{A} field inside the filament. At lower frequencies it will be the same as the neighboring media; at higher frequencies it will be a perfect conductor with $\vec{A} = 0.0$.

Questions remained however as to how we treat the “source” of the filament to the neighboring medium. We proposed to use the linear properties of the Maxwell equation and assume that the total field is the summation

$$\vec{A}_{total} = \vec{A}_{media} + \vec{A}_{filament}$$

Our task was to express $\vec{A}_{filament}$ as an analytical solution with consistent boundary condition. While \vec{A}_{media} is from a solution without existence of the filament.

If we define a local coordinate with $x'y'$ in the cross-section of the filament and z' is along the filament length, the analytical solution is

$$\nabla^2 A_z = 0.0$$

for the cylindrical coordinate

$$\frac{1}{r} \frac{\partial}{\partial r} \left(r \frac{\partial A_z}{\partial r} \right) = 0.0$$

$$A_z = -\vec{A}_{cell} \quad \text{at } r = a, \quad a = \text{radius of the filament}$$

$$A_z = 0 \quad \text{at } r=b$$

The solution to the above equation is

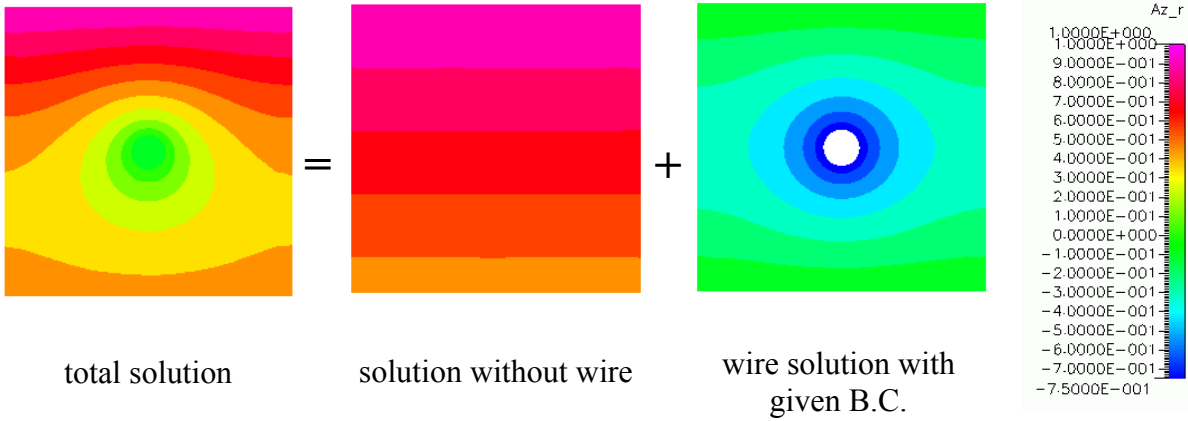
$$A_z = C_1 + C_2 \ln r$$

by substituting the boundary conditions we have

$$\begin{aligned} A_z &= -\frac{\ln b}{\ln b - \ln r} \bar{A}_{cell} - \frac{\ln r}{\ln a - \ln b} \bar{A}_{cell} \\ &= -\left(\frac{\ln b - \ln r}{\ln b - \ln a}\right) \bar{A}_{cell} = -\frac{\ln^b/r}{\ln \frac{b}{a}} \bar{A}_{cell} \end{aligned}$$

\bar{A}_{cell} is the local cell solution for CFD-ACE+. The above A_z represents the contribution of a conducting wire under high frequency.

The above solution will ensure that for $r = a$, $\bar{A}_{total} = 0.0$. We can express the total solution in the following graphic.



Filament Wire as a Source for Electromagnetic Module

In the following, we will show some results from the implementation of the derivation: filament wire behaves as a source to electromagnetic module.

Here the filament will provide a source in the form of

$$\vec{J}_s = \sigma \vec{E} = -\sigma \nabla \phi$$

\vec{J}_s can be obtained by either solving for electrical DC/AC field in the filament, or by prescribed \vec{J}_s vector.

In DC/AC field approach, electrical module has to be activated and we are solving:

$$\vec{\nabla} \cdot \vec{J} = 0.0 \Rightarrow \vec{\nabla} \sigma \vec{\nabla} \phi = 0.0$$

when ϕ is obtained, the electrical field $\vec{E} = -\vec{\nabla} \phi$ can be calculated and hence $\vec{J} = \sigma \vec{E}$.

On the other hand, \vec{J}_s can be specified as:

$$\vec{J}_s = |J_s| \frac{\vec{r}_{axis}}{|\vec{r}_{axis}|} \times \frac{\vec{r}_{coil}}{|\vec{r}_{coil}|}$$

where \vec{r}_{axis} is the vector along the coil axis and \vec{r}_{coil} is any point on the axis to the coil.

Straight Wire

The model is shown in Figure 51. The wire length is 1 and the voltage difference is 1, so that $\vec{E} = 1\vec{z}$. The filament has a radius of 0.1 with conductivity of $10^6/\Omega\text{m}$. The analytical solution is:

$$\text{total } I = A \cdot J = \pi r^2 \cdot \sigma |E| = \pi r^2 \times 10^6$$

and the B field is then

$$B = \frac{\mu I}{2\pi r} = \frac{4\pi \times 10^{-7} * \pi (0.1)^2 \times 10^6}{2\pi r} = \frac{2\pi \times 10^{-3}}{r}$$

We considered only a quarter of the computational domain. Three grids were considered: 50x50x10, 25x25x10, and 15x15x10. The grid sizes were 0.1, 0.2, 0.33, respectively.

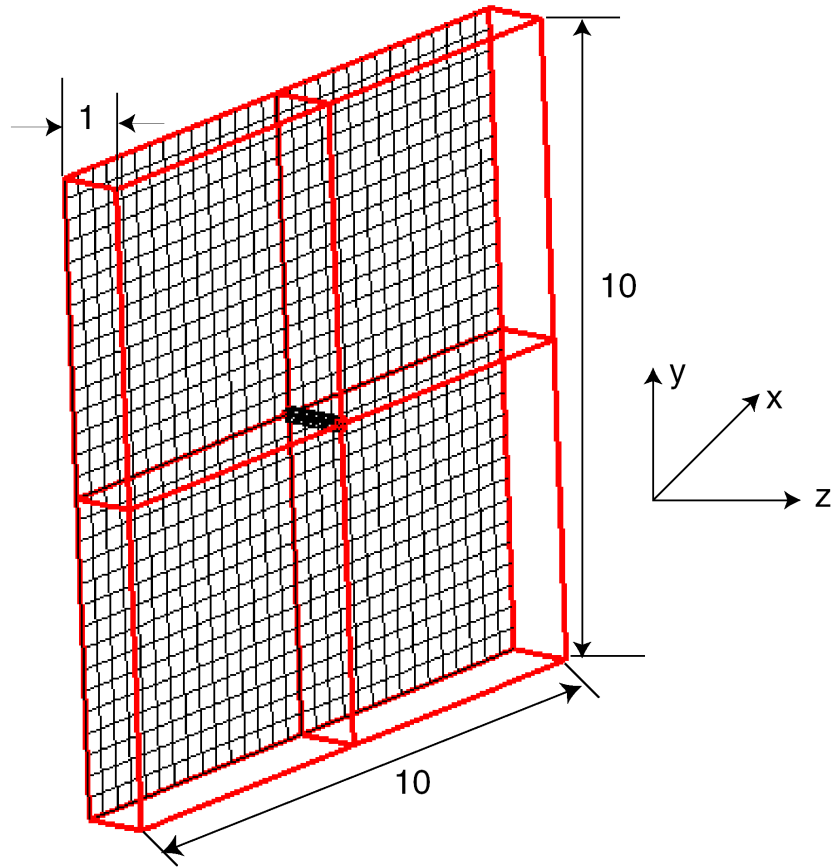


Figure 51. Computational Model for a Straight Wire

Figure 52 shows the potential distribution along the wire and the magnetic vector around the wire.

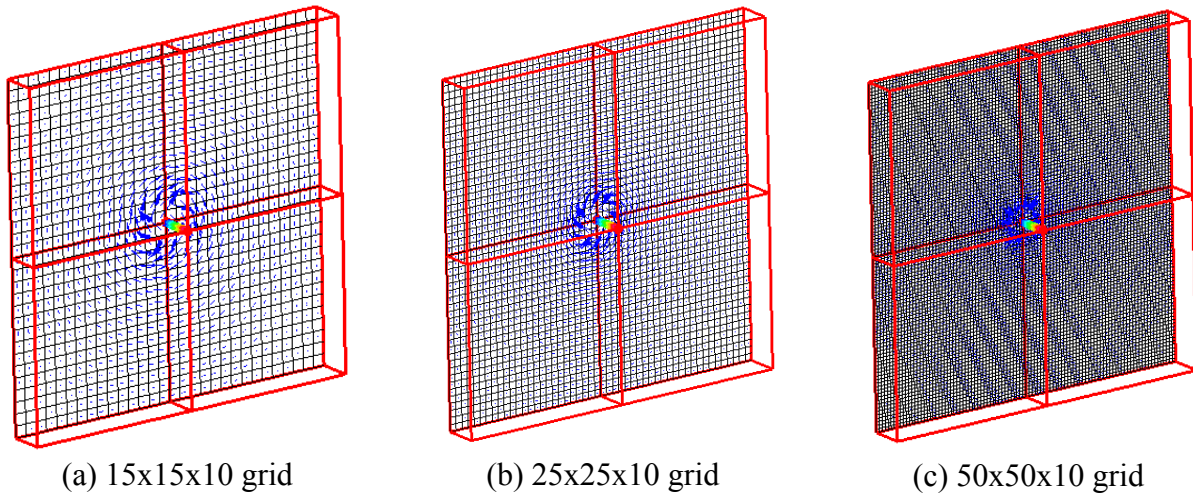


Figure 52. Magnetic Vector Around a Current Carrying Wire

Comparison with analytical solutions are shown in Figure 53. Note, except for the first point which contains the filament, the solutions match with the analytical solutions exceptionally well. The inaccuracy in the first point is due to:

1. It is the average solution over the first cell. This cell contains the wire contribution, but it could not resolve the detailed wire contribution.
2. Magnetic vector is $\nabla \times \vec{A}$, which depends on the local solution \vec{A} . If \vec{A} is off, so is $\nabla \times \vec{A}$.

In conclusion, the filament model can provide an excellent alternative for complex geometry of wire without sacrificing accuracy away from the wire.

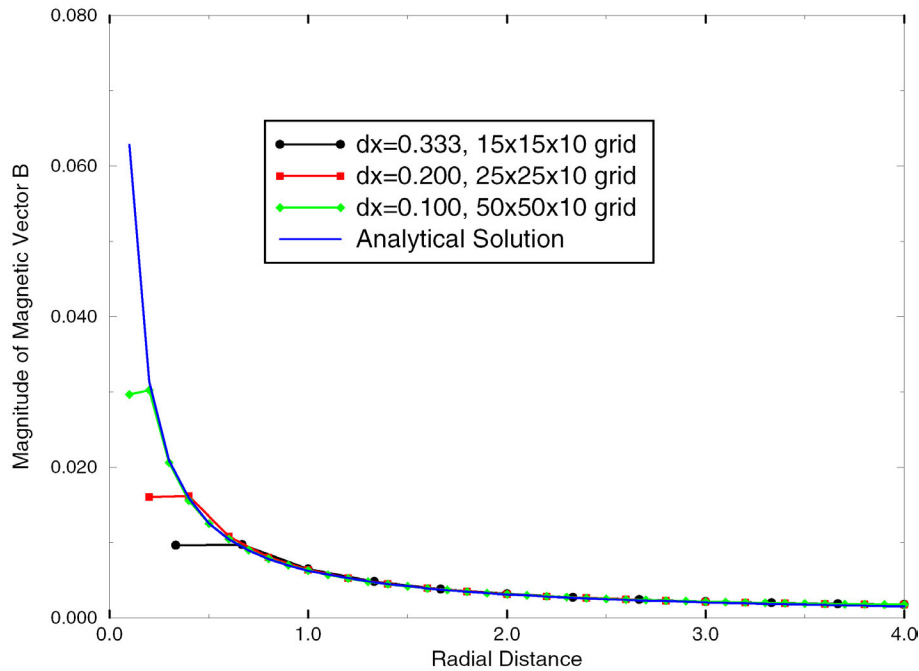


Figure 53. Comparison of Magnetic Field

4.2 Modeling of Interaction between Filament and 3D EM Field

A 3D model was built and run to validate the magnetic source through electric current in a straight wire. The purpose was to give a general idea on how the two are coupled. The sample configuration is shown in Figure 54 below, along with the calculated resulting magnetic field vectors.

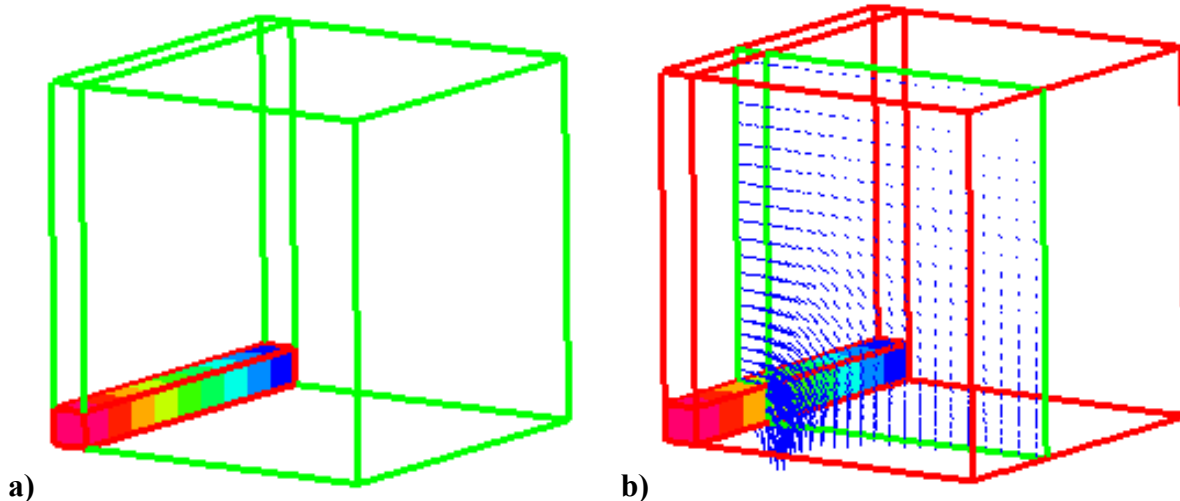


Figure 54. a) Distribution of voltage due to conduction current in a wire. b) Magnetic field vectors resulting from the conduction current in a wire.

The idea was to use relatively large grid, yet at the same time to be able to resolve the sub-cell scale physics due to one or more conducting wires.

Inductive Current in a Wire due to Time-Varying Magnetic Field

A more general case was tested with fine scale model for detailed inductive current of three conductors near one conductive wire, see the figure below. This kind of structure is quite typical for multi-layered VLSI interconnects.

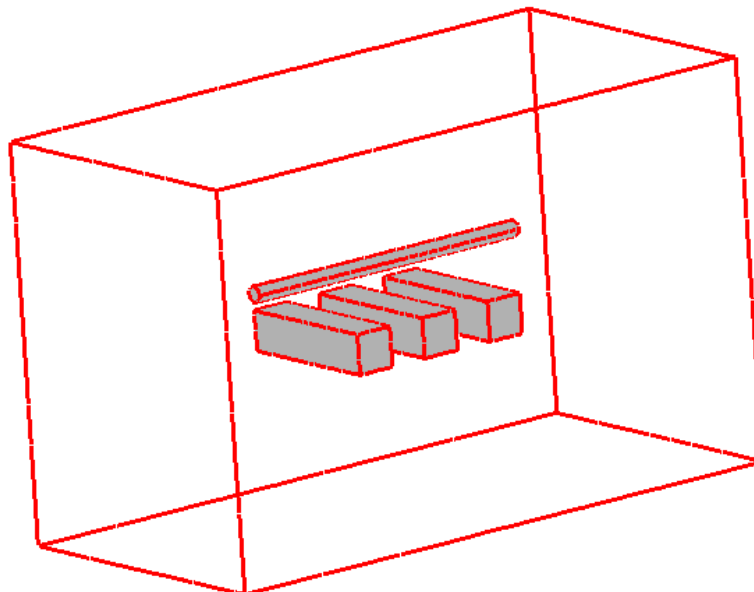


Figure 55. A geometrical setup to investigate inductive influence of one wire on its neighbors.

AC current was applied to the top wire (circular cross-section), while we wanted to investigate the induced current in its neighboring conductors (square cross-section). We hoped it would shed

light on how to model the inductive effect of a fine wire, or multiple wires, in a large control volume. The calculated current vectors induced by the current flow in the top wire are shown in the figure below.

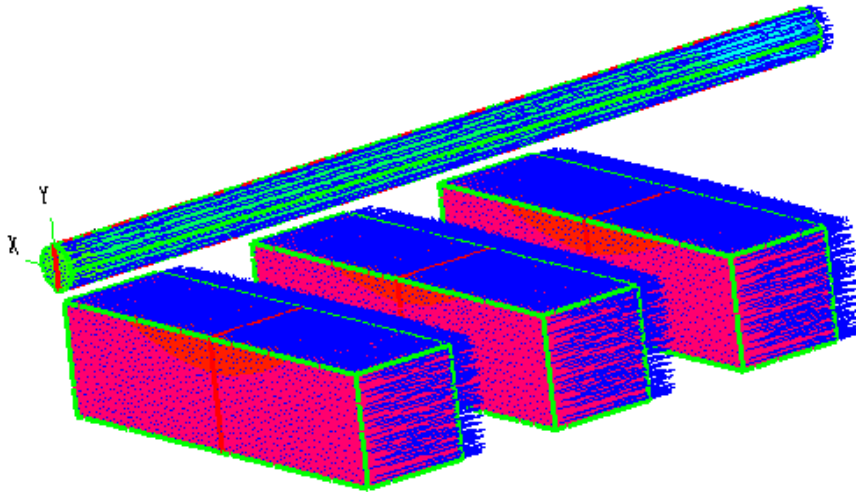


Figure 56. Computed current vectors induced by the current flow in the top wire.

EMAG Examples

The multi-filament model can be used for all kind of diffusive physics, including the electromagnetic vector potential solved by the EMAG module of CFD-ACE+. The new multi-filament diffusion model was tested against magnetic field problems. Electromagnetic field in a square background with 3 thin wires (magnetic field is generated by AC current in one of the thin wires) was simulated with:

- 1) A multi-domain direct grid approach;
- 2) Single-filament model with fine grid;
- 3) Multi-filament model with fine grid;
- 4) Single-filament model with coarse grid;
- 5) Multi-filament model with coarse grid;

The grids used in the computation were the same as in the test heat transfer problems. With fine grid, each cell has at most one filament. With coarse grid, all 3 filaments are in the same cell. The AC frequency is 1000 Hz, the wire cross-section is $0.04 \times 0.04 \text{ m}^2$, and the original current density is 1000000 A/m^2 .

Figure 57 shows the typical magnetic field calculated using the direct grid approach. Figure 58 compares the magnetic fields along x-axis for all the 5 cases. Table 1 compares the induced current for all the cases.

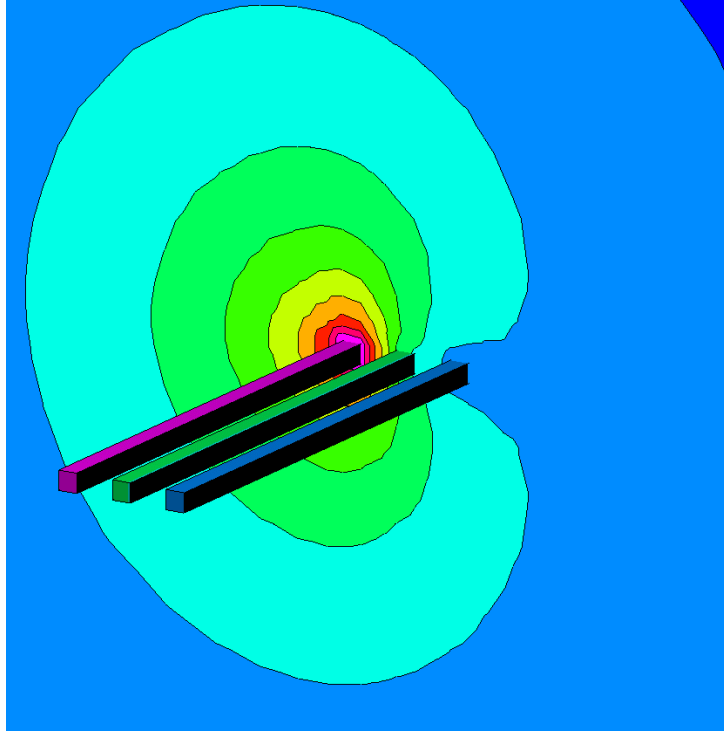


Figure 57. Typical magnetic field induced by one of 3 wires in a transmission line.

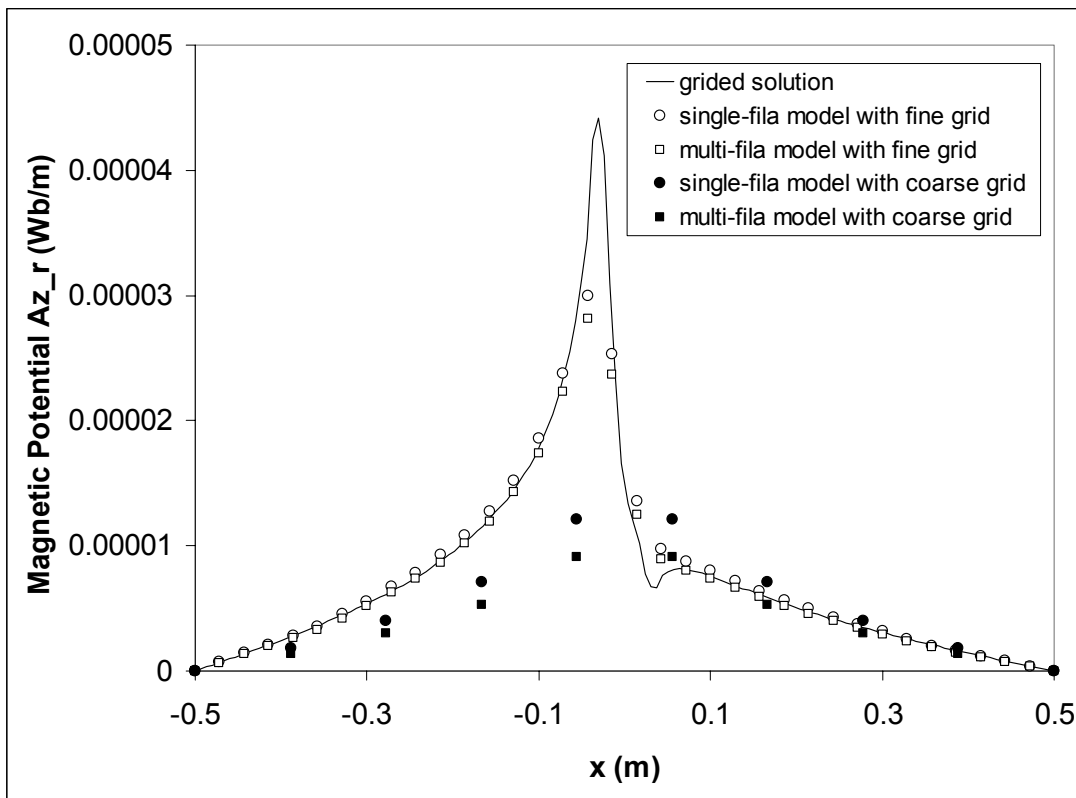


Figure 58. Comparison of simulation results of magnetic fields along x-axis for 5 cases of single- and multi-filament models, with fine and coarse grids.

Table 1. Induced current (A/m²) for 5 cases of single- and multi-filament models, with fine and coarse grids

	1 st wire (source)	2 nd wire	3 rd wire
Grid solution	485672	205044	146204
Single-filament model with fine grid	508451	194500	136805
Multi-filament model with fine grid	465474	203200	145794
Single-filament model with coarse grid	573793	232000	131679
Multi-filament model with coarse grid	425276	210498	210498

Simulation results show that the multi-filament solution is close to the grid solution, and the single-filament model solution when the grid is fine enough. For very coarse grid, when multi-filaments occupy the same background grid cell, the multi-filament model solution has the similar overall accuracy as single-filament model in the far field, and both are a little bit off the grid solution. However, the multi-filament solution can reproduce the local variations of the filaments within the same cell, which cannot be resolved with single-filament model.

5 AUTOMATIC 3D MODELING AND MESHING FROM IC LAYOUTS: CFD-MICROMESH

During the DARPA/MTO TEAM/NeoCAD Summer Project Review, Aug 27-29, 2002, in Providence, RI, several teams indicated the need for, or planned the development of, grid generation tools. The round table discussion, organized by DARPA PMs and DoD PMs, with NeoCAD PIs, indicated that an automated geometry modeling and meshing tool, working directly from electronic layouts, could be of great benefit to most of the teams. A common tool could save development costs, reduce development time, enable communication between different tools, and could simplify the design task of other DARPA programs, e.g. TEAM, MEMS, WBSG, and others. In the previous couple of years, DARPA Composite-CAD program partially sponsored CFDRC for the development of the Micromesh code for MEMS modeling. It was expected that with a possible modest enhancement effort the Micromesh could be used by all NeoCAD teams as well as DoD agencies. A document summarizing those discussions has been prepared by John W. Rockway, SSC-SD, and Andrzej Przekwas, CFDRC, and distributed to all the interested NeoCAD participants. After that, we discussed internally at CFDRC the challenge of providing CFD-ACE+ and Micromesh to the DARPA teams. After the NeoCAD Review in Providence, and subsequent exchange of emails within the interested group of NeoCAD members, CFDRC made substantial progress in resolving both the issues.

As far as Micromesh is concerned, CFDRC made the following progress:

- improved the automating meshing quality from imported GDSII and CIF layouts,
- implemented better handling of large layouts,

- improved and simplified API to DTF mesh files to extract FEM (volume) and BEM (surface) type meshes,
- a new, detailed tutorial how to use Micromesh effectively for NeoCAD benchmark example cases, was prepared and distributed to all interested NeoCAD members (see below selected illustrations from the new tutorial).

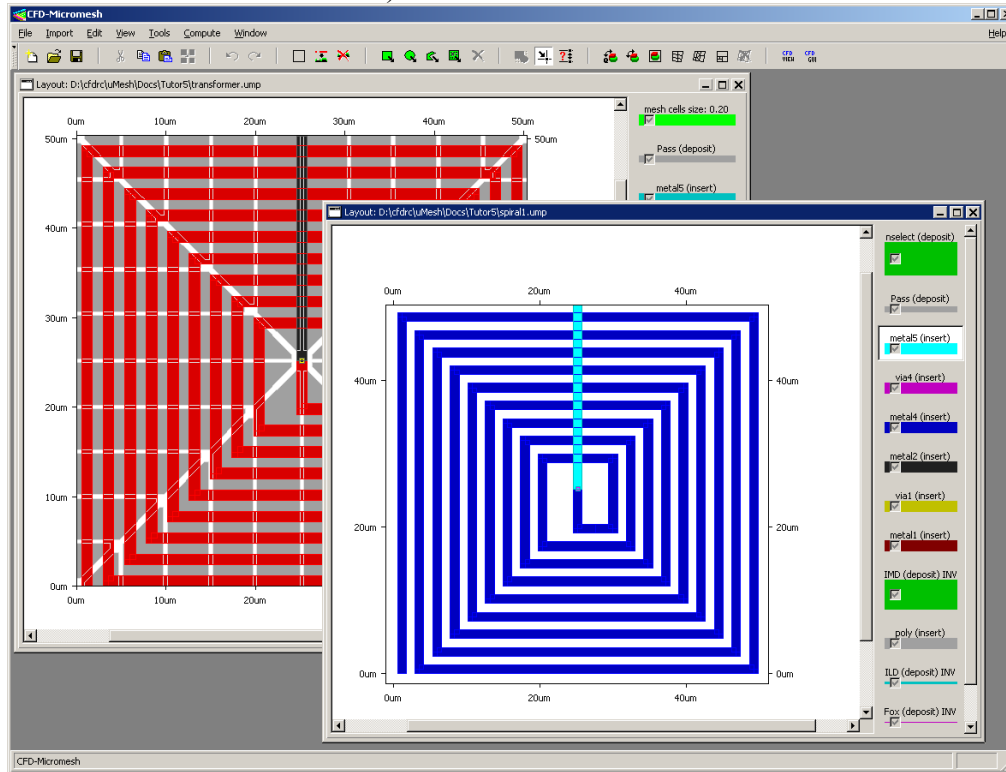


Figure 59. Example from the new Micromesh Tutorial, the Spiral Transformer (built of two spiral inductors): two separate GDSII layouts imported into Micromesh from *coupled.gds* file provided by NCSU as a NeoCAD benchmark.

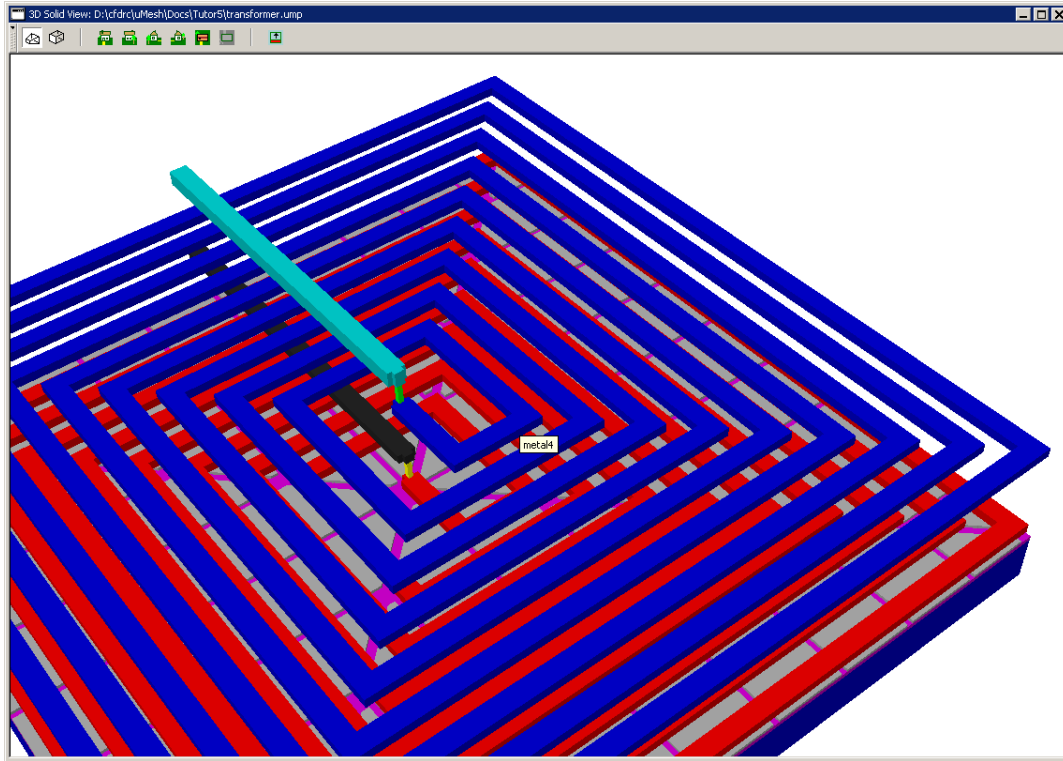


Figure 60. 3D solid model of the NCSU Spiral Transformer, built automatically from layout in Micromesh.

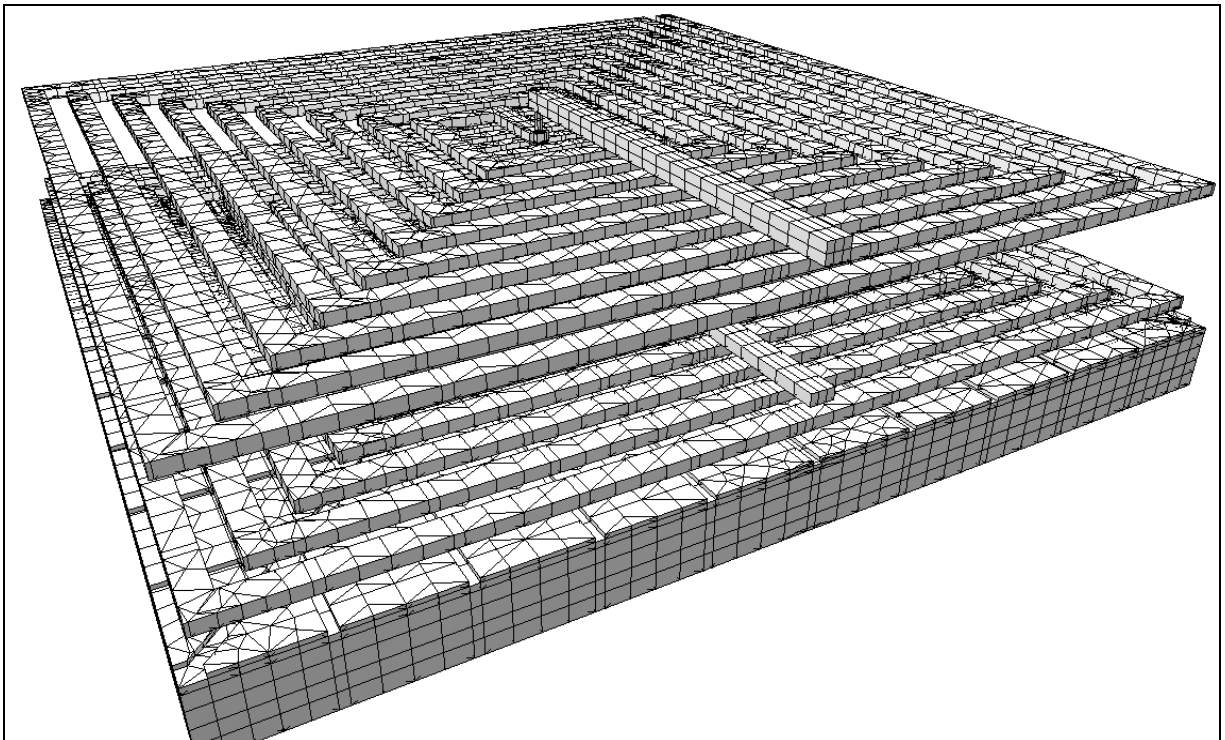


Figure 61. 3D prism-hex mesh built automatically from layout in Micromesh.

We obtained excellent feedback from Andreas Cangelaris' University of Illinois group, and several other NeoCAD PIs, in particular the University of Washington team, i.e., University of Washington (Vikram Jandhyala) and Lawrence Livermore National Laboratory (Dan White).

In January 2003, CFDRC received from John Rockway an interesting report “**Comparison of Tools for DARPA CoSMoS mesh generation**” containing collection of observations of meshing tools applied to NeoCAD problems. The observations were from University of Washington and Lawrence Livermore National Laboratory.

Below is a summary of **CFDRC's Response and Comments to this report** (in the frames are extracted relevant fragments from the original report):

	Coventor Designer	Commercial Mesher	CFDRC Micromesh
speed of defining geometry	good	adequate	very slow ; volumetric extrusion is the bottleneck

CFDRC Response:

- The “volumetric extrusion” is relatively slow in Micromesh only for non-rectangular shapes in masks, when millions of fine voxels must be used on large areas. If layout masks contain rectangular shapes only, then voxels are not used at all, and the 3D model generation is much faster.

meshing speed	good	good	slow . However, it takes more man-hours to "get ready to mesh" than it takes to numerically generate the mesh.
---------------	------	------	---

- A totally new algorithm and procedures for prism-hex mesh generation in **Micromesh** have been implemented and completed in 4th qtr 2002. The meshing speed **is more than 2 orders of magnitude faster now!** Moreover, the resulting mesh quality is much better, where the minimum angle in all triangles can be controlled (typically now the min. angle is > 10 deg).

API available	no	simple enough to reverse engineer	no
---------------	-----------	-----------------------------------	-----------

API available	Is it possible to access the meshing routines from library with a well-documented Application Program Interface? Failing that, is it possible to call the mesher from the command line?		
---------------	---	--	--

- Also in 4th qtr 2002, CFDRC completed the implementation of **a new API and a Python-based scripting**, which allows **access to all the Micromesh functions**, including importing layouts, geometric model building, and all the meshing routines. The documentation is being currently prepared.

Moreover, **it is possible to call the mesher from the command line**, with parameters like layout file (GDSII or CIF), technology file, etc.

These new capabilities allow to use Micromesh in an EDA-style design flow, controlled by external tools.

- | | |
|----|--|
| 3. | Often, it has been necessary to manually replace GDSII coordinates with "hand-typed" coordinates, rounded to some tolerance, in order to generate an acceptable mesh. We do not know if the problem has been with the GDSII input or if it is a problem with Micromesh. In either case, it would be beneficial to have a "snap-to-grid" capability for imported geometries, e.g. round all geometry coordinates to a specific tolerance. It should be noted that we recently received a Micromesh upgrade that has a new procedure for tolerancing, this has not been evaluated. |
|----|--|

- **The "snap-to-grid" capability** for imported geometries, that is rounding all geometry coordinates to a specific tolerance, **has been implemented** in the new version of Micromesh (available in the upgrade package sent to LLNL on 1/20/03). This **facilitates fixing of the "bad" GDSII layouts** which have traces that should be joined, but are not quite, etc.

- | | |
|----|---|
| 6. | The "cut and paste" capability of Micromesh is limited in that it only works for a single layer, i.e. it is difficult to replicate a multilayer geometry. |
|----|---|

- The **capability to "cut and paste" or "copy and paste" for multiple layers at the same time has been implemented**, and is currently available in Micromesh (since March 2003).

New licenses of CFDRC software, including Micromesh, were provided with no charge to Univ. of Cincinnati (Ranga Vemuri), Univ. of Illinois (Andreas Cangellaris), University of Delaware (Fouad Kiamilev's group), and University of Washington (Richard Shi's group) for NeoCAD applications and interoperability studies.

The **overall progress of the CFD-Micromesh tool** during the DARPA NeoCAD program is illustrated below.

Examples of building time of high-resolution 3D model and mesh
in progressing Micromesh technologies

	32-lines interconnect structure	64-lines interconnect structure
Micromesh 1.4 (2000)	120 minutes (7200 sec.)	∞ (impossible with voxels)
Micromesh 2.0 (2001)	2 minutes (120 sec.)	10 minutes (600 sec.)
Micromesh 2003 (May 2003)	2 seconds	10 seconds

**3500X
faster!**

**New
techno-
logy!**

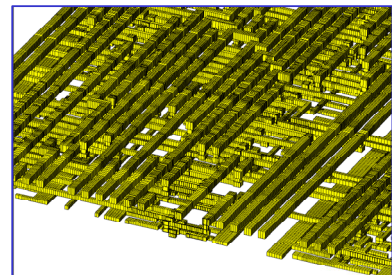
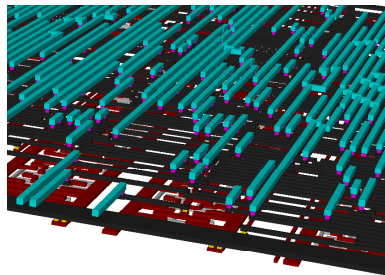
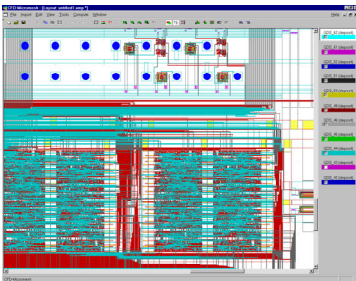


Figure 62. Overall progress of the CFD-Micromesh tool during the DARPA NeoCAD program.

New Micromesh Applied to Another NeoCAD Benchmark

The newest Micromesh version, including all the newly developed technologies mentioned above, was applied to another NeoCAD Benchmark: UW-SOI-QVCO placed on the DaVinci site by University of Washington (UW). This is an SOI quadrature voltage-controlled oscillator (QVCO) with three inductors placed at varying distances to test magnetic coupling effects on VCO phase noise performance. The layout proposed by UW is presented below.

5.6GHz Quadrature LC Oscillator Layout

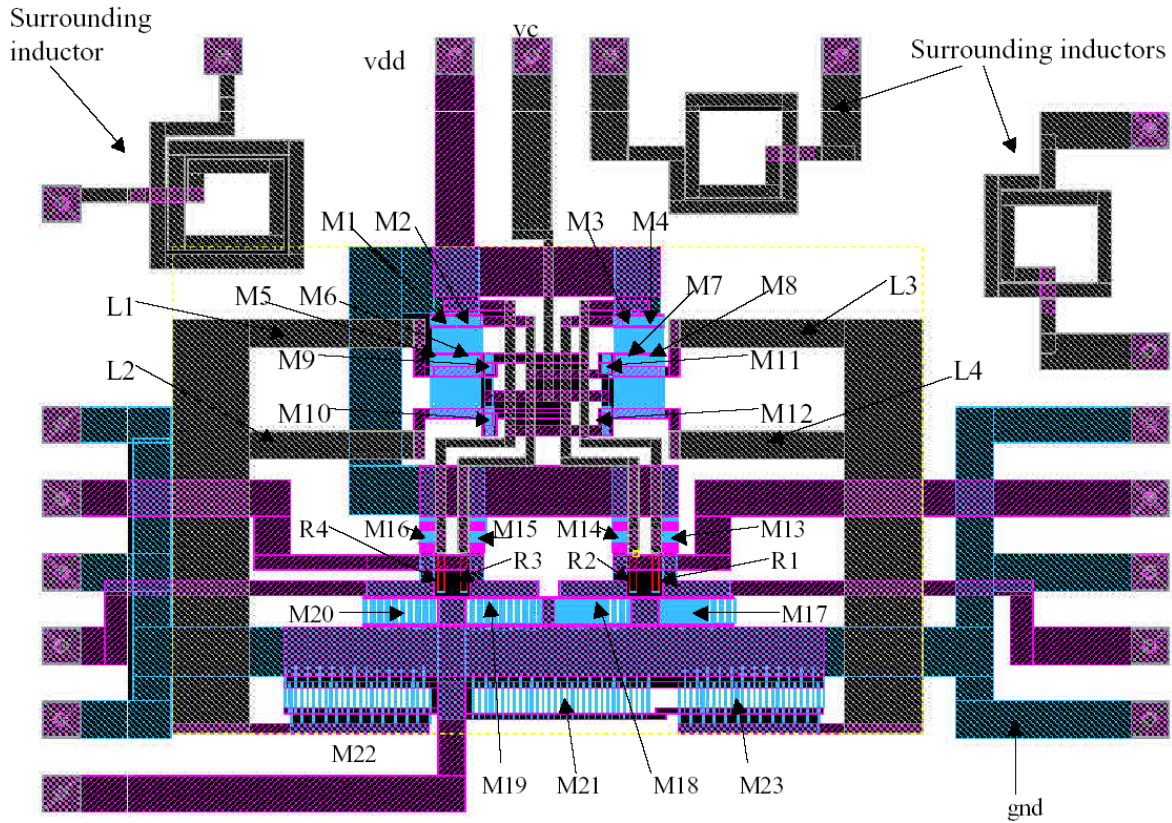


Figure 63. NeoCAD Benchmark layout: UW-SOI-QVCO from University of Washington.

The GDSII file provided by UW in the benchmark set was imported into Micromesh, and a 3D model was built, which is shown below.

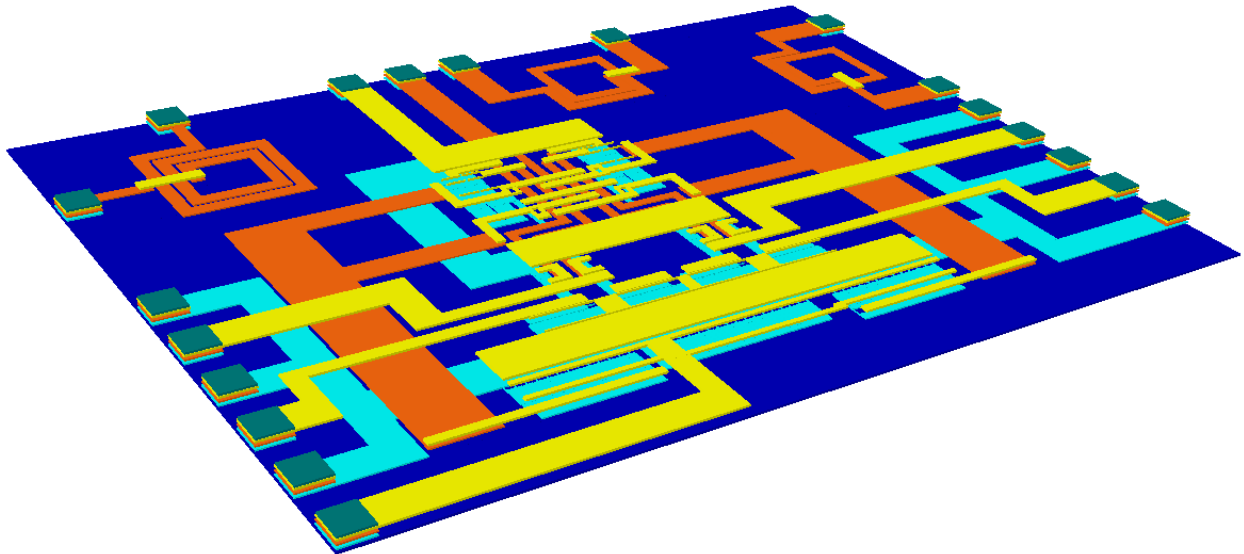


Figure 64. The UW-SOI-QVCO benchmark 3D model, automatically built from the GDSII layout, using the new Micromesh capabilities.

Next, using the new Micromesh, we generated automatically a 3D structured mesh, fragment of which is presented below. It is a quite regular, hexagonal mesh, which is quite convenient for many electromagnetic solvers.

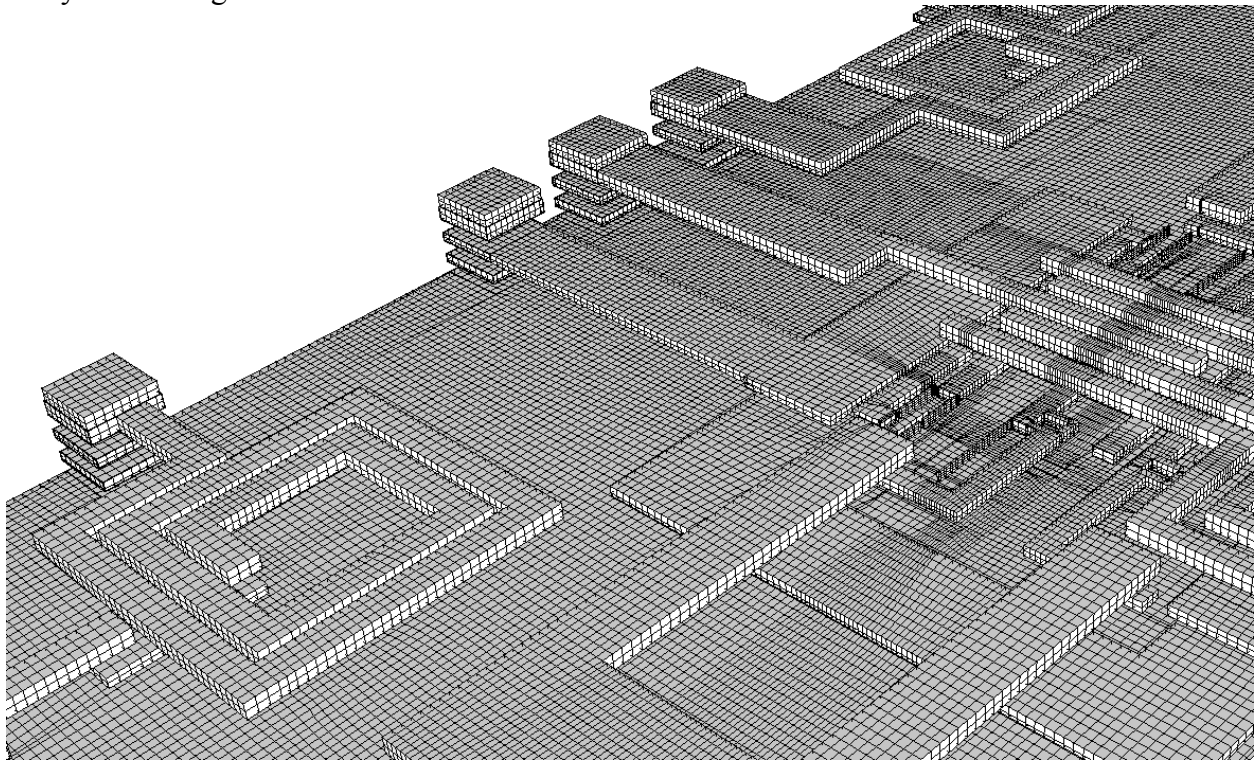


Figure 65. A 3D structured mesh generated automatically by Micromesh from UWB layout.

Summarizing, Micromesh became during the NeoCAD Program a very useful tool for automatic generation of complex 3D models and computational mesh from layout formats used in EDA community (GDSII and CIF). Micromesh has been successfully used by several NeoCAD teams and has become an indispensable component of full-wave EM modeling software in several NeoCAD design tools (e.g. Orora, LLNL, U. Wash., U. Pitt., SUNY, and others).

6 VHDL-AMS COMPACT MODELS OF O/E DEVICES

Task led by University of California, Santa Cruz, PI: Prof. Steve Kang

During the NeoCAD OE-IDEAS effort, we developed, implemented, and tested compact models for various opto-electronic (O/E) devices, with the aim of creation of a model library for mixed-level mixed-technology simulations. The new models were demonstrated through example VHDL-AMS simulations. The following O/E devices were addressed and tasks accomplished.

6.1 VCSEL and Transmitter (VCSEL and a CMOS driving circuit)

- Developed a behavioral VHDL-AMS model of VCSEL;
- Implemented the model into SMASH from Dolphin Integration;

- Tested the VCSEL model by time domain simulation of different devices;
- Simulated a simple transmitter consisting of CMOS driving circuit and VCSEL.

Automation of O/E behavioral model parameters extraction:

- Finished the linear part of VCSEL behavioral model parameter extraction using Python;
- Implemented a nonlinear behavior model parameter extraction algorithms for Python.

6.2 Metal-Semiconductor-Metal (MSM) Photodetector

- Developed a behavioral VHDL-AMS model of MSM photodetector;
- Implemented the model into hAMster provided by AnSoft;
- Validated the model by comparing simulation results with experimental data.

6.3 Raman Amplifier

- Developed a behavioral VHDL-AMS model of Raman Amplifier;
- Implemented the model into hAMster from AnSoft;
- Validated the model by comparing simulation results with experimental data.

6.4 Erbium Doped Fiber Amplifier (EDFA)

- Developed a behavioral VHDL-AMS model of EDFA;
- Implemented the model into hAMster from AnSoft;
- Validated the model by comparing with the experimental data.

A detailed description of the derived compact models, with references, and representative VHDL-AMS simulation results are presented in Appendix A at the end of this report.

7 DESIGN AND FABRICATION OF TEST STRUCTURES AND VALIDATION FOR RF INTERCONNECTS AND OPTO-ELECTRONIC SYSTEMS

In this task, University of Delaware and Cornell University groups designed, fabricated, and measured test O/E and mixed-signal VLSI structures to validate models and extract necessary physical parameters.

7.1 Design, Fabrication, and Testing of OE and RF chips and PCBs

This task was primarily performed by **University of Delaware (UD)**, led by Dr. Fouad Kiamilev. UD has been focusing on providing experimental circuits and measured data for the verification and validation of CFDRS new modeling and simulation capabilities in the OE-IDEAS project.

First year accomplishments:

- Completed the design, fabrication and testing of a testing chip using TSMC 0.25um CMOS technology. The chip contains arrays of VCSEL drivers, optic receivers, LVDS drivers and receivers.
- Transferred the design database to Micromesh for subsequent processing.

Second year accomplishments:

- Generated Mayo 10G system MCM design database in DXF format for CFD to transfer the database to Micromesh and to simulate the MCM electrical interconnects performance.
- Performed experimental study of the signal integrity performance of the electrical traces on DARPA RATS main board.
- Performed the theoretical and simulation studies of Via-Stub resonance phenomenon on system PCBs.
- Designed and implemented low power Current Mode Logic electrical interconnects in Peregrine 0.5um Silicon on Sapphire process. Testing is in process.

Graphics:

OE-IDEAS Test Chip (1st-year accomplishment):

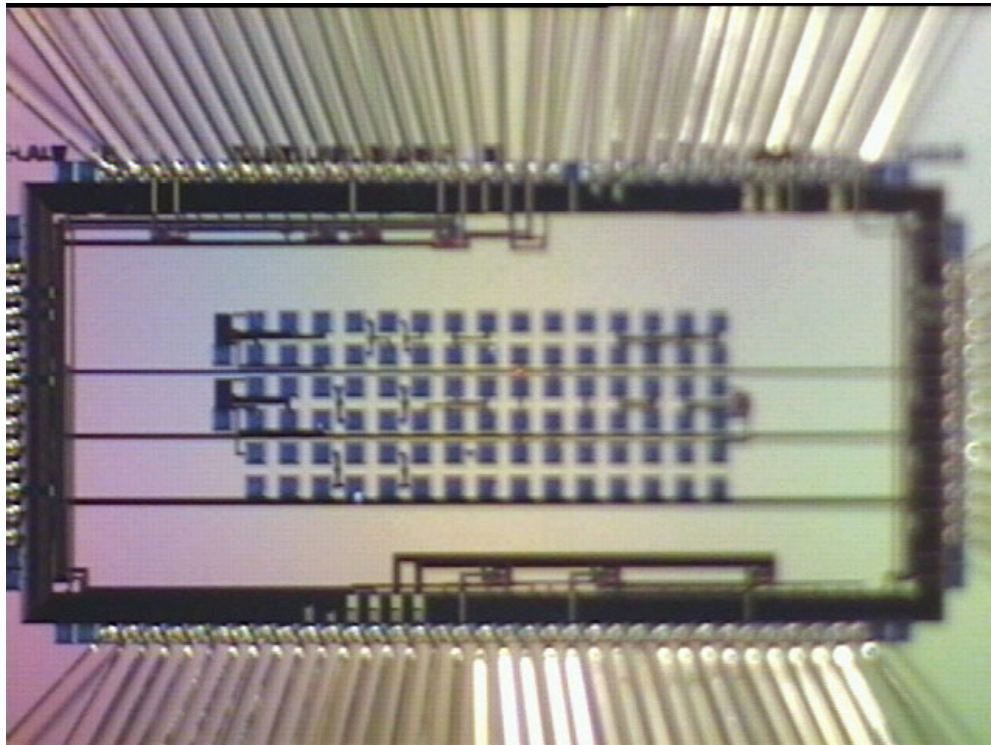
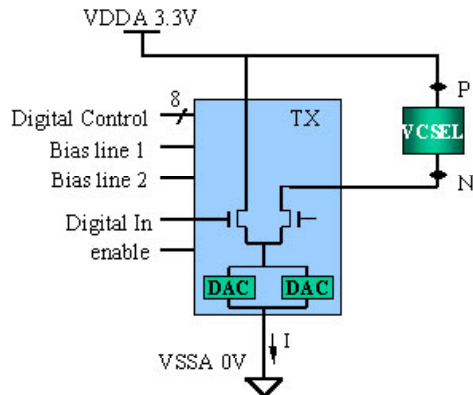
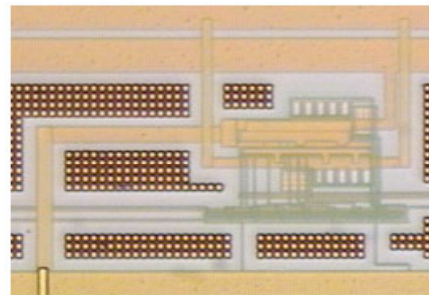
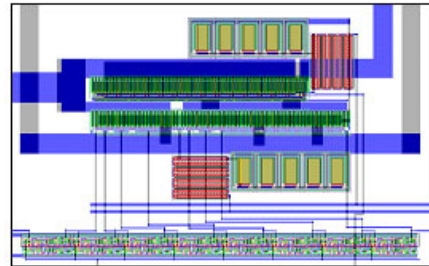


Figure 66. Chip with Bonding Wires.

LVDS Driver-Receiver Testing:



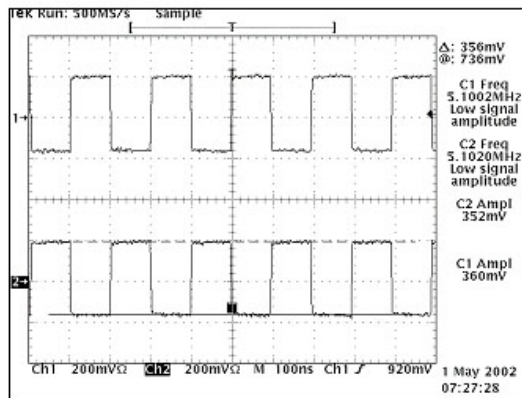
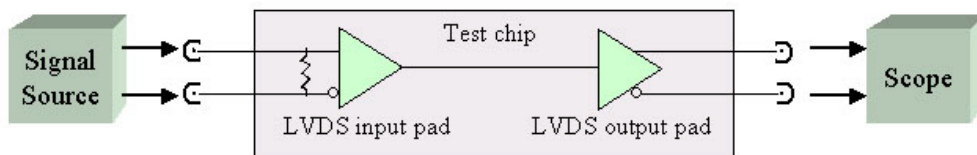
Layout and photograph



Features:

- Independent and digitally controlled bias current and modulation current settings
- Power down capability
- Current steering for reduced SSN

LVDS Driver-Receiver Testing:

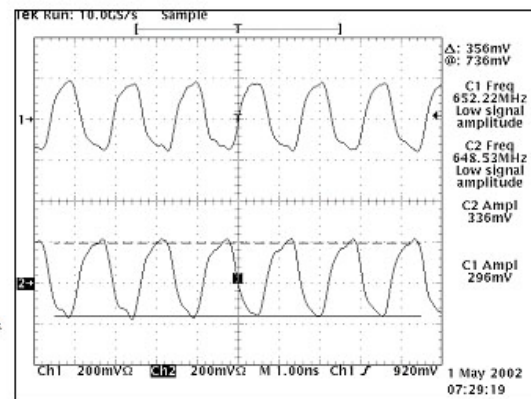


5MHz, 360mV p-p output from 400mV p-p source

Low Speed

High Speed

650MHz, 330mV p-p output from 400mV p-p source



Mayo 10G Opto-Electronic System Multi-Chip Module (MCM)
(2nd-year accomplishment):

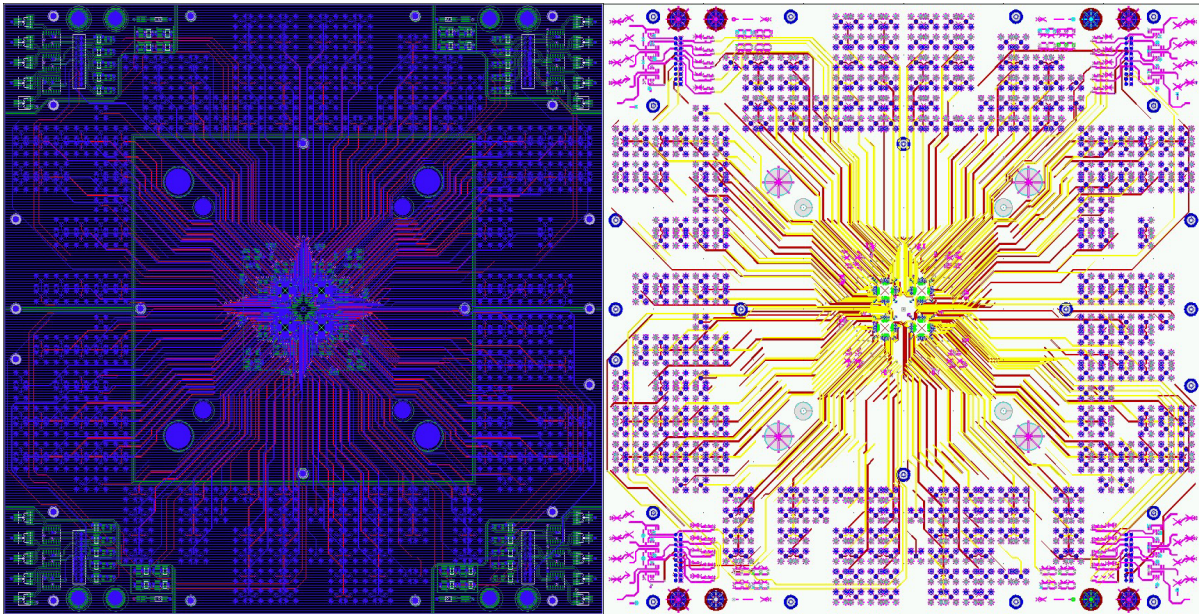
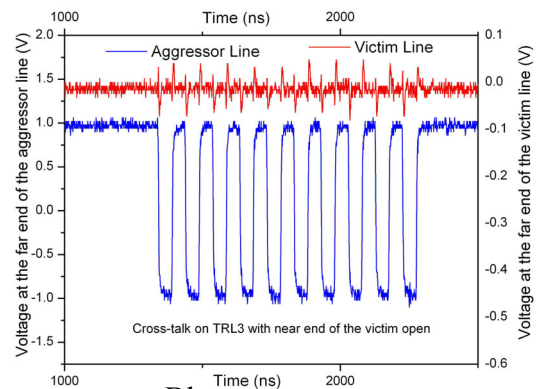
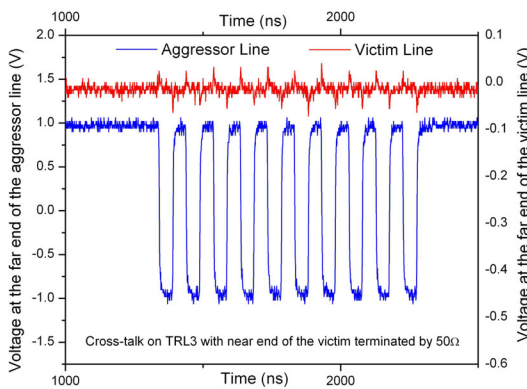
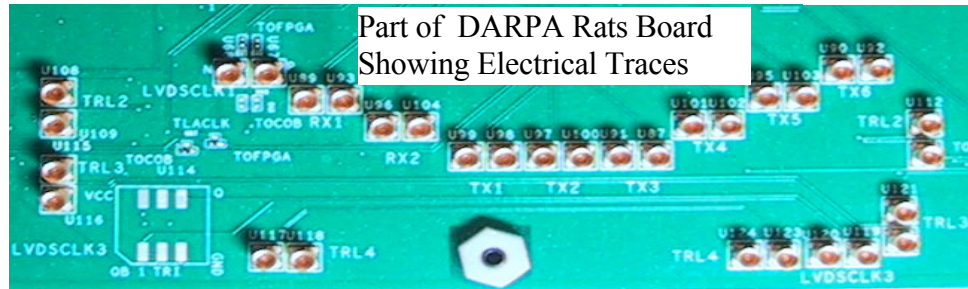
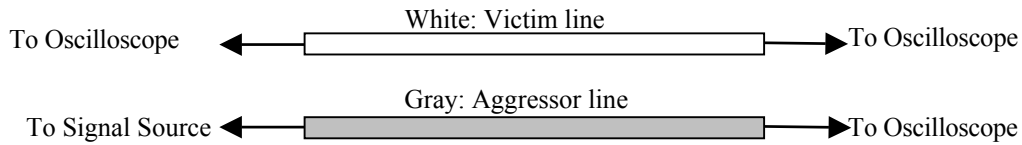


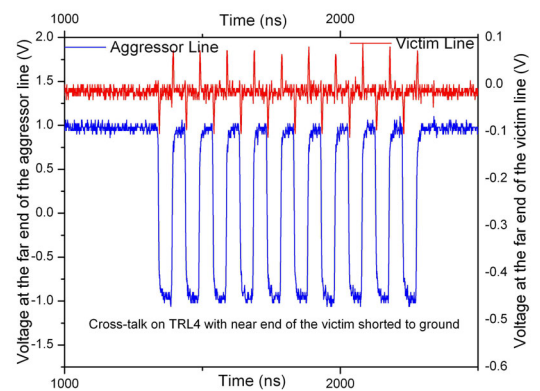
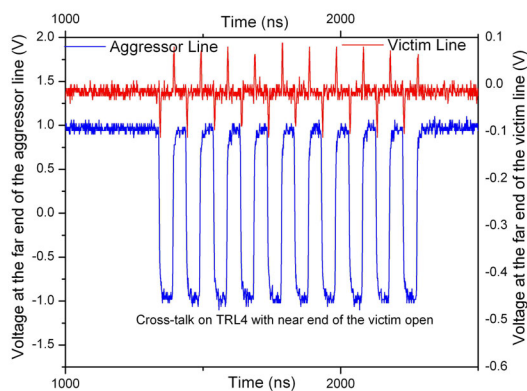
Figure 67. Mayo 10G system MCM layout, in Cadence-Allegro (left) and CFD-Micromesh (right).

- Measurement of Signal Integrity Properties on DARPA RATS Board Electrical Traces
(2nd-year accomplishment)

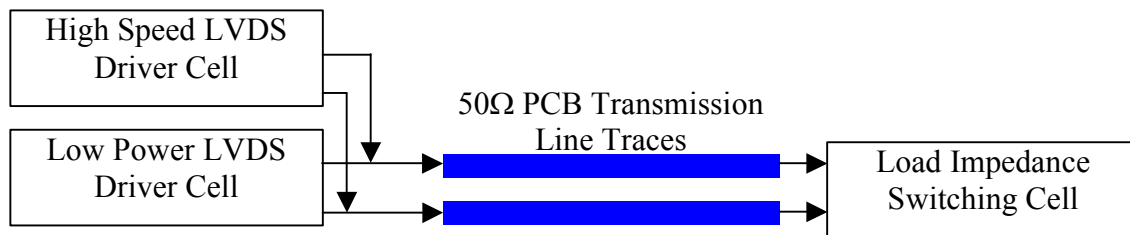


Cross Talk Measurements

Blue: aggressor
Red: victim



- *Dual-Rate Current Mode Logic Electrical Interconnects (2nd-year accomplishment)*



Dual Rate CML
Electrical
Interconnects were
implemented in
Peregrine 0.5um
SOI process;
Testing is on-going

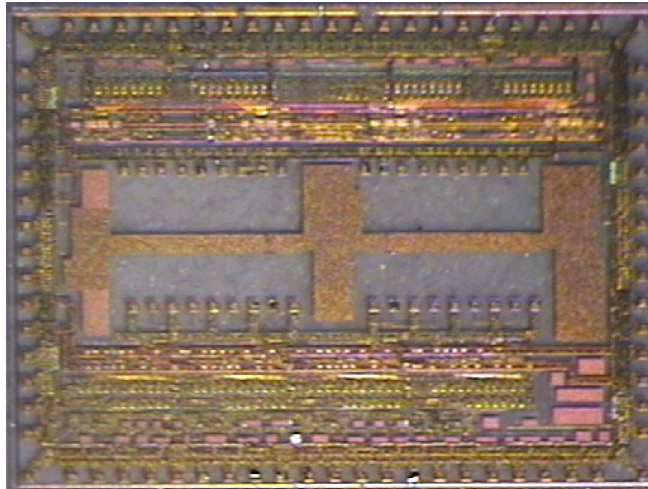
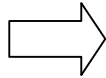


Figure 68. Dual-Rate Current Mode Logic Electrical Interconnects test chip.

7.2 Characterization and modeling of on-chip interconnect with realistic loads and drives

Full 3D Maxwell's solver cannot be directly applied to the complex interconnect problem in mixed-technology IC due to its huge complexity. Any computational algorithm for interconnect analysis has to be linear or $O(n)$, where n is the number of interconnect lines in the system. The constraint mainly comes from the increase in n also following the growth in Moore's Law, and hence we cannot otherwise anticipate future computing machines to handle the complexity. Algorithms of $O(n)$ almost dictates that the analysis will be based on lumped or spectrum analysis. At **Cornell University**, the S-parameters approach with generalization to large signals has been attempted for interconnect coupling. Interconnect structures have been fabricated in Cornell Nanofab with the initial measurements presented in the figures below.

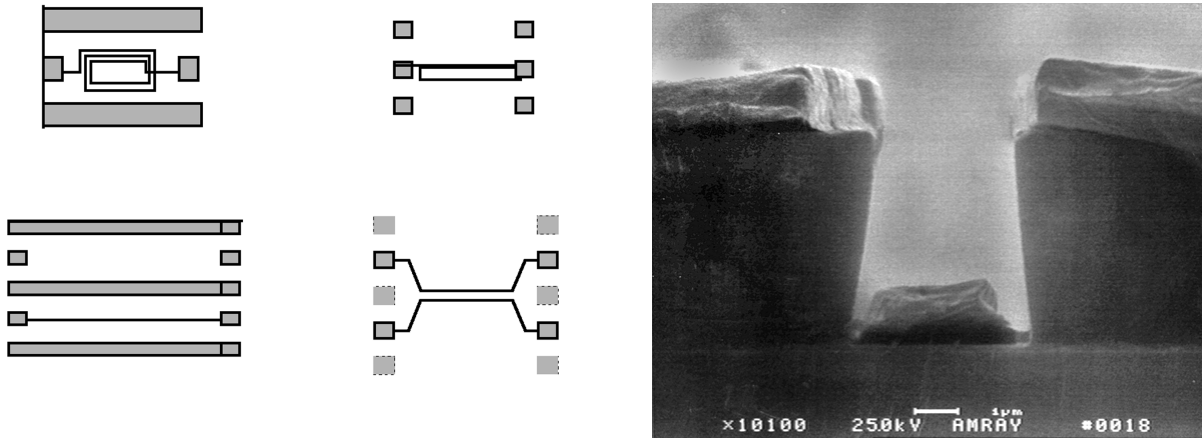


Figure 69. Interconnect structures fabricated in Cornell Nanofab.

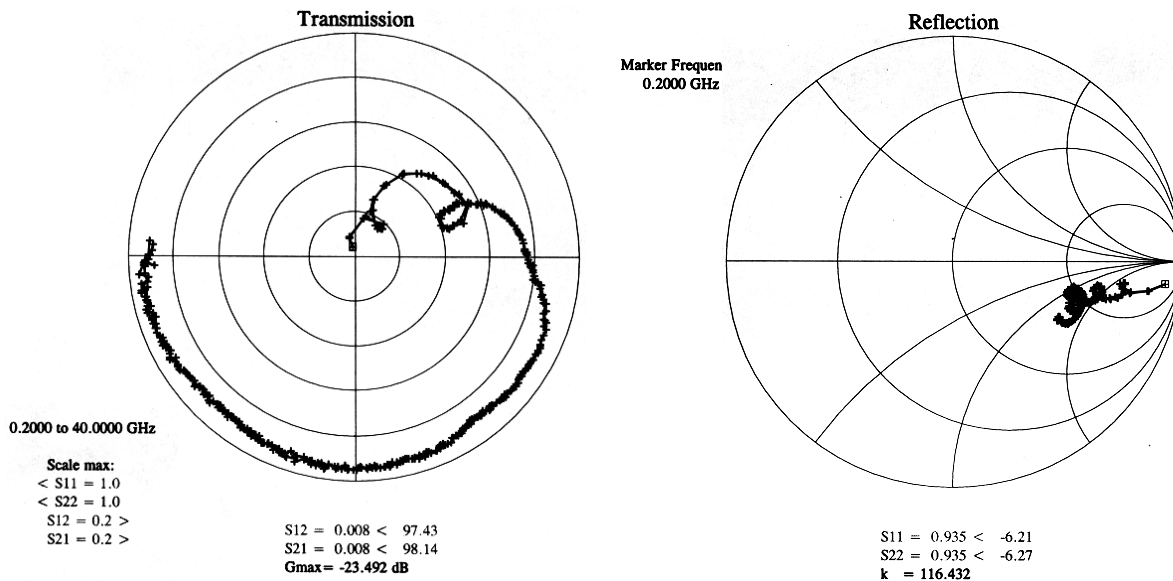


Figure 70. Results of initial measurements of the interconnect structures fabricated at Cornell University.

Transient Analysis of Nonlinear Microwave Circuits Using Small-Signal S-Parameters

The number of carrier frequencies limits the application of Harmonic-Balance (HB) method, which has matured as the workhorse for nonlinear microwave circuit analyses. A newly proposed frequency-domain method in allows more accurate description of the frequency dependence than that of the Root model. It can also be applied to strongly nonlinear circuit analysis, where the conventional frequency-domain methods, such as power series and Volterra-series analysis, are not appropriate. However, the total number of frequencies that can be considered is still limited.

Microwave circuits intended for telecommunication applications are expected to handle one or more carriers modulated with non-null information signals, i.e., finite bandwidth excitations. The bandwidth issue is more pronounced in CDMA and the emerging ultra-wide-band (UWB) communication systems. Furthermore, waveform engineering for the linearization of power amplifiers in CDMA systems, waveform analysis of high-efficiency power amplifiers (such as class F) and UWB systems require accurate transient analysis and simulation methods for nonlinear microwave circuits, which was considered not necessary a decade ago. The broadband nature of those problems makes the available methods difficult to use.

Here we propose a general method for nonlinear circuit transient analysis based on measured small-signal scattering parameters. The method does not suffer from the limitations of the aforementioned approaches. The procedure directly constructs the large signal response from the small-signal scattering parameters. The method is applied to the simulation of a high electron mobility transistor (HEMT) power amplifier. Reasonable agreement between the simulated and measured results is obtained. This method does not have limitations on the number of input carrier frequencies or the total number of frequencies. It is expected to be a useful and efficient tool in waveform engineering applications.

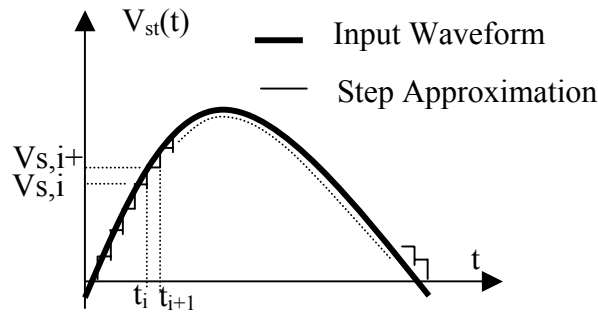


Figure 71. Approximation of input waveform.

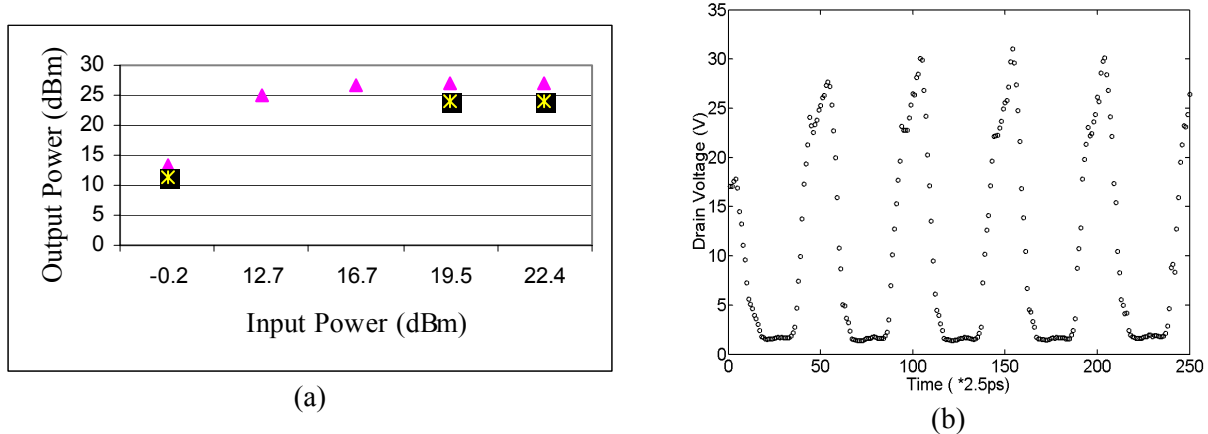


Figure 72. Measured and simulated results. (a) Output power. The square is the simulated points, and the triangles are measured points; (b) Simulated output voltage waveforms.

For more details on this topic, see the attached paper from Cornell University “Transient Analysis of Nonlinear Microwave Circuits Using Small-Signal Scattering Parameters”, by Pingshan Wang, Valeriy S. Kaper, Shealy J. Richard, and Edwin C. Kan, submitted to *IEEE MTT-S Conference*, June 2003.

Interconnect modeling of mixed-signal integrated circuits

A small signal s-parameter transient analysis method for high-speed interconnect with CMOS inverters as transceivers is developed. The input signal is approximated as the summation of small amplitude step functions. The linear-microwave-circuit theory is used in the simulation algorithm with the measured scattering parameters of the nonlinear active devices and the dispersive interconnect lines. Thus, no frequency dependent information is lost. The self-consistent method may also be used to analyze the small signal crosstalk simultaneously. Simulation results agree well with experimental results.

A typical interconnect representation is shown in Figure 73. The interconnect line is generally a linear system (except the nonlinear transmission line interconnect proposed previously in this NeoCAD project as soliton interconnect), despite some operating voltage level related phenomena. Its frequency dependent characteristics are faithfully and conveniently described using small-signal s-parameters, S_L , shown in Figure 73. The driver and receiver are nonlinear devices. Their small signal s-parameters depend on the bias conditions. As a result, their s-parameters across the full bias space, S_D and S_R , will be used in the following simulation and analysis.

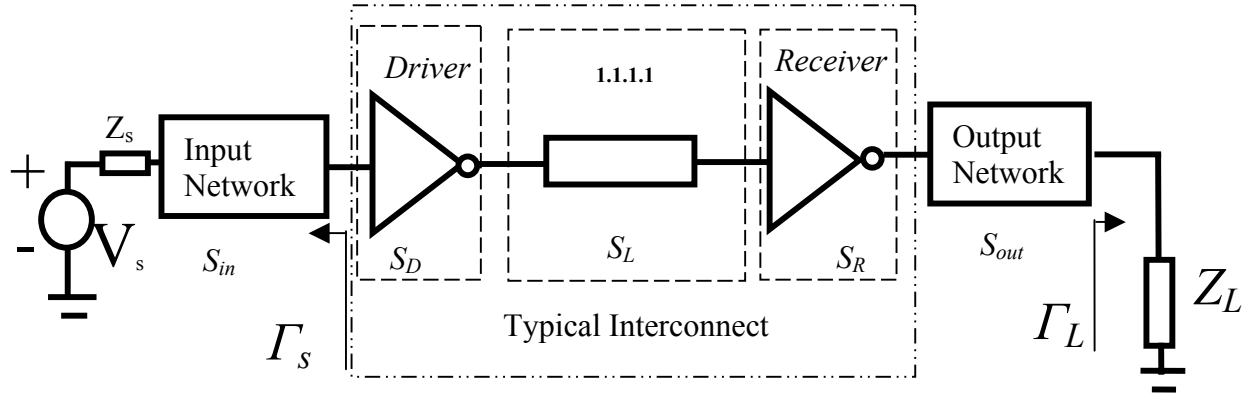


Figure 73. An interconnect circuit with an input power source, an input network with s-parameter S_{in} , and an output network with S_{out} . Z_s is the source impedance. The input and output networks provide connections between the power source and the load. Γ_s and Γ_L denote the source and load reflection coefficient in the frequency domain.

A transient analysis needs to find the circuit response to an arbitrary input signal, shown in Figure 74. We approximate the input signal as the summation of small amplitude step-functions, each with a different time delay, shown in Figure 74.

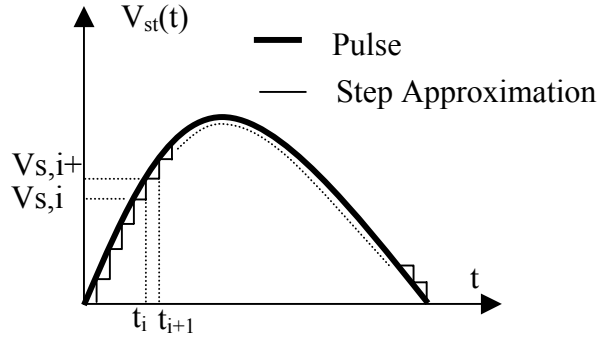


Figure 74. Approximation of input waveform.

The i_{th} step function is

$$V_s(t) = \sum_{i=1}^n (V_{s,i+1} - V_{s,i})u(t - t_i), \quad (1)$$

where n is the number of discrete steps. The Fourier transform of the i_{th} step-function is,

$$V_{s,i}(\omega) = (V_{s,i+1} - V_{s,i})(\pi\delta(\omega) + \frac{1}{j\omega})\exp(-j\omega t_i) \quad (2)$$

The response of the circuit to the i_{th} small step input pulse can be found using the microwave circuit theory through the signal flow graph in Figure 75 provided that S_D and S_R are specified using the algorithm in Figure 76.

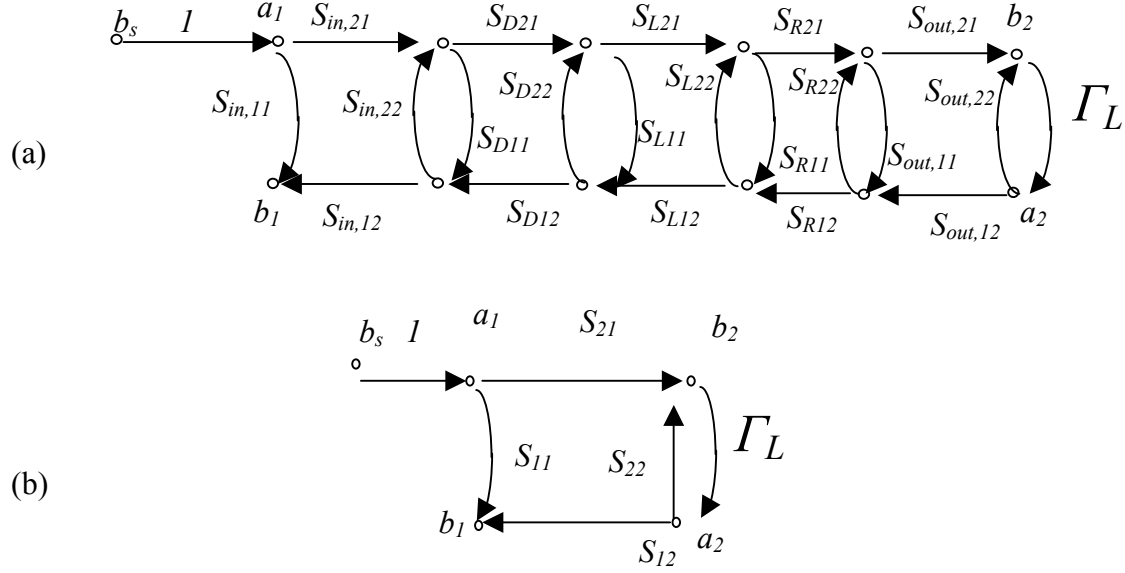


Figure 75. (a) A signal flow graph of the circuit in Fig. 1. A Z_0 (reference impedance of the s-parameters) is splitted from the source impedance, Z_s , in Fig.1. The rest of the sources impedance is combined with the input network, and represented by S_{in} . The separation is not necessary, but convenient for analysis formula simplifications. (b) Simplified signal flow graph by cascading the s-parameters of all the elements in (a).

In Figure 75, we have

$$b_s = \frac{V_{s,i}}{2\sqrt{Z_0}} \quad (3)$$

$$\Gamma_L = \frac{Z_L - Z_0}{Z_L + Z_0} \quad (4)$$

Therefore, we have

$$\begin{aligned} a_1 &= b_s \\ a_2 &= b_s \frac{\Gamma_L S_{21}}{1 - \Gamma_L S_{22}} \\ b_1 &= b_s \frac{S_{11} - \Gamma_L \Delta S}{1 - \Gamma_L S_{22}} \\ b_2 &= b_s \frac{S_{21}}{1 - \Gamma_L S_{22}} \\ \Delta S &= S_{11} S_{22} - S_{12} S_{21} \end{aligned} \quad (5)$$

With the incident and reflected waves given in equation (5), the voltages and currents at any port in circuit Figure 73 can be obtained easily with the help of the scattering parameters of the relevant sub-network. An inverse Fourier transformation gives the voltages and currents at the interested time moment.

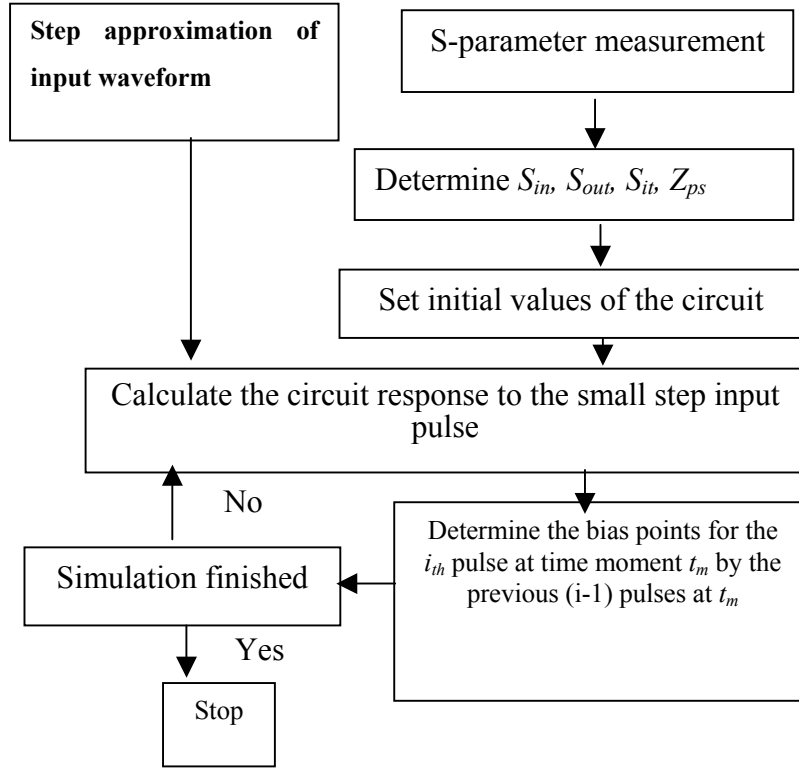


Figure 76. A flow chart of the frequency-domain algorithm

A new bias point for the next small step input calculation at the following time moment is then obtained by the summation of the circuit responses to all the previous small step inputs at the interested time moment. Using the algorithm in Figure 76, the transient response of the circuit can then be obtained.

The arbitrary input signal in Figure 74 can also be approximated as the summation of narrow square functions as,

$$V_s(t) = \sum_{i=1}^n V_{s,i}(u(t - t_{i+1}) - u(t - t_i)) \quad (6)$$

where n is the number of discrete steps. The Fourier transform of the i_{th} square signal is,

$$V_{s,i}(\omega) = V_{s,i} \frac{1}{j\omega} (-\exp(-j\omega t_{i+1}) + \exp(-j\omega t_i)) \quad (7)$$

The system response to this square signal depends on the bias conditions of the nonlinear devices determined by their responses to all the previous square signals at the moment when this signal appears. If the time step (the width of the square), $t_{i+1} - t_i$, is not large, the amplitude of each frequency component in (7) is small. The circuit operation condition will not change much as well. Therefore, the system is an instantaneous linear system to this square pulse though pulse amplitude seems large. Similar equations and algorithm can be used for the transient analysis.

In the concluding phase of the interconnect modeling, we solidified our programs for large-signal reconstruction from S-parameter measurements. Benchmarks of typical data paths containing nonlinear amplification elements are compared with full Maxwell solver, reduced solver, and SPICE-level large-signal simulation. Also, we have consolidated our effort in using permalloy and undergrid decoration of transmission lines (TL) and coplanar waveguides (CPW) to achieve broadband interconnect with small dispersion in MHz-20GHz ranges. This technology not only makes the design of complex interconnect network more tractable from decreased cross talk and more manageable large-signal behavior, but also gives the available interconnect simulation algorithm better handles to reduce the complexity. If no localization assumption can be applied through either the filament or partial inductance concept, the complex geometry of full-chip interconnect (more than 10^9 geometry objects) usually renders the modeling work intractable. This is one problem that we cannot hope to be solved by better computing capabilities, because to our present knowledge better computers can only be made from more complex interconnect network, and the simulation has to be linearly scaled.

Permalloy Loaded Transmission Line for High-speed Interconnect Applications

Self inductance and mutual inductance of global interconnect in deep sub-micrometer CMOS technologies are crucial factors of integrated circuits performance. Self inductance depends on the current return path, which is unknown prior to extracting and simulating the entire nonlinear circuits. A large number of the neighboring interconnects need to be considered for accurate estimation of the mutual inductance. Consequently, extraction of inductance is the present bottleneck in high-speed interconnect modeling and design.

The partial inductance method is the general practice for such problems, evaluating inductance for each wire segment by an imaginary loop with infinity. Furthermore, building a complete inductance matrix for all interconnects on an integrated circuit (IC) is impractical because this procedure will result in a large, tightly coupled network representation. Unlike capacitance matrices that can be truncated to represent only localized couplings, simply discarding remote mutual inductances can produce an unstable equivalent circuit mode. Based on this increased complexity and what is known from full-chip capacitance extraction, any attempt at full-chip inductance extraction requires some form of localization via windowing, which is hardly applicable to long wires. Techniques used in capacitance extraction, such as library construction and analytical formulas, cannot be directly applied to inductance extraction. Several other methods, such as return-limit loop inductance, the $2\times$ mutual inductance screening rule, and the susceptance matrix, have been proposed. These methods have their own specific limitations related to the penetrating nature of magnetic field coupling. Therefore, the ultimate solution to the interconnect inductance extraction and modeling is to eliminate the mutual magnetic field coupling and the dependence on the current return path for the self inductance. This can result in a diagonalized inductance matrix with elements accurately determined by the partial inductance method. We show that the incorporation of patterned permalloy in interconnects provides such a path. Introduction of high frequency magnetic material increases the self inductance. Nonetheless, it is demonstrated that inductance can have positive effects on the performance of VLSI, which suggests that increasing inductance in a controllable way can be beneficial for overall system considerations.

The figure below shows the test structures fabricated using a CMOS compatible process. Lines with or without patterned permalloy are designed for direct comparison on self and mutual inductance. Lines with patterned permalloy bars are $2\mu\text{m}$ wide, $7\mu\text{m}$ long and around 200nm thick. A patterned Tantalum (Ta) film of $\sim 20\text{ nm}$ thickness serves as an adhesion and migration-barrier layer. The distance between two adjacent permalloy bars is $2\mu\text{m}$. Aluminum transmission lines are $5\mu\text{m}$ wide. The coupling section of the two lines that are parallel to each other is $3,705\mu\text{m}$ long. The separation between the parallel transmission lines is $10\mu\text{m}$. These dimensions are all layout dimensions subject to lithography variations, except for the thickness. Identical comparison structures without patterned permalloy were also fabricated. The ground aluminum plate is $\sim 8\mu\text{m}$ below the top metals separated by SiO_2 deposited at $\sim 460\text{nm/minute}$ using plasma-enhanced chemical vapor deposition (PECVD). The porosity in PECVD oxide is high enough to relax the residual stress that no serious wafer warping is observed.

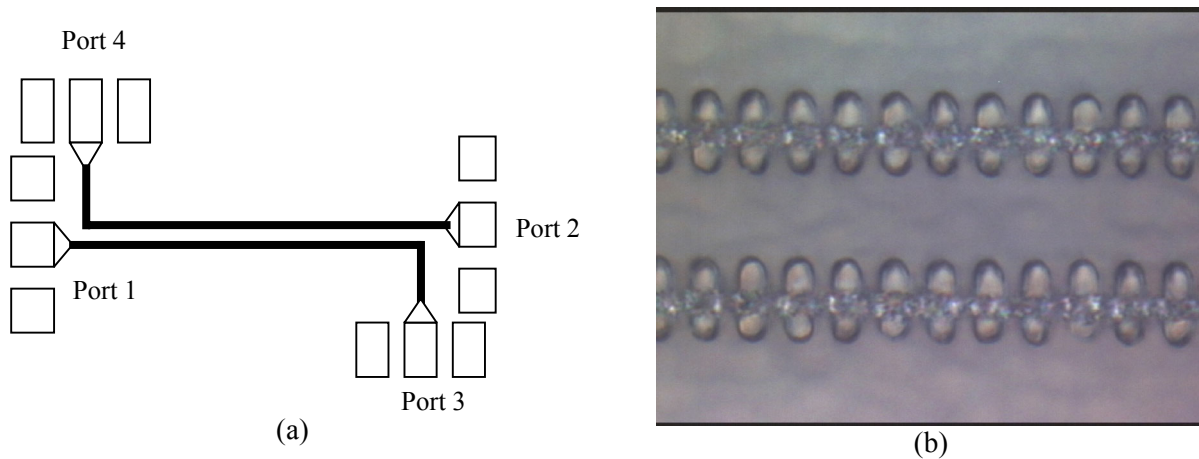


Figure 77. (a) Schematic of the magnetic coupling test structures; (b) part of the fabricated test structures

The comparison structures are designed to have a strong magnetic coupling, but small capacitive coupling. The estimated coupling capacitance and mutual inductance for the comparison structure are 18.9fF and 367pH , respectively. The structures with permalloy have slightly larger coupling capacitance and essentially the same mutual inductance.

After performing measuring pad de-embedding and equivalent circuit elements extraction procedures, the figure below shows the measured S_{12} while port 3 and 4 are left open. Asymptotically similar curves were obtained if port 3 and port 4 were connected to a 50 Ohm load through several sub-miniature adapter (SMA) elbow connectors. The measured S_{12} for the lines with patterned permalloy structures is essentially from the noise background. The comparison structure shows very small coupling at low frequencies. The coupling grows along with the increase of frequency as expected for the test structures. It is clear that patterned permalloy has effectively reduced the magnetic coupling for more than 60 dB , and the mutual inductance is virtually eliminated.

For more details on this topic, see the paper from Cornell University “Permalloy Loaded Transmission Line for High-speed Interconnect Applications”, by Pingshan Wang and Edwin Kan, submitted to *IEEE MTT-S Conference*, June 2003.

Patent application has been filed by the Cornell University group.

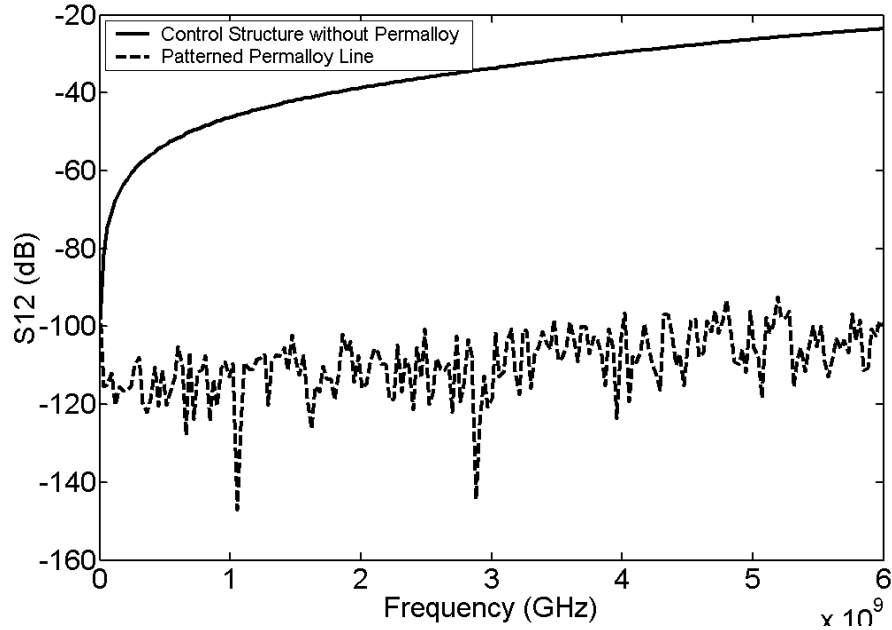


Figure 78. S_{12} of the coupled transmission lines.

8 NEOCAD TEST STRUCTURES AND BENCHMARKS SIMULATIONS

8.1 NeoCAD Benchmarks from the DaVinci Netbook website

In May 2002, CFDRRC downloaded all the materials from the DaVinci Netbook website containing the benchmark cases suggested for NeoCAD participants. We built 3D models and ran 3D EM simulations of several selected benchmark cases. This effort is reported below.

As a first test structure we took HRL-Mayo InP test chip “**ic_hrl_tc1**”, posted on the DaVinci web site. On that chip Mayo designed a variety of test structures, including coupled Line Pairs (LP), Coplanar lines (CP), and a Microstrip line (MS) structure (see Figure 79). The substrate was 700-micron thick semi-insulating InP. Two levels of gold interconnect were separated by a polyimide dielectric layer 1.4 microns thick. Metal-1 lies on the substrate and is 0.55 microns thick. Metal-2 is on top of the polyimide dielectric and is 2 microns thick.

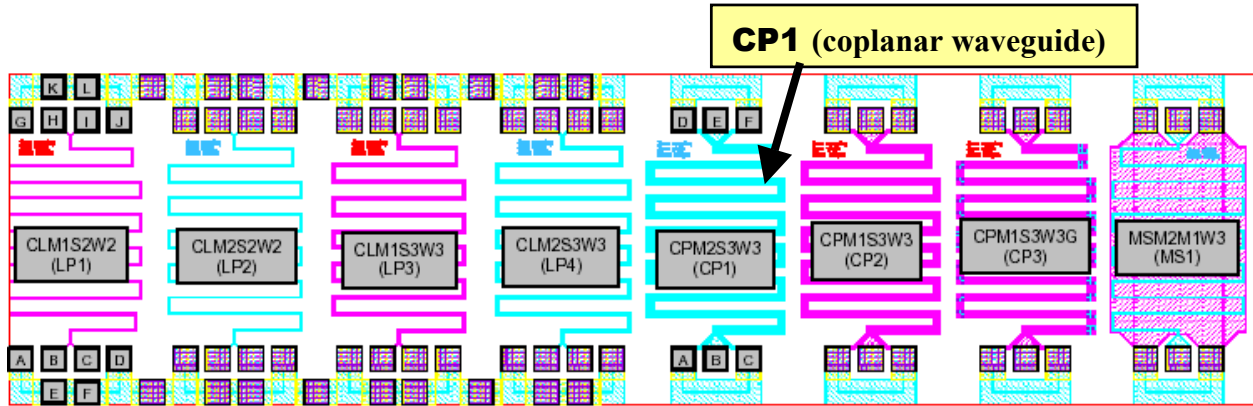


Figure 79. Layouts of several test structures on the Mayo test chip “ic_hrl_tc1”.

The *ic_hrl_tc1* GDSII layout file was imported into CFD-Micromesh and analyzed with respect of the most appropriate test structures for the initial simulations with NeoCAD tools at CFDRC. As the first test case, we selected the CP1 structure (Figure 79), that is Coplanar line of Metal 2, with Spacing 3 μ m and Width 3 μ m. The CP1 layout, imported in CFD-Micromesh, is shown in Figure 80, together with the computational mesh..

After setting up in CFD-Micromesh the technological data (thicknesses and positions of all the layers) of the *ic_hrl_tc1* chip, a 3-D computational model was generated automatically by CFD-Micromesh. An example of structured grid is shown in Figure 80 below.

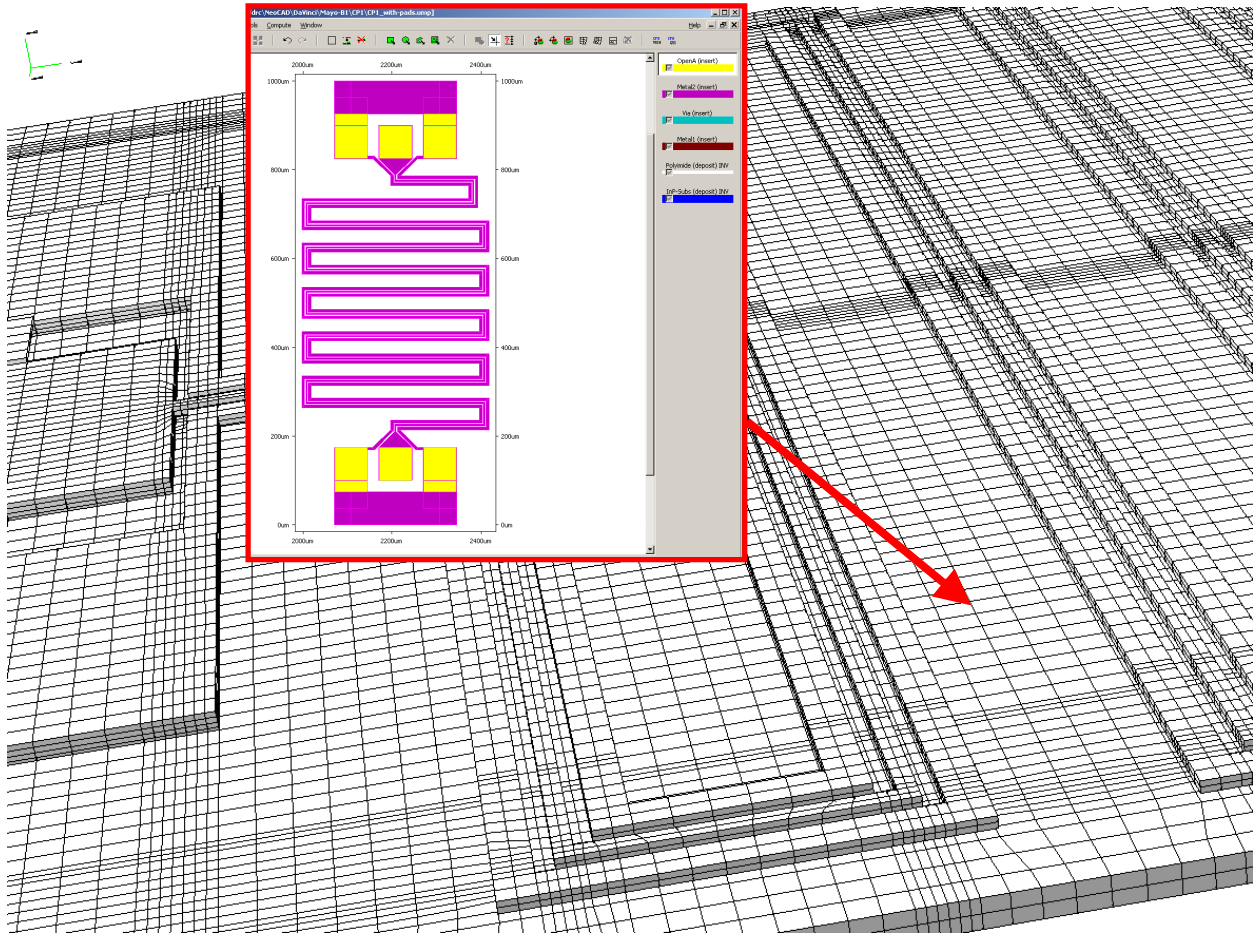


Figure 80. Layout of the CP1 structure, imported in CFD-Micromesh from GDSII file, and the computational grid generated automatically by CFD-Micromesh from the layout.

Next, we performed a series of static-electric and transient full-wave electromagnetic simulations with ACE+, to extract the basic parameters (resistance, I-V characteristics, S-parameters) of the structure, to be compared with the measured data posted on the DaVinci site, in the Mayo-B1 directory.

Before performing a full-wave transient electromagnetic simulation of the CP1 structure, a steady-state electric simulation of the line was performed, to calculate the resistances of all the lines. An example snapshot of these results is shown below (with 3.3 V applied to the ground pads A and C). Both the line resistance values agree very well with the values measure at Mayo – see the table below..

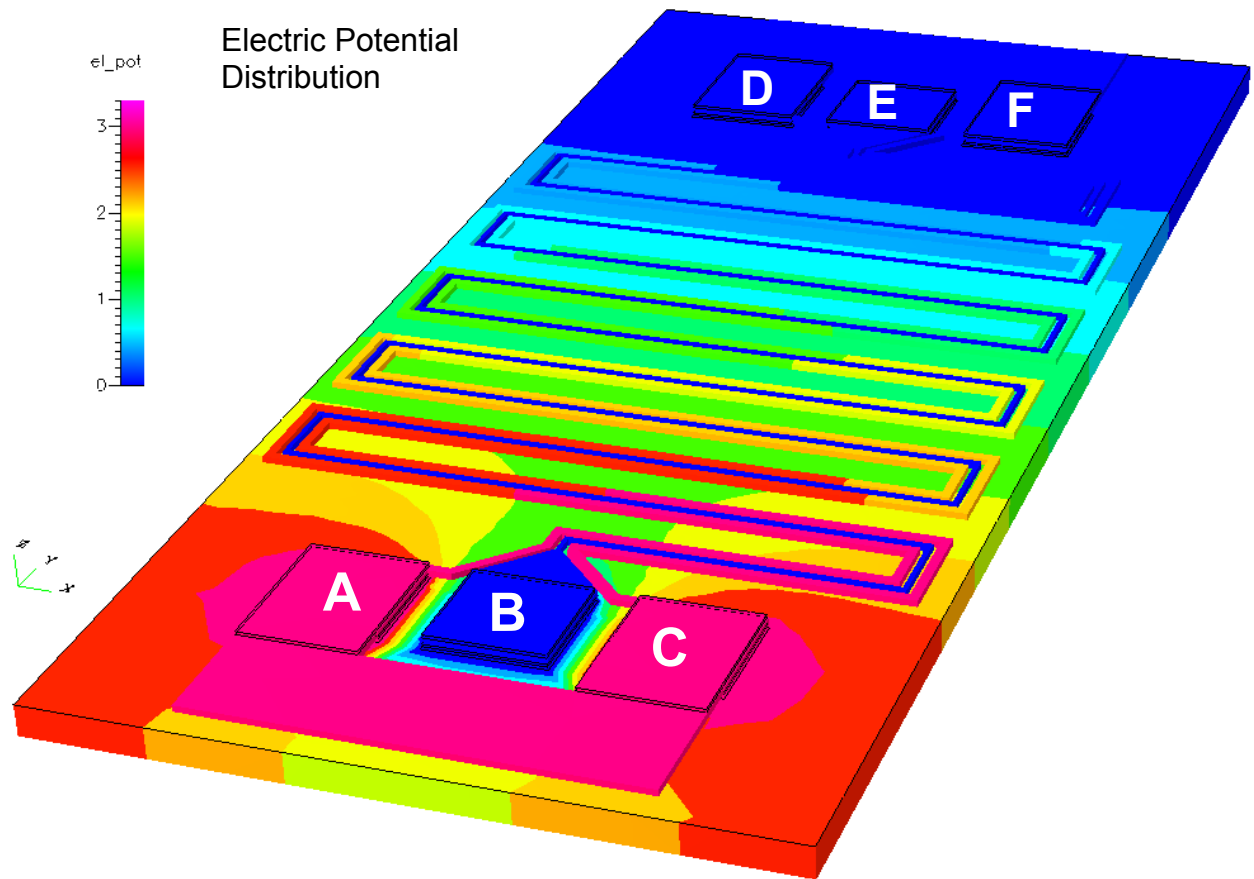


Figure 81. An example snapshot of steady-state electric simulation results of CFD-ACE+, with 3.3 V applied to the ground pads A and C, and zero volts to all the other pads.

Line Resistances:

	Calculated with CFD-ACE+	Measured at Mayo
B-E Line	19.76 Ω	19.86 Ω
A-D Line (ground)	5.12 Ω	5.15 Ω

Next, a full-wave transient electromagnetic simulation of a signal pulse propagation on the CP1 serpentine coplanar waveguide was performed using CFDRC's EMAG simulator. A Gaussian pulse with amplitude 3.3 V was applied between the input (pad B) and the ground pads (A and C). Several selected snapshots of that transient simulation are shown in the figures below, as well as resulting time-dependent voltage and current waveforms, and calculated from them S-parameters converted to frequency domain.

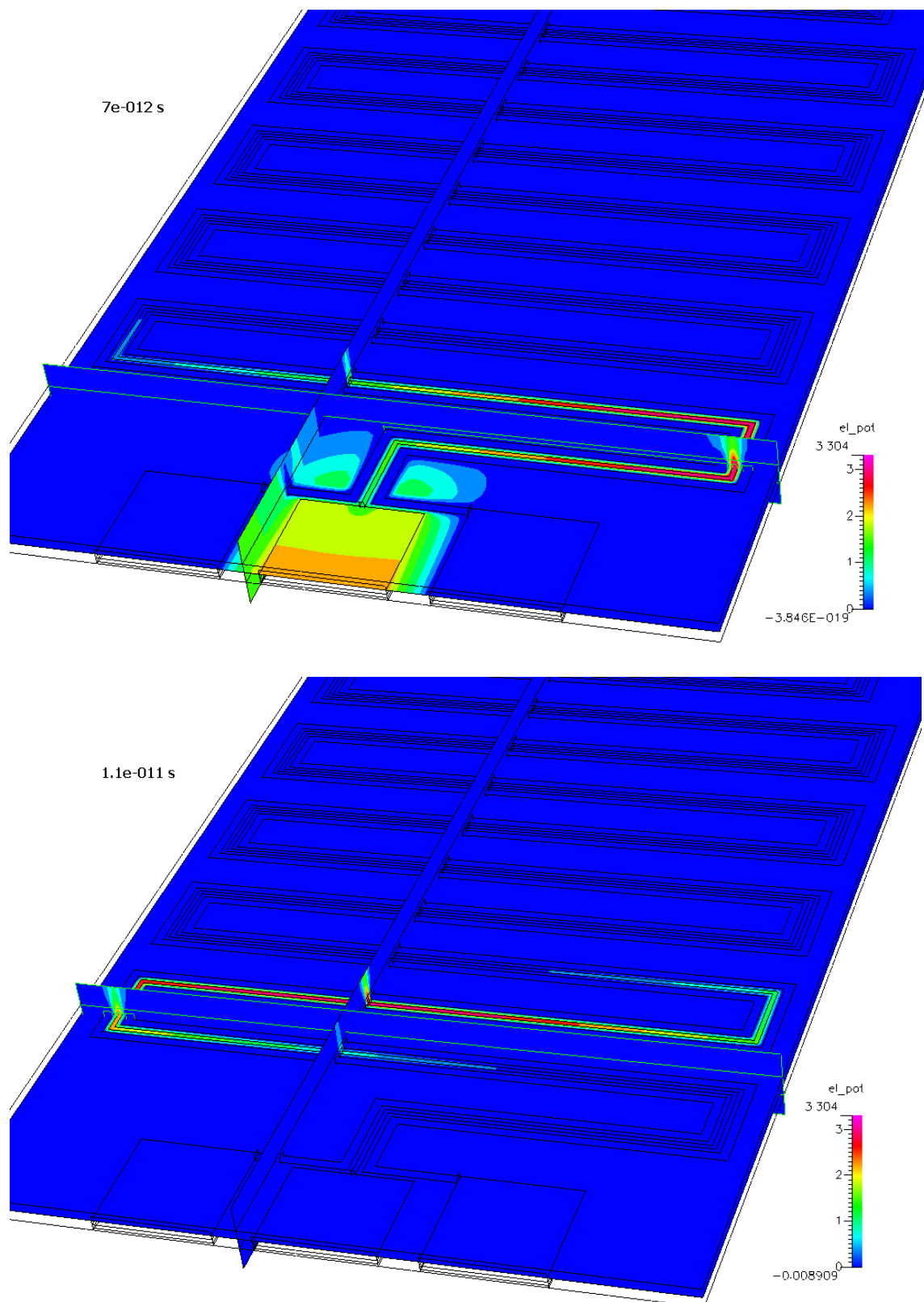


Figure 82. Simulated Gaussian Pulse Propagation in Time in the CP1 Benchmark Structure.

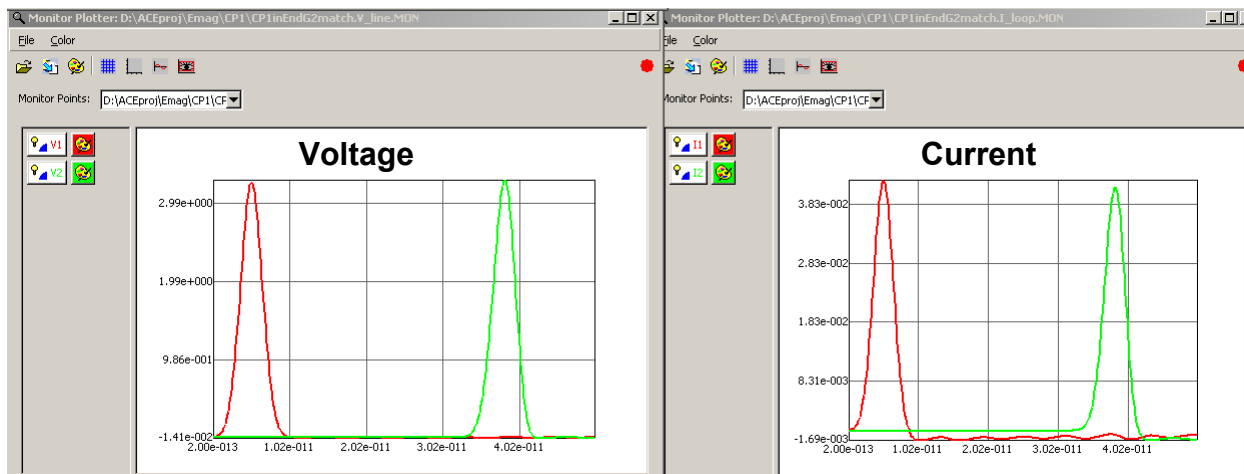


Figure 83. Voltage and Current Monitors at the CP1 line beginning (red) and end (green).

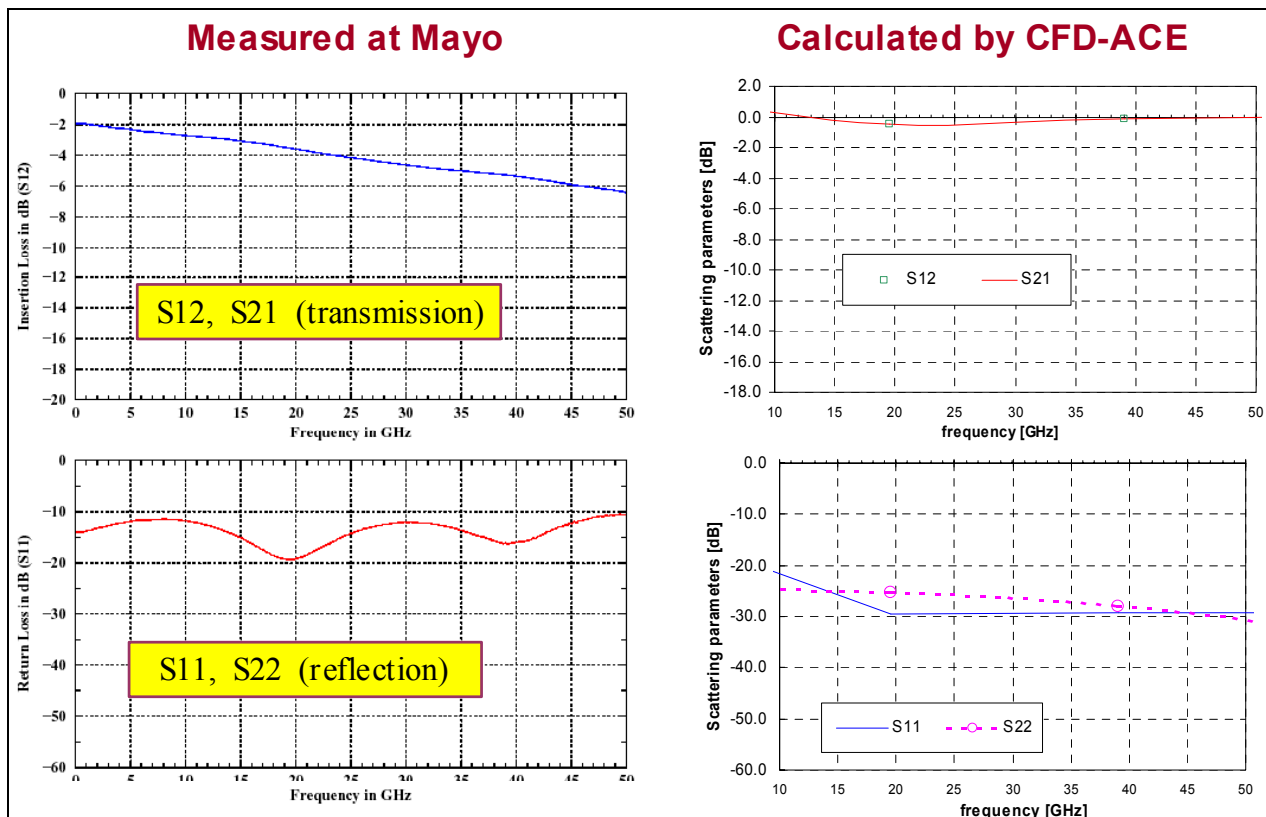


Figure 84. Measured and Calculated S-Parameters for the CP1 Test Structure.

2OG Waveguide Benchmark from NCSU

Another structure taken from the DaVinci web site for CFDRC software validation was the **2OG** structure from **NCSU-B2B** directory. The structure is illustrated in Figure 85 below.

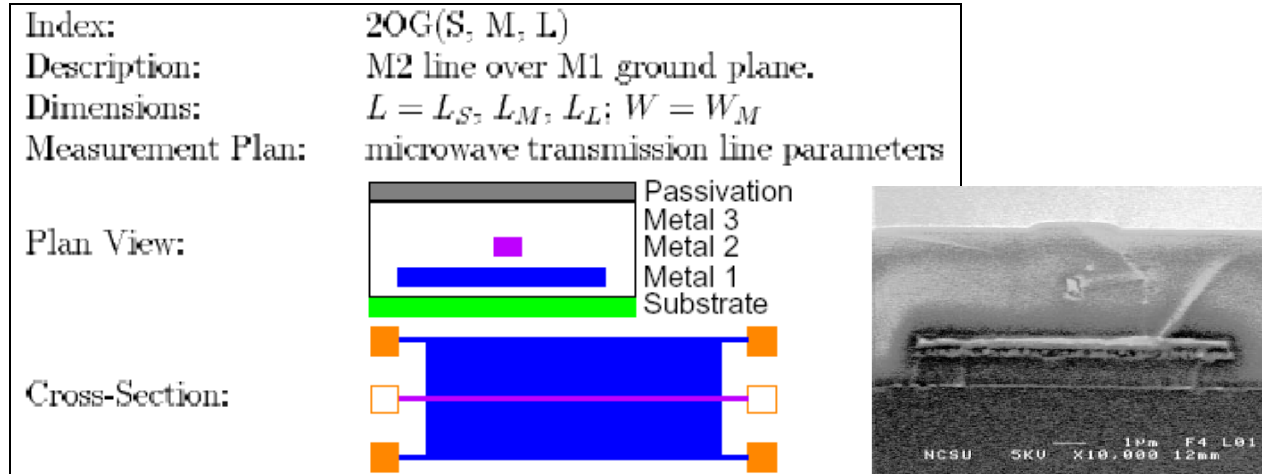


Figure 85. The 2OG test structure from NCSU-B2B: basic parameters and cross-section photo.

For our first calculation we selected the structure of the width $W_M = 0.5 \mu\text{m}$, and the “short” length $L_S = 400 \mu\text{m}$. A structured computational mesh built automatically in CFD-Micromesh is shown in Figure 86. Using this mesh, we performed full-wave electromagnetic simulations with CFD-Maxwell.

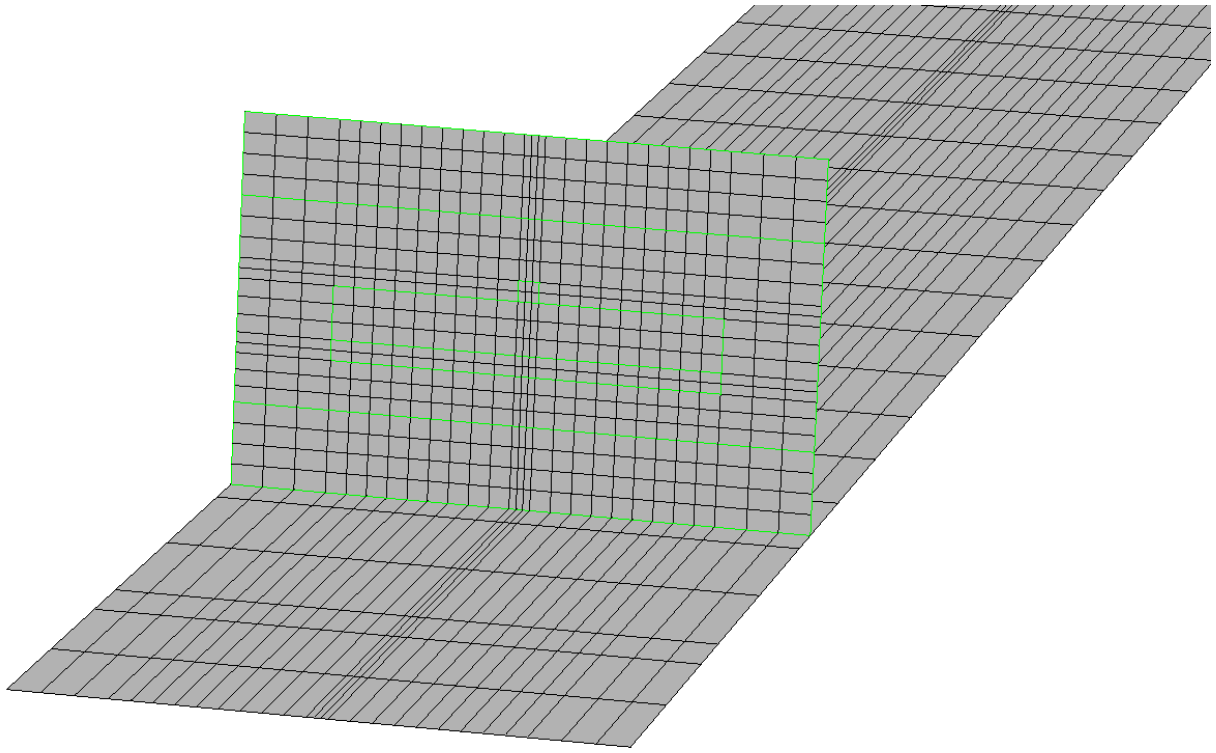


Figure 86. Computational mesh built in CFD-Micromesh for 2OG structure from NCSU.

The computed S-parameters are shown in Figure 87. For comparison, the S-parameters measured by NCSU are plotted in Figure 88. Some issues may be observed. First, note that the measured data cover much lower range of frequencies (45 MHz – 20 GHz), while the calculated range of frequencies is 9GHz – 200 GHz. This is due to the fact that our current CFD-Maxwell algorithms do not allow to calculate long simulated time intervals due to very small computation time step (limited by CFL number, or Courant factor). Therefore, the short simulated time intervals translate into very high frequency range after FFT transformation. This difficulty should be overcome after implementation of the ADI algorithm, reported earlier in this report.

Second, even if both in the measurements and calculations S_{11} is very close to S_{22} , and S_{12} is virtually equal to S_{21} , the values obtained from experiments and calculations are very different. In the measured data the reflection coefficients (S_{11} , S_{22}) are high (0.6...0.9), and the transmission coefficients (S_{12} , S_{21}) are much lower (0.2 to 0.3 for higher frequencies). In our calculated results it is the opposite: in the similar frequency range (up to 20 GHz, or $2E+10$) the reflection coefficients (S_{11} , S_{22}) are lower (less than 0.5), and the transmission coefficients (S_{12} , S_{21}) are much higher (more than 0.9). This discrepancy was discussed, also with the authors of the measurements from NCSU (Prof. M. Steer's group). The reflection and transmission depend very much on the line termination impedance (matching), and we were not sure if the experimental equipment (microprobes and pads) setup had not affected the measured characteristics (if the line impedance was not ideally matched on both ends, the reflection coefficients S_{11} and S_{22} would be much higher).

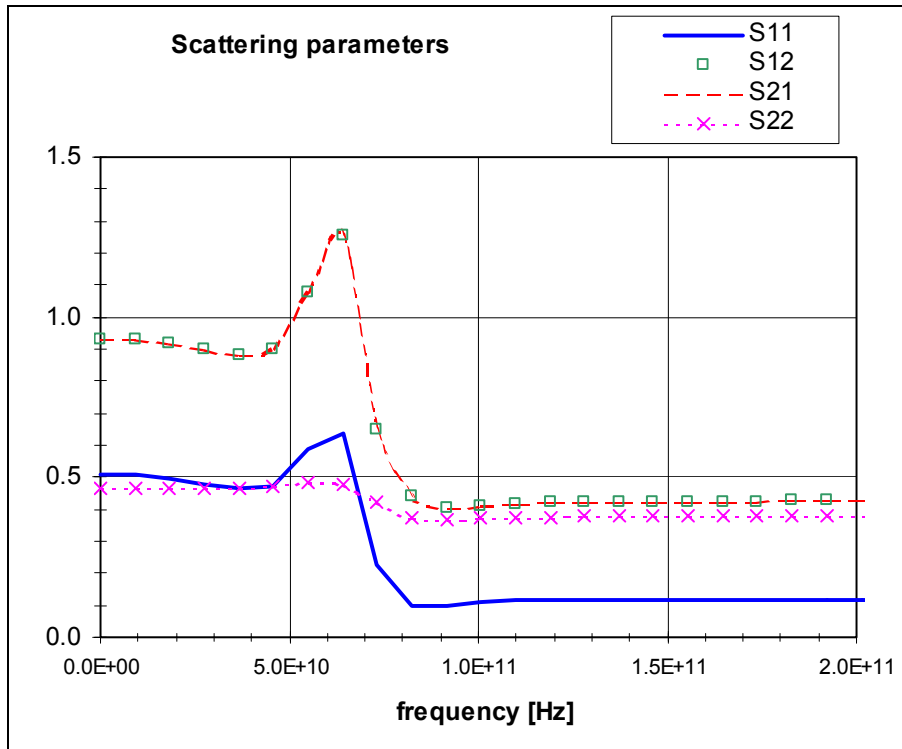


Figure 87. S-parameters computed by CFD-Maxwell for the 2OG structure.

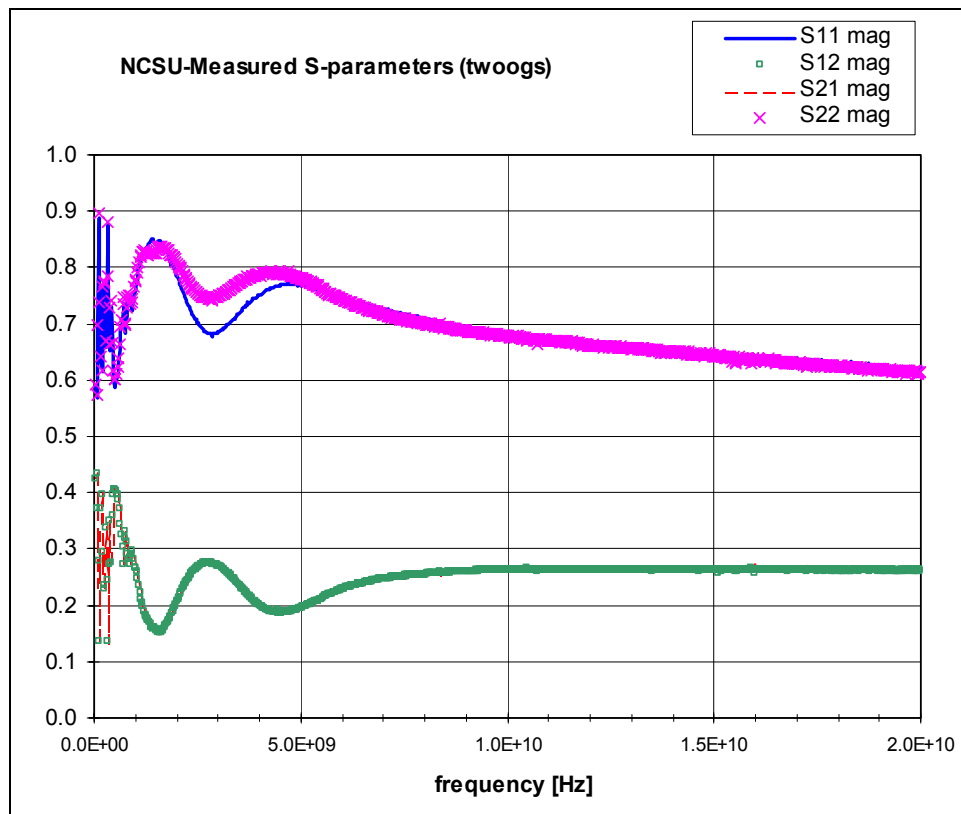
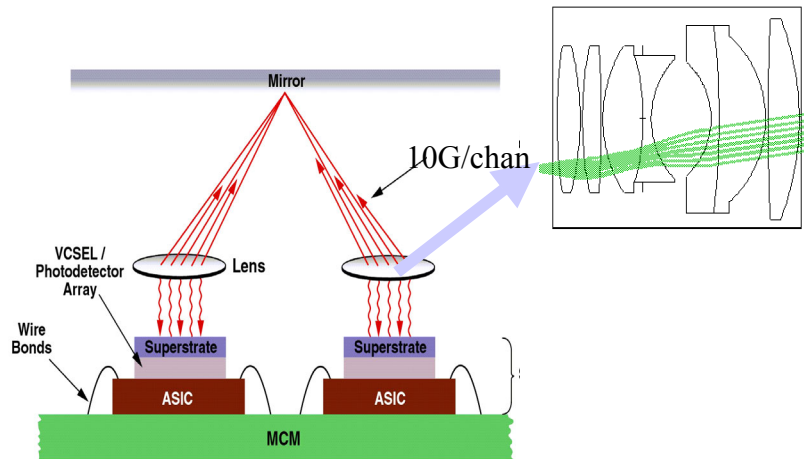


Figure 88. S-parameters of the 2OG structure, measured by NCSU.

8.2 Simulation of Critical Path from the Mayo “10G” System MCM Board

In the first year of NeoCAD, after extensive discussions with participation of CFDRC, U-Delaware, U-Pittsburgh, and Mayo, it was decided that the '10G' FSOI system funded under DARPA VLSI-Photonics Program would be used as a benchmark problem for the teams working on integrated electronic/photonic system design. A sketch of the 10G System is depicted in Figure 5.1.

According to the NeoCAD goal of using the 10G System as a demonstrator, we decided to use the MCM (multi-chip module) board of the 10G System as an example for our electromagnetic simulations. The most interesting would be analysis of a “critical path” on the MCM board, which may limit the overall performance. Such a critical path has been identified through consulting with Mayo, UPitt, and UDelaware. It is illustrated graphically in the following figures.



**Figure 89. Sketch of the “10G” FSOI System, accepted as the NeoCAD benchmark.
The MCM board is at the bottom.**

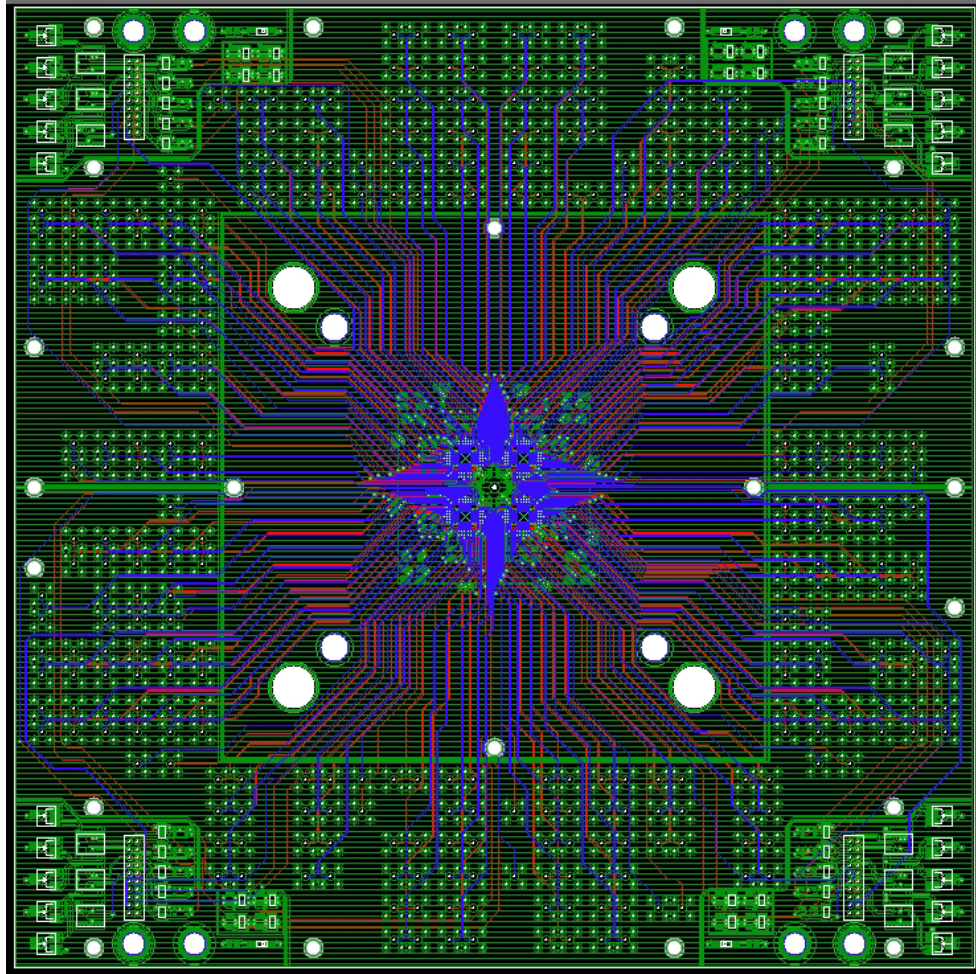


Figure 90. 10G MCM board layout (4 chips = 4 clusters of SPAs).

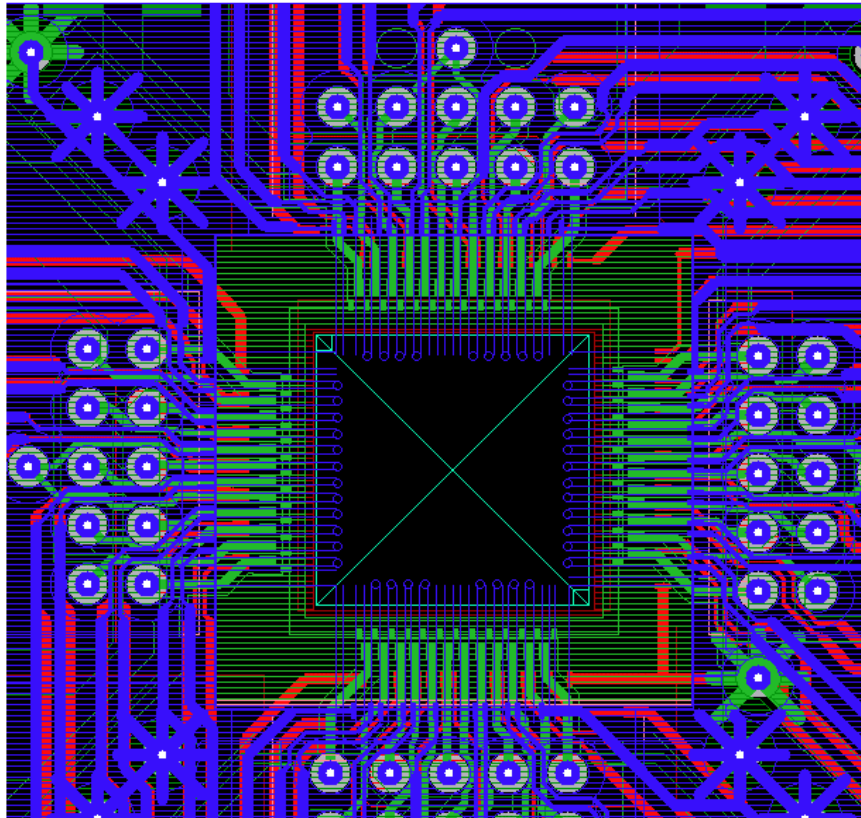
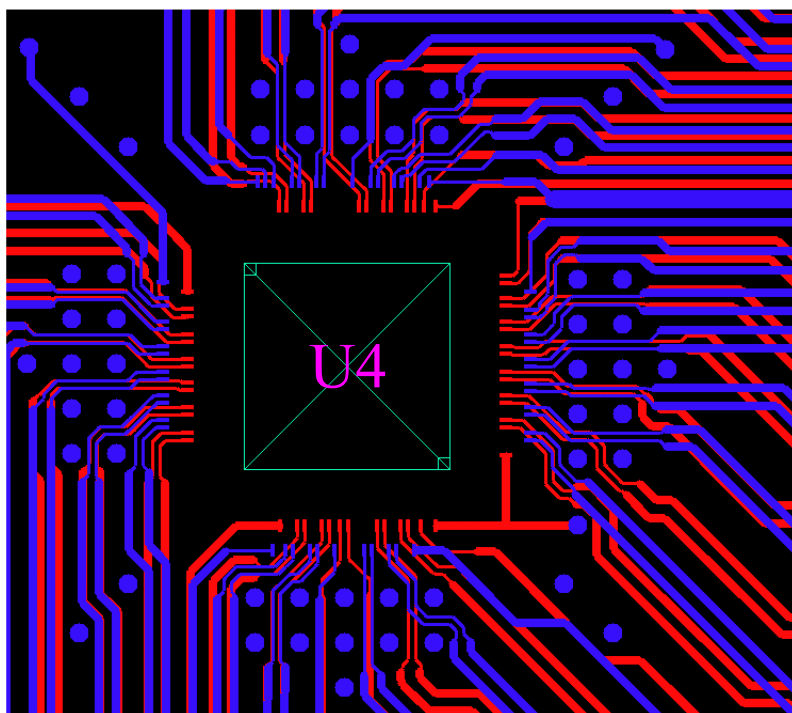


Figure 91. Single chip layout on the 10G MCM board.



Blue line : signal_1, Red line : signal_2

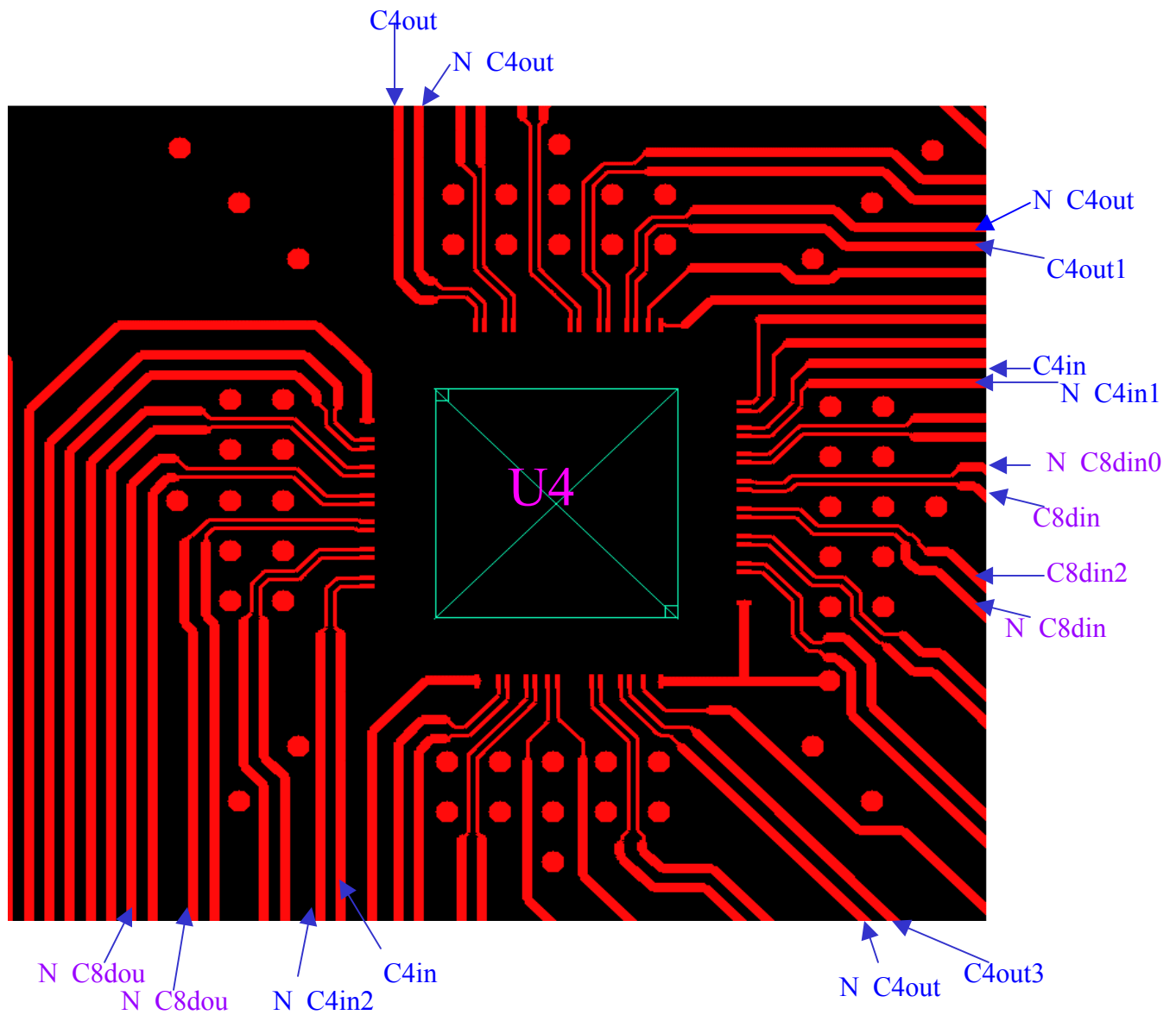
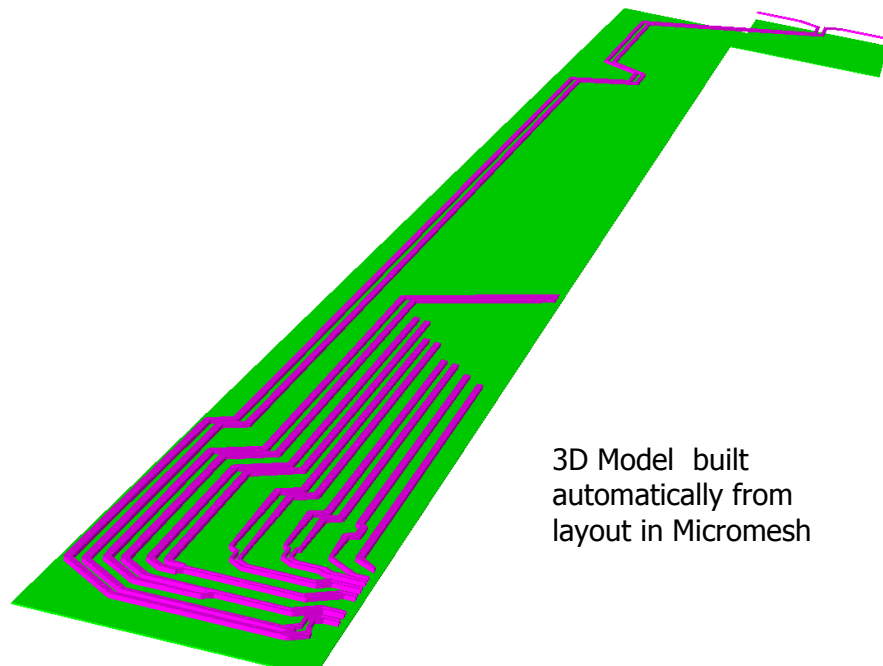
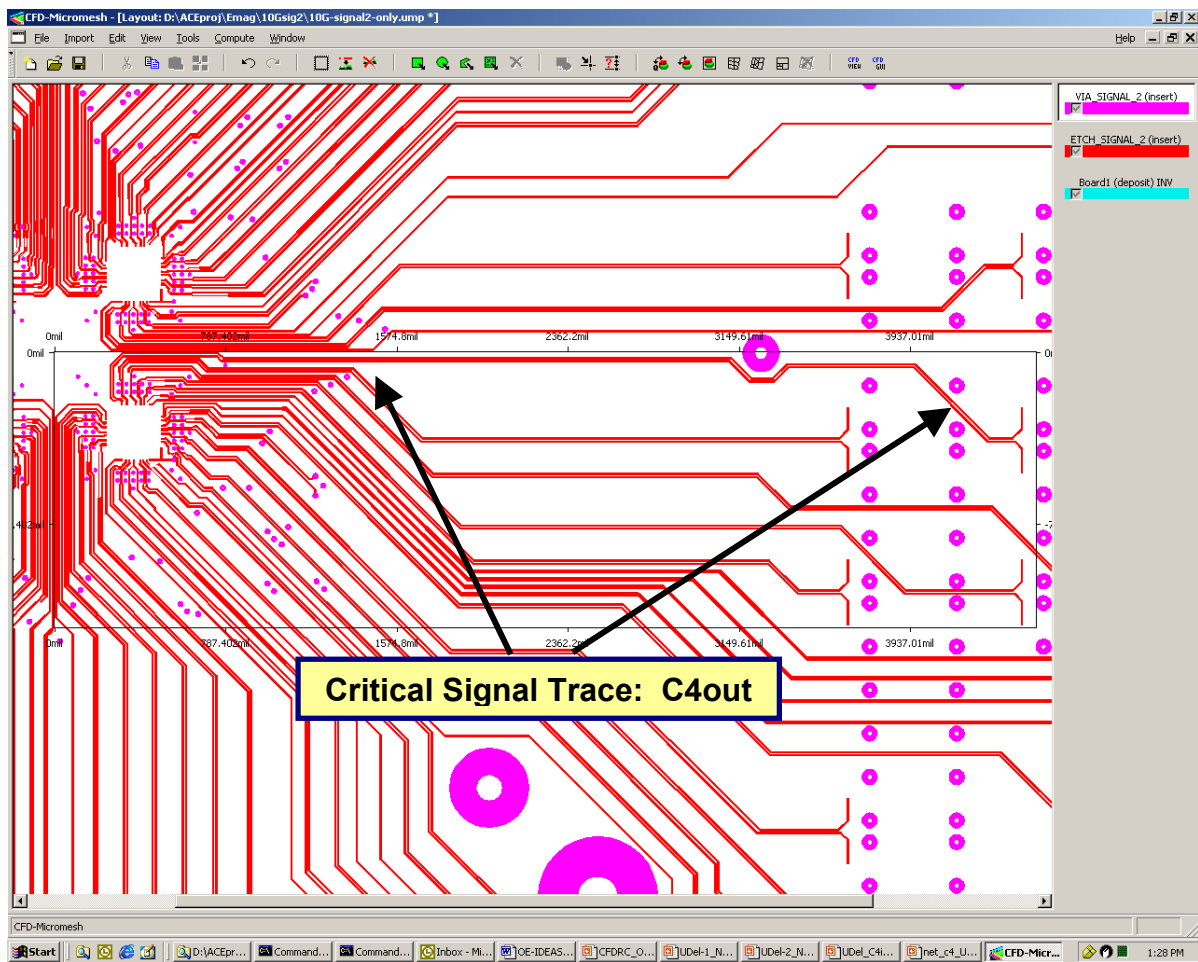


Figure 92. Some signal traces in the layer “signal_2 chip_U4”. The C4out signal path (two differential lines) has been selected as the “critical path” for first electromagnetic simulations.

The C4 “critical signal path” from the above layout of the 10G System MCM board was selected to be simulated by CFDRC’s full-wave electromagnetic simulator, to extract crucial electrical parameters (e.g. S-parameters, cross-talk, delays).

The layout of the full C4 Path, after importing into Micromesh, is shown in the figure below.



3D Model built
automatically from
layout in Micromesh

Figure 93. The C4out signal-path layout, and a 3D model built in Micromesh.

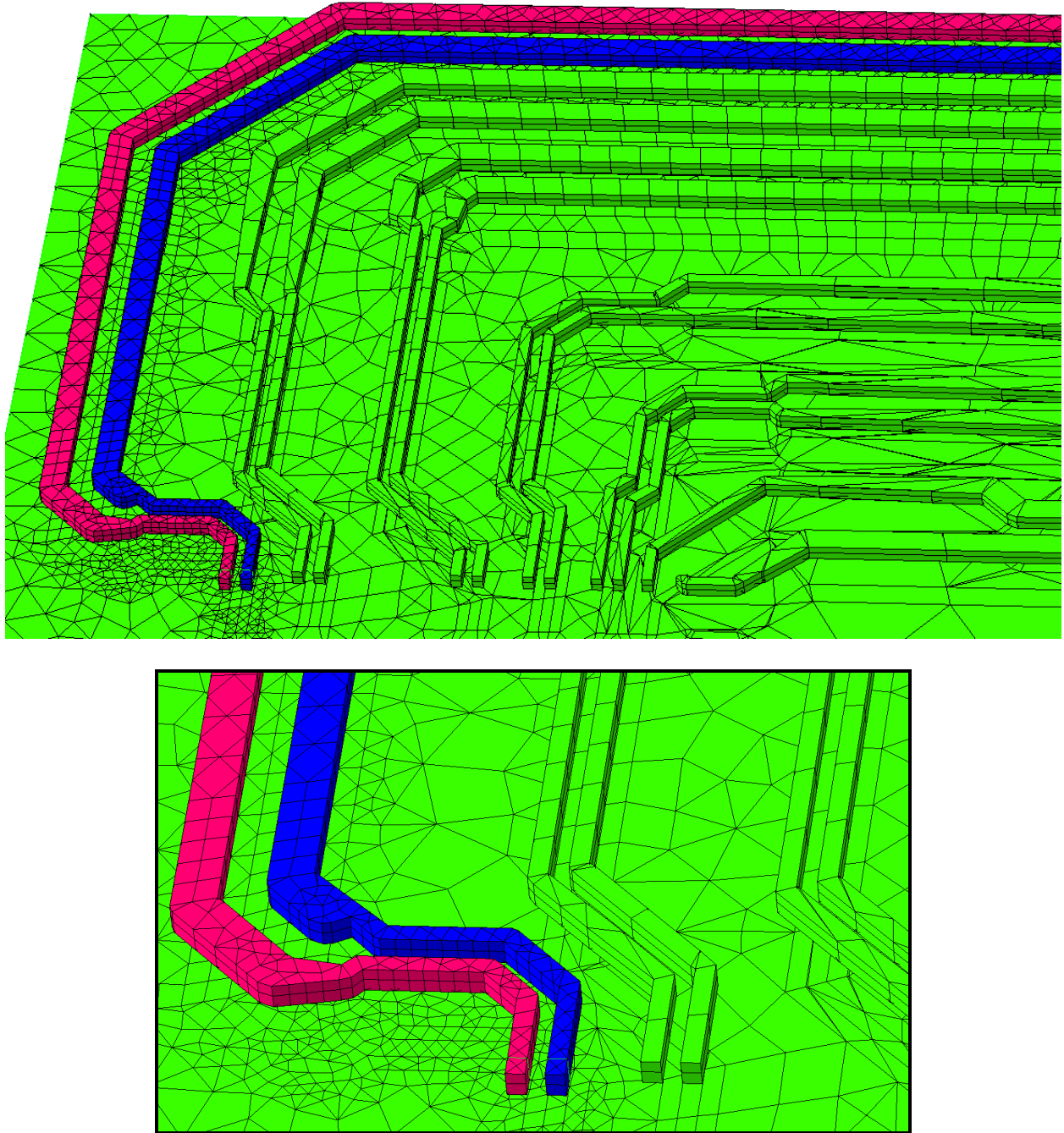


Figure 94. Mesh details of the C4out Line, with static differential electric potential results.

Before performing a full-wave transient electromagnetic simulation on the critical path C4out, a steady-state electric simulation of the line was performed, to calculate the line resistance. A snapshot of these results is shown below (with +3/-3 V applied to the differential lines C4out and N_C4out). Both the line resistance values calculated with ACE+ were less than 3% different from the values extracted by Cadence Allegro tool.

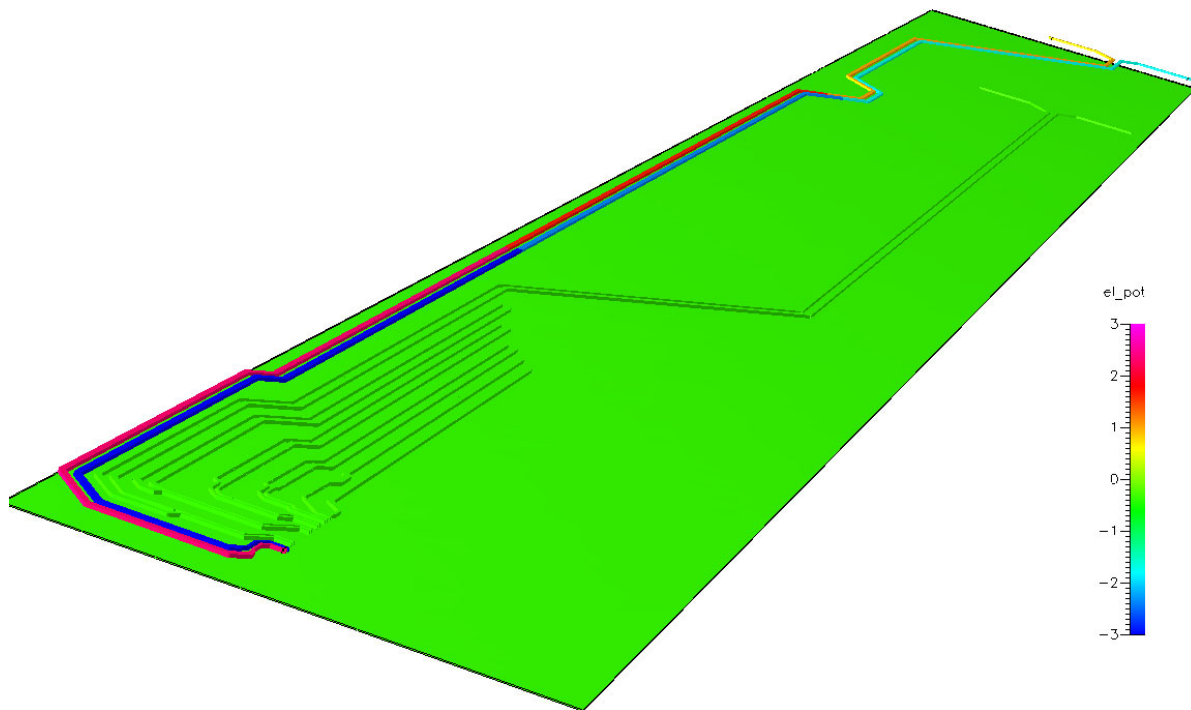
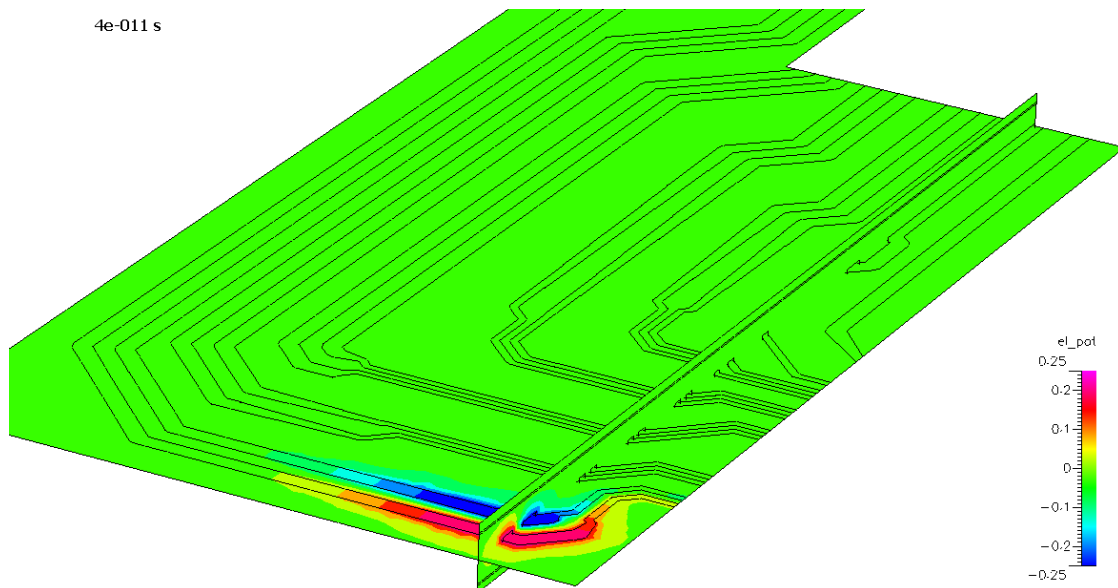
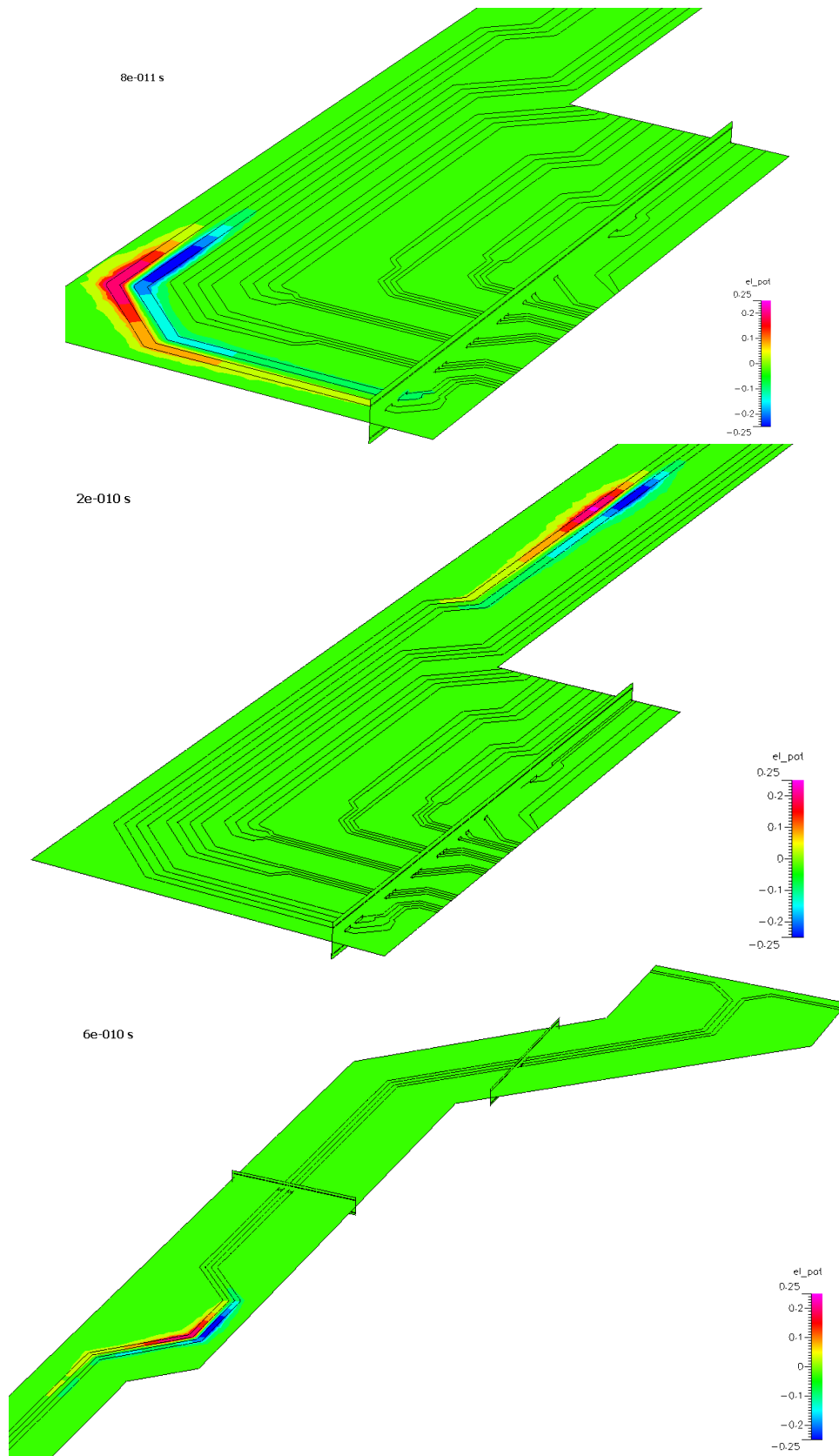


Figure 95. Snapshot of the steady-state electric simulation results from CFD-ACE+, with +3 V and -3 V applied to the differential lines C4out and N_C4out.

Next, a full-wave transient electromagnetic simulation of a signal pulse propagation on the critical path C4out was performed using the CFDRC's EMAG simulator. A differential signal (Gaussian pulse) of +0.4 and -0.4 volt was applied to the input of the differential lines C4out and N_C4out. Several selected snapshots of that transient simulation are shown in the figures below.





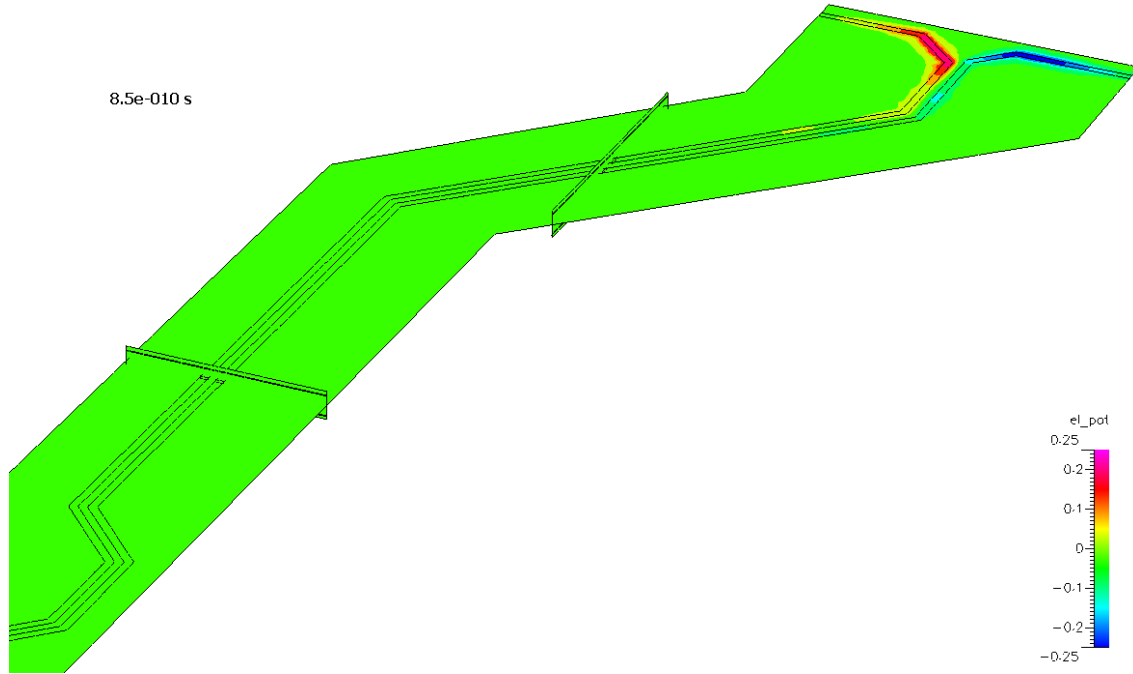


Figure 96. Several selected snapshots of that transient simulation for a differential signal (Gaussian pulse) of +0.4 and –0.4 volt applied to the input of the differential lines C4out and N_C4out.

The Impedance and Propagation Delay calculated for the C4out line by CFDRC full-wave EMAG solver were within 20% difference range as compared to the values extracted by Cadence Allegro tools.

9 CONCLUSIONS, COMMERCIALIZATION, TECHNOLOGY TRANSFER

9.1 Conclusions and Summary of Achievements

This report has presented the current status and results of the OE-IDEAS project within DARPA NeoCAD Program, aimed at developing, demonstration, and validation of new modeling concepts and tools in the following domains:

- new, efficient techniques of extraction of parasitics as well as new methods of full-wave EM modeling of parasitics in electrical interconnects, where high-frequency electromagnetic effects do not allow for using simplified SPICE-type models anymore;
- new, comprehensive CAD tools for integrated opto-electronic (O/E) circuits and systems, which would allow designers to analyze and optimize the full-path electrical-optical signal characteristics, at all the stages of the optically communicating circuits.

The major achievements of the program have already been outlined in the Introduction section, and here are presented again in brief:

- **First in the U.S. commercial software for high-fidelity multi-mode simulation of Lasers (VCSELs, edge-emit.) and Photodetectors, O'SEMI** from CFDRC:
 - new Optical Gain Model, with quantum-physics and thermal phenomena;
 - implemented Effective Index Method for Edge-Emitting Laser optics;
 - new Tunneling Current Model, based on quantum model of heterojunction;
 - currently installed and used by AFRL/WL, ARL (Adelphi, MD), NRL, UCSB, UC Santa Cruz, U. Florida, U. Arizona, U. Waterloo, Vanderbilt Univ., and others;
 - inquiries from: Sandia National Labs, LLNL, McMaster University, et al.
- **New capabilities in CFDRC's Full-Wave Electromagnetic Simulators for RF and Optical Interconnects:**
 - Signal monitoring and postprocessing: $V(t)$, $I(t)$, $Z(w)$, S-param(w);
 - Electromagnetic filament model implemented and initially tested;
 - CFDRC full-wave EM solvers offered to NeoCAD Community, and used by Univ. of Delaware, U. of Washington, and U. of Cincinnati.
- **CFDRC's Full-Wave 3D Simulator EMAG coupled with SPICE.**
- **Demonstrated Photonics Applications and provided Tutorials for EMAG users:**
 - 1) Optical waveguide coupling;
 - 2) Optical ring resonator;
 - 3) Photonic crystal waveguide;
 - 4) Photonic bandgap 2D matrix.
- **Simulated several NeoCAD benchmark structures and demonstrated results.**
- **CFD-Micromesh** - a unique, automated 3D mesher from IC layouts – **enhanced, offered to NeoCAD Community; new tutorials provided.**
 - Micromesh became during the NeoCAD Program a very useful tool for automatic generation of complex 3D models and computational mesh from layout formats used in EDA community (GDSII and CIF).
 - Micromesh has been successfully used by several NeoCAD teams and has become an indispensable component of full-wave EM modeling software in several NeoCAD design tools (e.g. Orora, LLNL, U. Wash., U. Pitt., SUNY, and others).
- At the University of Delaware:
 - **Designed, fabricated, tested and measured an optical transceiver chip**, and built a 3D model (with CFD-Micromesh).
 - Characterized and built a **3D model (with CFD-Micromesh) of the Mayo 10G system multi-chip module (MCM)**.
 - Formulated the **transmission-line model and the π -model of via-stub resonance** on system PCB's; with CFDRC simulated the model performance .
 - **Designed, fabricated, and tested Dual-Rate Current Mode Logic electrical IO's.**
- At Cornell University:
 - Established the **quantum transport model hierarchy** in density gradient, quantum hydrodynamic, full Wigner, and NEGF on large barrier tunneling problems. The benchmark problems are RTD and MOSFET gate tunneling.

- Established **large-signal transient analysis from S-parameters on nonlinear circuits**. The benchmark problems include high-power/high frequency transistors, nonlinear transmission lines, and buffer-insertion interconnect.
- Proposed and analyzed **pulse-based interconnect architecture and circuit implementation**, based on the large-signal transient analysis.
- Designed and verified the use of **patterned permalloy to control the on-chip magnetic fields** for accurate partial inductance extraction.
- Designed and verified the **use of undergrids to control CMOS interconnect dispersion on transmission lines** and co-planar waveguides.
- At the University of California Santa Cruz:
Developed, implemented, and tested compact models for mixed-level mixed-technology simulation, and demonstrated in VHDL-AMS for the following OE devices:
 - VCSEL and transmitter (including driver CMOS circuit)
 - Metal-Semiconductor-Metal (MSM) photodetector:
 - Raman Amplifier:
 - Erbium Doped Fiber Amplifier (EDFA):
 - Automation of O/E behavioral model parameters extraction from CFDRC 3D high-fidelity 3D simulator, for VCSEL and MSM photodetector.

9.2 Commercialization and Technology Transfer

Commercialization: This project resulted in several components with strong commercial value, including:

- Advanced 3D full-wave electromagnetics solver, **EMAG**, solving full Maxwell equations, has been developed and implemented as a integrated module in CFD-ACE+ Multiphysics software. It is currently marketed and distributed by ESI-Group, but CFDRC has the rights for adaptation and applications for DoD and US defense industry projects.
- **Micromesh** – An automated geometric modeler and mesher, customized for electronic circuits applications. CFDRC will commercialize it directly as a separate product, and as a module in 3rd party EDA software (Orora, Cadence, ...).
- **O'SEMI** – CFDRC-owned software tools for modeling and design of semiconductor electronic and optoelectronic devices. CFDRC is working with selected academic teams and DoD labs on software validation and qualification for commercial use. O'SEMI will be marketed to US industry in the form of customized tools, projects, and ultimately as a licensable software tool.
- **CFD-Maxwell** – CFDRC-owned flexible FDTD solver of full 3D Maxwell equations, with powerful capability of body-conforming and unstructured mesh solutions, for high-fidelity electromagnetic and optical/photonic design problems. It is being evaluated by academic teams, and will be used for projects with DoD labs, defense industry, for commercial industry projects, and a customized version as a licensable technology.

Technology Transfer: The Technology Transfer resulting from the OE-IDEAS project includes:

In the new “Coupled EM+Circuit” SBIR project, **CFDRC** and Dr. Vikram Jandhyala from **University of Washington** will be working closely with **Orora Design Technologies** towards bringing the new CAD framework and tools to RF/analog circuit designers and EDA market. The existing Orora tools (Arsyn, Arcap and Arana) can be used standalone, or used with tools from Cadence, Mentor Graphics, and other third-party tools, to form a complete analog/RF design flow (see Figure 97 below).

Figure 97. Analog/RF Design Flow with related Orora tools, and the new *Coupled EM+Circuit* tools to be implemented in the next CFDRS SBIR project (starting Spring 2004).

The new CFD-Micromesh software, greatly enhanced during this project, for automatic 3D solid model generation and meshing from electronic IC layouts, has a **very big and promising commercial potential**. The popular layout description formats, CIF and GDSII, are imported easily into CFD-Micromesh, allowing coupling the software with several commercial EDA design tools. The 3D model building and meshing in CFD-Micromesh is very fast and controlled by a user-friendly graphical user interface (GUI), as well as by external Python scripts or command lines. The automatically generated three-dimensional device models, using the

structured or unstructured 3D computational mesh in DTF format, can be imported directly into CFDRC's simulator CFD-ACE+ for multi-physics simulations, or to other NeoCAD EM solvers, after translation to the neutral mesh format also developed under the NeoCAD Program.

The **Cornell University** team (headed by Prof. Edwin Kan) will try to secure more external funding to continue the interconnect technology development and modeling.

- Both non-linear transmission line (NLTL) and permalloy technology have found applications in the DARPA Chip-scale Atomic Clock (CSAC) project under PM of Al Pisano.
- The large-signal reconstruction from small-signal responses is continuing development with more test cases and the AWE method (asymmetric waveform estimation).
- The pulse-wave interconnect has published its first architectural paper, and the future silicon implementation is uncertain at this stage. The work related to pulse-wave interconnect needs more evidence before commercialization can be considered.
- The permalloy transmission line work is under patent application.

The **University of California Santa Cruz** team (headed by Prof. Steve Kang) plans to share the developed compact models of OE devices as broadly as possible.

- As a first step, we plan to apply the models for a study of CD writing using blue laser diodes.
- For system studies and potential commercial applications, Prof. Kang's PhD student (Shu Wu) will work with Prof. Ken Pedrotti of UCSC to perform feasibility studies sponsored by National Semiconductor and the State of California.

Interaction of CFDRC Team with DoD Laboratories

Since the beginning of the NeoCAD program, CFDRC has established collaborative partnerships with three DoD Laboratories in areas directly related to this project:

- **AFRL Wright Patterson AFB.** Contact: Dr. Thomas Nelson, **Tactical Lasers Branch, Sensors Directorate**. CFDRC has delivered ACE+ software to AFRL for modeling optoelectronic devices (VCSELs, Photodetectors). AFRL arranged a DoD wide training of ACE+ at AFRL WL in Dayton, OH, on Oct 1-3, 2002. Seven people from Air Force and Army attended the workshop. One of the key areas of interest was electronic, thermal, and optical modeling of VCSELs.
- **ARL Adelphi MD.** Contact Dr. Brian Riely, **Optoelectronics Branch**. CFDRC representative visited ARL in June 2002, and Dr. Riely attended ACE+ training course at CFDRC in Huntsville in Aug 2002. Dr. Riely is already using ACE+ at ARL. The major interest of this collaboration is modeling of optoelectronic devices (VCSELs) and effects of optical emission on quantum wells.
- **NRL Washington DC:** Dr. Felix Buot, **Power Electronics Branch**. Dr. Buot spent one year sabbatical at CFDRC working on enhancements of quantum effects models in ACE+ SEMI module, and on modeling power semiconductor devices. CFDRC has installed ACE+ at NRL and Dr. Buot is using the code for Navy research projects.

Interaction with US Industry

During the course of this project CFDRC has established technical interaction contacts with several US industry partners including:

- **Rockwell Science Center**, Thousand Oaks (Dr. Rong Chow) joint project for analysis of wide bandgap semiconductor devices, and packaging problems of RF power electronics.
- **Mixed Technology Associates (MTA)**, Palo Alto, CA, (Dr. Daniel Yergeau): adaptation of ACE+ modeling tools for MTA TCAD device simulation tools for RF devices.
- **LSI Logic** (Ken Doniger): joint analysis of a test set consisting of three problems:
 - 1) A spiral inductor with substrate: calculate inductance and Q of the device.
 - 2) Three parallel conductors of trapezoidal cross-section: calculate the capacitance as a function of the trapezoidal angle.
 - 3) A thin metal serpentine structure: extract resistance and capacitance
- **IBM**, T. J. Watson Research Center, Yorktown Heights, NY, (Dr. Steven Koester), a member of DARPA TEAM Program: joint submission of a new SBIR proposal "Computational Analysis of Electromagnetic-Noise Tolerance of Nanoelectronic Devices" to DARPA.
- **Eastman Kodak Company**, Integrated Materials and Microstructures Lab, Rochester, NY, (Dr. Edward P. Furlani, Senior Principal Scientist): since beginning of March 2003, CFDRC has been providing software and support for simulation of photonic structures (waveguides, photonic crystals), and for optoelectronic semiconductor device simulation (VCSELs, photodetectors). Kodak plans to use CFDRC's software to design and optimize new optoelectronic devices.
- **Agilent R&D Center**, San Jose, CA, (Dr. Darek Burak): presentation of CFDRC's Optoelectronic software and discussion of future collaboration and software applications.
- **Lumileds Lighting** Advanced Labs, San Jose, CA, interested in modeling multiple quantum well light emitting diodes and design of anti-reflection surface features. Got O'SEMI trial license, software sales is being negotiated.

Several companies (e.g. **Samsung** from Korea, **NEC** from Japan) have expressed interest in using CFD-ACE+ electromagnetic tools (developed under this project) for modeling full-wave electromagnetic and parasitic effects in VLSI analog/RF ICs and interconnects. CFDRC has developed example demonstration cases and tutorials, which should lead to software sales and/or additional R&D projects.

Interaction with Academia

More than 600 academic users have been using ACE+ Multiphysics software worldwide. The ACE+ EMAG module for VLSI/RF Integrated Circuits, however, has not been formally released yet. At present CFDRC provides a "research" version to few selected academic partners. Some of them have committed to participate in joint development and enhancements of ACE+ EMAG. Academic teams using or evaluating the CFDRC electromagnetic codes include: Cornell Univ. (Prof E. Kan), SUNY (Prof. A. Pacelli), Georgia Tech (Prof. G. Cassinovi), Univ. Cincinnati

(Prof. R. Vemuri), Univ. of Illinois Urbana-Champaign (Prof. A. Cangellaris), Univ. Washington (Dr. P. Nikitin), and Univ. of Delaware (Dr. F. Kiamilev).

The newly developed O'SEMI package is currently used by several academic groups, including: two licenses at UC Santa Barbara (Prof. Larry Coldren, Prof. Joachim Piprek), UC Santa Cruz (Prof. S. Kang), University of Arizona, ECE Department/Optical Sciences (Prof. M. Neifeld), Univ. of Florida (Prof. Fan Ren's group, collaborating with ARL), Wilfrid Laurier University in Waterloo, Ontario (Prof. M. Wartak), Univ. of Texas in Arlington (Dr. B. Borovic), Vanderbilt University (Prof. Ron Schrimpf, Prof. Greg Walker).

Talks / Presentations (not listed in the published References)

- DARPA/MTO NeoCAD Kickoff Meeting in Malibu, California (Aug. 29-30, 2001): OE-IDEAS Project presentation was given by the PI, Marek Turowski.
- DARPA/MTO NeoCAD Program Review Meeting in San Antonio, TX (Feb. 27-28, 2002): OE-IDEAS Project presentation was given by the PI, Marek Turowski.
- NeoCAD OE-IDEAS Project Review by AFRL Monitors: Norman Bernstein, Paul Cook, (Rome Labs), and Thomas Nelson (WP-AFB), at CFDRC in Huntsville, AL (May 2, 2002): presentations were given by Marek Turowski and Andrzej Przekwas.
- DARPA/MTO TEAM/NeoCAD 2002 Summer Review in Providence, RI (Aug. 27-29, 2002): OE-IDEAS Project presentation was given jointly by the PI, Marek Turowski, and a subcontractor, Edwin Kan of Cornell Univ.
- Presentation at Agilent R&D Center (San Jose, CA), entitled "Computational Multiphysics Technology at CFDRC: Applications to Optoelectronics and Photonics", by Zbigniew Sikorski (CFDRC), on Jan 29, 2003.
- Presentation "Multiphysics modeling of intracavity VCSELs" at the *Photonic West 2003* Conference, Session *Physics and Simulation of Optoelectronic Devices XI*, given by Zbigniew Sikorski (CFDRC), on Jan 29, 2003.
- DARPA/MTO NeoCAD 2003 Winter Review in Arlington, VA (Feb. 19-20, 2003): OE-IDEAS Project presentation was given by the PI, Marek Turowski.
- DARPA TEAM/NeoCAD 2003 Summer Review in Monterey, CA (Sep. 15-17, 2003): OE-IDEAS Project presentation was given by the PI, Marek Turowski.

Patents

A new nonlinear interconnect scheme for integrated circuits, named *soliton interconnect*, has been conceived at the Cornell University (PI: Prof. Edwin Kan), using microwave circuit techniques to enhance information transaction on the interconnect network. The new technology has been filed for **patent** consideration.

9.3 Recommendations and Plans for Further Research

Based on the experience gained in this project we have identified several areas for further research, model development, and CFD-ACE+ software improvement. They can be grouped in following categories:

a) Interfaces with EDA Tools

In the present project we have greatly enhanced CFD-Micromesh, to interface microelectronic and 3D EM computational domains. The code is rapidly gaining acceptance and interest from broad range of applications. It is one of the biggest achievements of this project. Micromesh has however still several needs for system-level design, for example:

- semiautomatic block structured grid generation,
- mixed structured-unstructured grids,
- adaptive octree grids,
- parametric modeling in Micromesh,
- automated construction of filaments in Micromesh,
- tighter link with process fabrication and layout tools,
- boolean operations on masks for multilayer microstructures.

b) Automation and Parameterization of Model Setup

At present, CFD-ACE+ is suitable for single runs of a specific design or pre-arranged multi-runs for single variation in e.g. boundary conditions. There is a strong need for parametric modeling, scripting, optimization, and inverse problem solutions. A first step has been recently made at CFDRC by developing a Python scripting capability for our tools. We hope to expand this capability to more applications. Advanced academic and industrial users should be able to link the functions and modules in ACE+ modeling dataflow. Coupling of ACE+ with an optimization module would answer requests from several customers who have requested device optimization capability.

10 REFERENCES

10.1 Publications Resulting from This Project

1. Amitava Bhaduri, "Design, Test and Interface of CMOS and BICMOS Opto-Electronic Transceivers", MSEE Thesis (adv. Prof. F. Kiamilev), University of Delaware, 6/1/2002.
2. X. Wang, F. Kiamilev, and J. Ekman, "Power Minimization for Digital Optical Interconnects", Design Automation Conference *DAC 2002*, June10-14, 2002.
3. R. Tramel, M. Turowski, A. Hieke, and A. Przekwas, "Layout-Based 3D Electromagnetic Simulations of RF and Optical Interconnects", submitted to *DAC 2002* Conference, New Orleans, June 2002.

4. Z. Sikorski, Y. Jiang, M. Turowski, and A. Przekwas, "Coupled Full-Wave Optical and Semiconductor Analysis and Design of MSM Photodetectors", *9th Int. Conf. "Mixed Design of Integrated Circuits and Systems" - MIXDES 2002*, Wroclaw, Poland, 20-22 June 2002, pp.421-426.
5. J. Schultz, M. Turowski, R. Trammel, G. Henson, "3D Electromagnetic Simulation of Optoelectronic Transceiver Structures", *35th International Symposium On Microelectronics - IMAPS 2002*, Denver, Colorado, September 4-6, 2002.
6. P. Gui, F. Kiamilev, X. Wang, "Fully Differential Parallel Optical Transceiver with Fast Power-down Capability", *OSA Optics in Computing Topical Meetings*, June 2003, Washington D. C.
7. P. Gui, F. Kiamilev, X. Wang, M. McFadden, C. Kuznia, J. Ekman, J. Deroba, and M. Haney, "A Source Synchronous Double Data Rate (DDR) Optical Transceiver Link", *ASME International Electronic Packaging Technical Conference*, July 2003, Maui, Hawaii.
8. P. Gui, F. Kiamilev, X. Wang, M. McFadden, C. Kuznia, J. Ekman, X. Wang, J. Deroba and M. Haney, "Source-Synchronous Double Data Rate (DDR) Parallel Optical Interconnects", submitted to *IEEE J. Lightwave Technol.*, March 2003.
9. P. Wang and E. C. Kan, "Dispersion and resonance of on-chip interconnect lines with underlayer orthogonal metal grids", *12th Topical Meeting on Electrical Performance of Electronic Packaging (EPEP)*, Princeton, NJ, Oct. 27-29, 2003.
10. P. Wang and E. C. Kan, "High-frequency permalloy permeability extracted from scattering-parameters", *9th Joint MMM-Intermag Conference*, Anaheim, CA, Jan. 5-9, 2004.
11. P. Wang and E. C. Kan, "High-speed interconnects with underlayer orthogonal metal grids", accepted for publication in *IEEE Trans. Packaging and Component Technology*.
12. P. Wang, G. Pei and E. C. Kan, "Pulsed wave interconnect", accepted for publication in *IEEE Trans. VLSI Systems*.
13. P. Wang, N. Tien, and E. C. Kan, "Permalloy loaded transmission line for high-speed interconnects", *IEEE International Interconnect Technology Conference (IITC)*, June 2-4, 2003, San Francisco, CA.
14. P. Wang, N. Tien, and E. C. Kan, "Permalloy loaded transmission line for high-speed interconnects", *IEEE Trans. Electron Devices*, vol. 51, no. 1, pp. 74-82, Jan. 2004.
15. P. Wang, V. S. Kaper, R. J. Shealy and E. C. Kan, "Transient Analysis of Nonlinear Microwave Circuits Using Small-signal Scattering Parameters," *RFIC 2003*, June 8-10, Philadelphia, PA.
16. P. Wang, W. Ni, N. C. Tien, and E. C. Kan, "High-frequency permalloy permeability extracted from scattering-parameters", accepted for publication in *J. Appl. Phys.*
17. Shu Wu and S. M. Kang "Modeling and time domain simulation of VCSEL using VHDL-AMS", proceeding of *2003 Southwest Symposium on Mixed-Signal Design, SSMSD'03*.

18. V. Narayanan and E. C. Kan, "A New Quantum Hydrodynamic Approach with Explicit Treatment of Large Barriers", submitted to *SISPAD 2003*.
19. V. Narayanan and E. C. Kan, "Quantum hydrodynamic modeling of charge transport based on the exact, large-barrier equilibrium density matrix", *Techcon 2003*, Dallas, TX, Aug. 25-27, 2003.
20. Z. Sikorski, Y. Jiang, T. Czystanowski, A. Przekwas, and M. Turowski, "Coupled Multiphysics Modeling of Semiconductor Lasers", *2003 Nanotechnology Conference and Trade Show - NanoTech2003*, San Francisco, California, U.S.A., February 23-27, 2003.
21. X. Wang, F. Kiamilev, G. Papen, J. Ekman, P. Gui, M. McFadden, J. Deroba,, M. Haney, and C. Kuznia, "Performance-based Power Optimization for Digital Optical Interconnection", submitted to *IEEE J. Lightwave Technol.*, April 2003.
22. Z. Sikorski, M. Turowski, Y. Jiang, T. Czystanowski, and A. Przekwas, "Advanced Computational Tools for Multiphysics Analysis and Design of Semiconductor Lasers" (invited paper), *10th Int. Conf. "Mixed Design of Integrated Circuits and Systems" - MIXDES 2003*, Lodz, Poland, 26-28 June 2003.
23. X. Wang, F. Kiamilev, G. Papen, J. Ekman, P. Gui, M. McFadden, J. Deroba,, M. Haney, and C. Kuznia, "Packaging Friendly Parallel Optical Transceivers", *ASME International Electronic Packaging Technical Conference*, July 2003, Hawaii.
24. X. Wang, Y. Li, F. Kiamilev, J. Ekman, and G. Arce, "Power Efficient Parallel Optical Communication Links", *OSA Optics in Computing Topical Meetings*, June 2003, Washington D. C.
25. Z. Sikorski, M. Turowski, Y. Jiang, T. Czystanowski, A. Przekwas, and M.S. Wartak, "Multiphysics Modeling Tools For Vertical Cavity Surface Emitting Lasers (VCSEL)", *IEEE/LEOS International Conference on Numerical Simulation of Semiconductor Optoelectronic Devices (NUSOD'03)*, October 13-16, 2003 Tokyo, Japan.

10.2 Other References

- Azadeh M. (2000), R.B. Darling, and W. R. Babbitt, "A Model for Optoelectronically Interconnected Smart Pixel Arrays", *IEEE Journal of Lightwave Technology*, Vol. 18, No. 10, Oct. 2000, pp.1437-1444.
- Beattie M. (2000), Gupta S. and Pileggi L., "Hierarchical Interconnect Circuit Models", *ICCAD 2000*, p.215.
- Cangellaris A. (1999), Celik M., Pasha S., and Zhao L., "Electromagnetic Model Order reduction for System-Level Modeling", *IEEE Trans. Microwave Theory Tech.*, Vol. 47, No. 6, June 1999, pp.840-850.
- Cullum J.(1998), Ruehli A. and Tong Zhang: "Model Reduction for PEEC Models Including Retardation", *IEEE 7th Topical Meeting On Electrical Performance Of Electronic Packaging*, EPEP'98, Oct 1998, West Point, NY
- Griese E. (2000a), "Optical Interconnections on Printed Circuit Boards", in "Optics in Computing", SPIE Vol. 4089 (2000), pp.60-85.

- Griese E. (2000b), Himmeler A., Schrage J., "An Approach to Model Optical Multimode Interconnects for Time Domain Simulations", in "Optics in Computing", SPIE Vol. 4089 (2000), pp.958-968.
- Haney M. (2000), Christensen M., Milojkovic P., Fokken G., Vickberg M., Gilbert B., Rieve J., Ekman J., Chandramani P., and Kiamilev F., "Description and Evaluation of the FAST-Net Smart Pixel-Based Optical Interconnection Prototype", *Proc. IEEE*, vol.88, No.6, June 2000, pp.819-828.
- Li Y. (2000) and Towe E. (Editors) – Special Issue on Optical Interconnections for Digital Systems - Introduction, *Proc. IEEE*, vol.88, No.6, June 2000, pp.723-726.
- Liu Y. (2000), Strzelecka E., Nohava J., Hibbs-Brenner M., and Towe E., "Smart Pixel Array Technology for Free-Space Optical Interconnects", *Proc. IEEE*, vol.88, No.6, June 2000, pp.764-768.
- Mangold T. (1999) and Russer P., "Full-Wave Modeling and Automatic Equivalent-Circuit Generation of Millimeter-Wave Planar and Multilayer Structures", *IEEE Trans. Microwave Theory Tech.*, Vol. 47, No. 6, June 1999, pp.851-858.
- Miller D. (2000), "Rationale and Challenges for Optical Interconnects to Electronic Chips", *Proc. IEEE*, June 2000, p.728.
- Pinello W. (1997), Cangellaris A. C., and Ruehli A., "Hybrid electromagnetic modeling of noise interactions in packaged electronics based on the partial-element equivalent circuit formulation," *IEEE Trans. Microwave Theory Tech.*, vol. 45, pp. 1889–1896, Oct. 1997.
- Restle P. (1999), Ruehli A., Walker S.G., "Dealing with inductance in high-speed chip design", DAC'99, New Orleans, 1999, pp.904-909.
- Ruehli A. (1996): "Partial Element Equivalent Circuit (PEEC) Method and its Application in the Frequency and Time Domain", *IEEE 1996 International EMC Symposium*.
- Walker M.G. (2000), "Modeling the wiring of deep submicron ICs", *IEEE Spectrum*, March 2000, pp.65-71.
- Zheng J. (2000), Y.C. Hahm, V.K. Tripathi, and A. Weisshaar, "CAD-Oriented Equivalent-Circuit Modeling of On-Chip Interconnects on Lossy Silicon Substrate", *IEEE Trans. Microwave Theory Tech.*, Vol. 48, No. 9, Sep. 2000, pp.1443-51.

DARPA NeoCAD Program
OE-IDEAS Project

Final Report

APPENDIX A

Compact Model Extraction for Opto-Electronic Devices

*PI: Prof. Sung-Mo Kang
University of California, Santa Cruz*

This Appendix A to OE-IDEAS Final Report is composed of four chapters.

In chapter I we present VHDL-AMS implementation of the rate equation based Vertical-Cavity Surface-Emitting Laser (VCSEL) model, discussion of the time domain simulation results for different kinds of VCSEL, a prototype of a transmitter comprised of a VCSEL and a CMOS driving circuit, and the model parameter extraction issue.

In chapter II we present VHDL-AMS implementation of a Metal-Semiconductor-Metal photodetector (MSM-PD) model, and simulation results.

In chapter III we present VHDL-AMS implementation of an Erbium Doped Fiber Amplifier (EDFA) model, and simulation results.

In chapter IV we present VHDL-AMS implementation of a Raman Amplifier (RA) model, and simulation results.

CHAPTER I

MODELING AND SIMULATION OF VCSEL AND TRANSMITTER

1.1. Model description

The model in [Mena,1999] starts from spatially dependent rate equations. To reduce the computational complexity the carrier distribution was modeled by Bessel series and mode profile was modeled by a Laguerre-Gaussian function [Mena,1999]. Through integration we obtained spatially independent rate equations as the circuit-level VCSEL model, which is a series of ODEs (Ordinary Differential Equations). The complete mathematical model and physical explanation can be found in [Mena,1999].

The VHDL-AMS implementation of this VCSEL model is straightforward. After the port map of the device model was determined, the ODEs can be directly imbedded into the model. It should be noted that even though our implementation and simulation are in *SMASHTM* provided by *Dolphin Integration*, after some modification the VHDL-AMS VCSEL model can be used by any simulation tool supporting VHDL-AMS. According to the ability of the simulation tool we can change the time unit of the model parameters to help achieve the convergence in simulation. Following code expresses the implementation of VCSEL by VHDL-AMS.

```
library IEEE;
use IEEE.math_real.all;

entity VCSEL is
  generic(
    --parameters of VCSEL---
    wq: real:= 1.60219e-19; ----electron charge
    wg0: real:= 3.0e4;
    ...
    port( terminal p, n, phout: electrical);
end entity VCSEL;

architecture Singlemode of VCSEL is
  --quantities and variable declaration
  quantity lin through p ; --input current
  ...
  -- use break to set the initial condition
  break N0 => 0.0;
  ...
  --set variable value
  gain:=...
  ...
  -- rate equations
  N0'dot == wita*lin/(wq)-N0/(wtaon)-...;
  ...
  -- output laser power
  pw:= wkf0* S0;
end architecture singlemode;
```

1.2. Simulation results and discussion

1.2.1. VCSELs

As a typical demonstrative simulation example, we simulated the response of a VCSEL under two types of input, namely square wave and sinusoidal wave. Simulation results are shown in Fig 1-1.

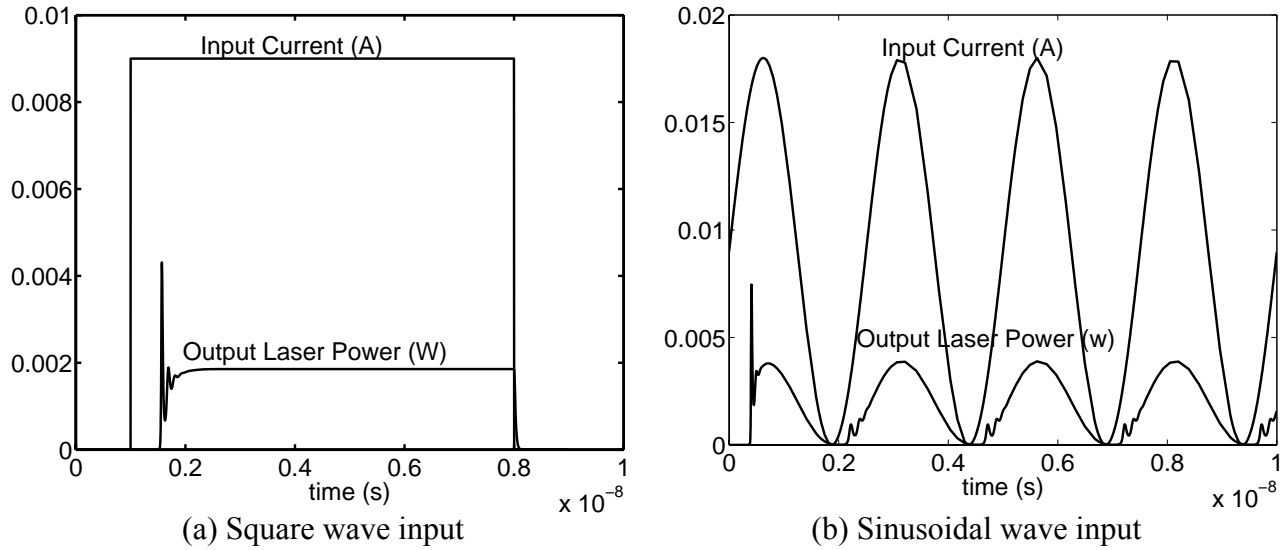


Fig 1-1. VCSEL responses under different inputs

From the simulation results we observe that the typical large signal response of VCSEL is oscillation followed by a steady state output which follows the input signal wave form. The differences lie in the oscillation amplitude and time. Simulation results showed the oscillation of laser under square wave input was much severer than the sinusoidal input. It is because the rise and falling edges of square wave are much sharper than the sinusoidal wave the suddenly inputted carriers need more time to be distributed. The laser diode would need more time to reach its steady state.

Due to the lack of the experimental data for large signal response of VCSEL, we chose an eye diagram reported in [Gustavsson,2002] to verify the multimode simulation ability of our model. This 850-nm oxide-confinement top-emitting VCSEL consists of an n-GaAs substrate, a 22 pair $\text{Al}_{0.92}\text{Ga}_{0.08}\text{As}$ - $\text{Al}_{0.12}\text{Ga}_{0.88}\text{As}$ p-DBR on top, a 33 pair $\text{Al}_{0.92}\text{Ga}_{0.08}\text{As}$ - $\text{Al}_{0.12}\text{Ga}_{0.88}\text{As}$ n-DBR on the bottom, three 6-nm GaAs quantum wells sandwiched by 2 8-nm $\text{Al}_{0.3}\text{Ga}_{0.7}\text{As}$ confinement layer, and a 40-nm $\text{Al}_{0.98}\text{Ga}_{0.02}\text{As}$ layer to create index-guiding oxide aperture. This kind of VCSEL is preferred light source for short distance high speed fiber communication system [Man,1998].

The simulation results show that when the drive current is well above the threshold, an optical bump occurred in the turn-off transient. Due to the strong index-guiding along the transverse direction in oxide-confined VCSELs, the transverse optical mode is confined in a small oxide

aperture. As a result the carriers in the central region are depleted much faster than other regions due to stronger central stimulated recombination processes. When the injection current source is suddenly turned off the carriers in the peripheral region diffuse to the central region, which could make the VCSEL turn on again. This spatial hole burning (SHB) effect results in interaction between the optical mode and carrier profiles. As a result the VCSELs have a poor turn off characteristic. The simulation results in Fig 1-2. show good agreement with experimental data in [Gustavsson, 2002] (Fig 1-10. and Fig 1-11).

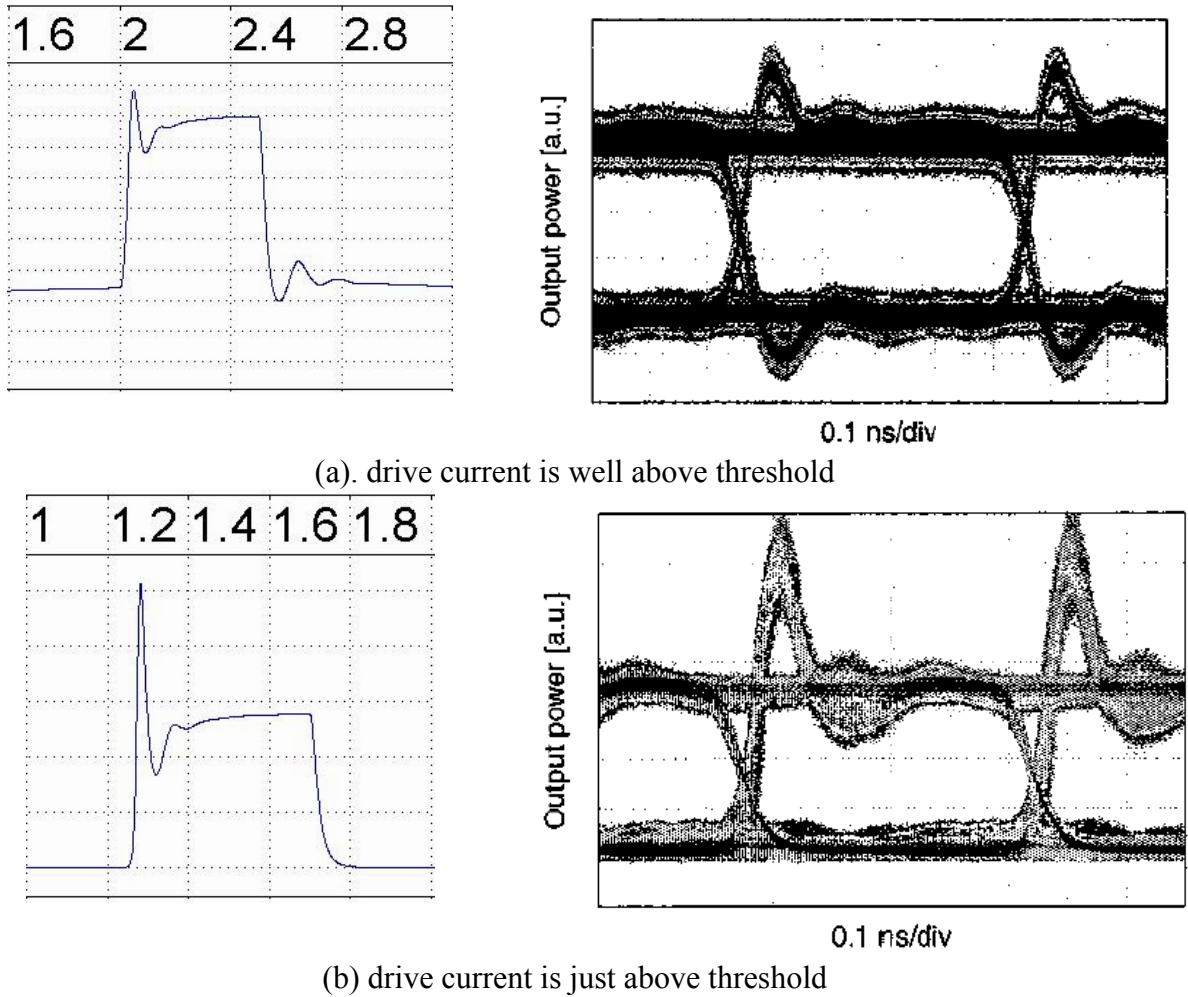


Figure 1-2. Simulation results vs. experimental data

1.2.2 Transmitter

As we mentioned earlier VHDL-AMS is a good choice to do mixed-mode simulation. We used a simple transmitter to show this advantage. Even though the simulation was not done for a real transmitter, we believe that after reasonable modification of the parameters we can use this process to simulate real systems.

The schematic of a driving circuit is borrowed from [Chen,1997]. The VCSEL is a typical index-guided InGaAs VCSEL. In the simulation process 0.35 μm technology file was used. Fig 1-3 are

the simulation results of driving circuit and transmitter. In Fig 1-3 (a), V(INR) represents the input signal and V(OUT) is the output of the driving circuit. Under a 200 MHz 1 V to -3.5 V input voltage signal the driving circuit generated a 200 MHz 2 mA to 8 mA current signal. For speed consideration the threshold current of the VCSEL is chosen to be about 1.8 mA to make it operated above threshold. When 2 mA current is inputted, the VCSEL would generate a weak laser signal which could not be detected by the receiver. The peak output power is about 2 mw and the difference between the peak and bottom is around 1.8 mW which is not desirable in optical communication system. By introducing a larger gain VCSEL such as thin-oxide-aperture we can get a better transmission. The whole simulation procedure suggests that because of its various compatibility VHDL-AMS is a very good choice to do the optoelectronic system modeling and simulation.

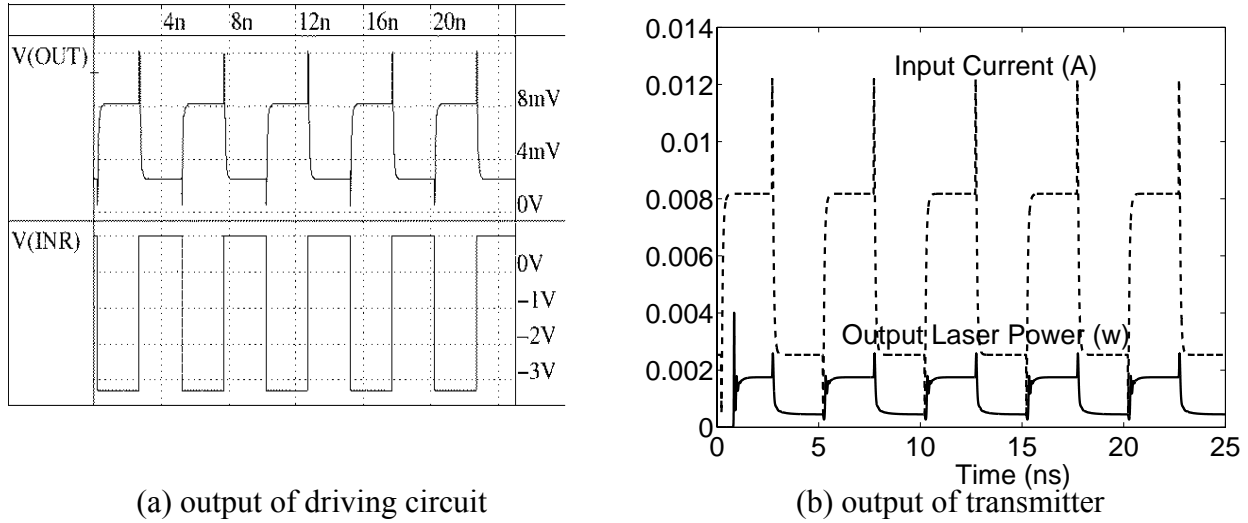


Fig 1-3. Simulation results of the transmitter

1.3. Model parameters extraction

1.3.1 Basic flow chart

During the last two decades much research has been done on modeling and simulation research on optoelectronic devices and systems. The circuit-level model is more efficient in system level simulation compared to device-level model, which requires great details of device physics. Usually this kind of model needs multidimensional analysis of spatial behavior, which is not suitable for system simulation. Another advantage of circuit-level model is that it can be implemented into conventional electronic simulation tool such as SPICE. An important before the model implementation is model parameter extraction from experimental data or high fidelity device-level simulation.

For automatic model parameters extraction for circuit-level VCSEL model, we chose the high fidelity simulation tool CFD-ACE+. By taking the advantage of the compatibility of Python with CFD-ACE+, we can take Python as the platform to implement our algorithm. By importing additional numerical enhancement module, Numpy, the implementation can be done more easily than directly implementing in C. The main procedure is shown below.

- Step 1. Set up device-level VCSEL model in CFD-ACE+.
- Step 2. Get L-I and I-V curve in different temperature through Simulation Manager.
- Step 3. Extract out the parameters of circuit-level VCSEL model.
- Step 4. Put the parameters extracted into circuit-level VCSEL model.
- Step 5. Simulate the VCSEL by VHDL-AMS simulation tool.
- Step 6. Compare the simulation results with the output of CFD-ACE+.
- Step 7. Repeat step 2 to step until the simulation results from different simulation tools are close enough.

The corresponding flow chart was shown in Fig. 1-4.

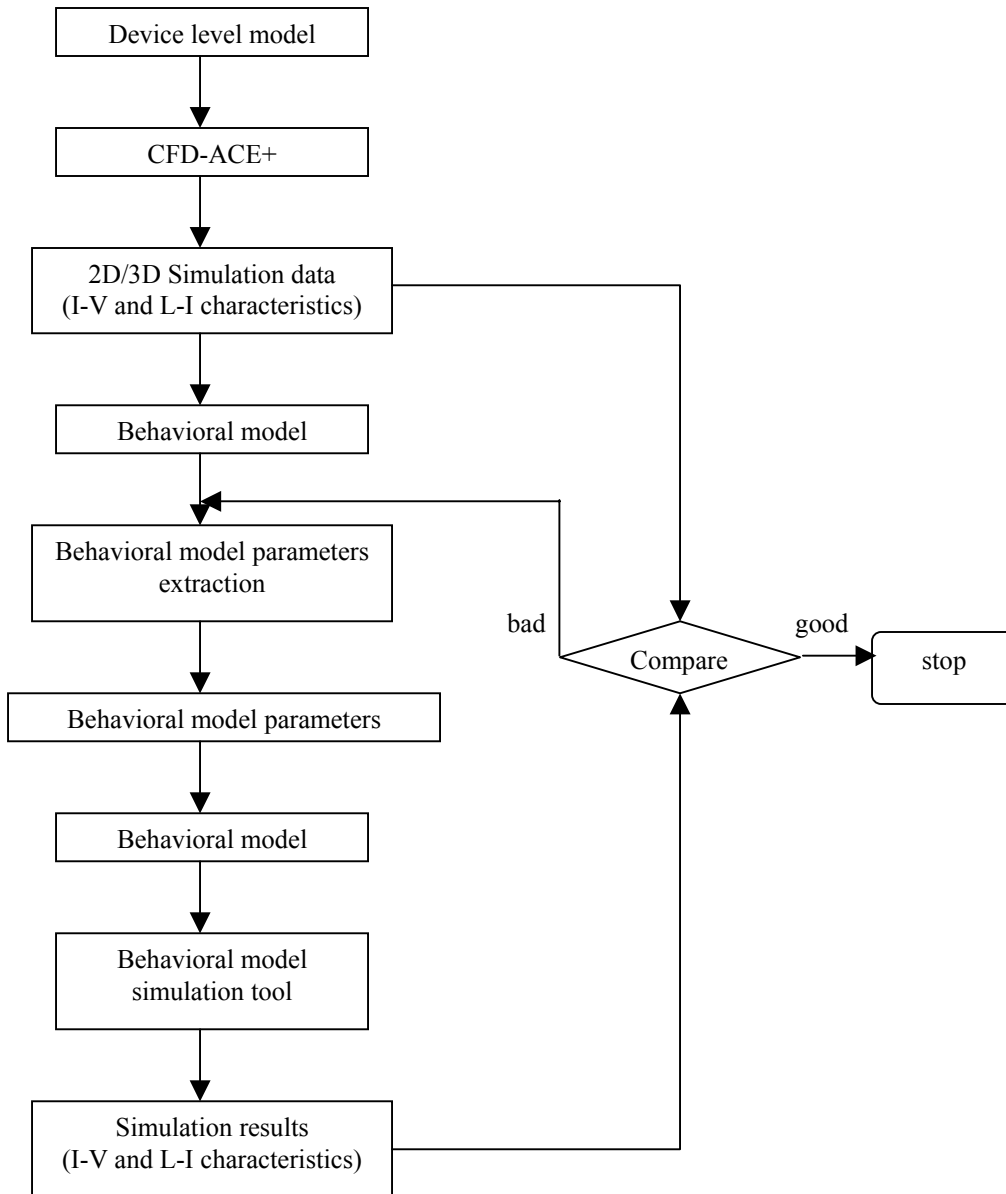


Fig 1-4. Flow chart of automatic parameters extraction for circuit-level VCSEL model procedure.

1.3.2 Linear part extraction

1.3.2.1 Extraction methodology

In order to extract model parameters from experimental data or high fidelity simulation tool we need to use curve fitting and optimization algorithms. At the beginning we can choose least square method for linear fitting. We start from the function of output light power P_0

$$P_0 = \eta(T)(I - I_{th} - I_{off}(T)) \quad (1-1)$$

where T is temperature, I is injected current, I_{th} is threshold current, η is the differential slope efficiency and I_{off} is the offset current.

The offset current could be an empirical function such as polynomial function.

$$I_{off}(T) = \sum_{i=0}^n a_i T^i \quad (1-2)$$

The temperature is related to the total input power, IV , and output light power, P_0 , as following format.

$$T = T_0 + (IV - P_0)R_{th} - \tau_{th} \frac{dT}{dt} \quad (1-3)$$

where R_{th} is the VCSEL's thermal impedance, τ_{th} is a thermal time constant, T_0 is the ambient temperature, and V is the laser voltage. Under dc conditions, the dT/dt term disappears. Thus, from the resulting equation it is clear that $(IV - P_0)$ models the power dissipated in the VCSEL. Here we assume that any power not carried in the optical output is dissipated as heat in the device. From L-I and I-V curve we found output light power is relatively small compared with the IV term so we can neglect P_0 in Eq. (1-3). The simplified relation between T and IV is given below.

$$T = T_0 + IVR_{th} \quad (1-4)$$

If we put (1-2) and (1-4) into (1-1) and after some combination, we can find (1-1) now becomes the following.

$$P_0 = \eta(T) \left[\sum_{i=0}^n (a_i I^i + b_i T^i) \right] \quad (1-5)$$

Obviously if we choose n as a large number it would be more accurate but also more complicated. Here we choose $n=4$ for both accuracy and efficiency. So far the VCSEL model in CFD-ACE+ can not simulate the roll over of L-I characteristic of VCSEL, and we can set $a_2 - a_4$ to zero. Fig 2-5. shows the simulation results.

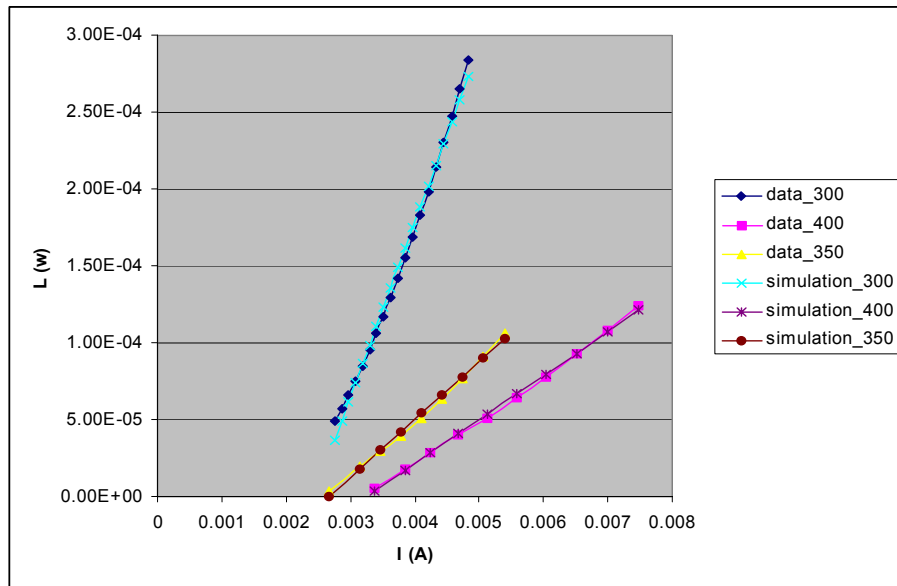


Fig 1-5. The simulation results using extracted parameter and data from CFD-ACE.

CHAPTER II

MODELING AND SIMUALTION OF MSM PHOTODETECTOR

2.1. Model description and simulation results

2.1.1. Numerical model

2.1.1.1. Model setup

The behavior of photo-generated carriers in MSM photodetector can be described by Poisson's equation and carrier continuity equations that are given below

$$\begin{aligned}
 \varepsilon_0 \varepsilon_s \nabla^2 \psi &= -q(p - n + N_D - N_A) \\
 -\frac{1}{q} \nabla \bullet J_n - G_n + R_n + \frac{\partial n}{\partial t} &= 0 \\
 \frac{1}{q} \nabla \bullet J_p - G_p + R_p + \frac{\partial p}{\partial t} &= 0 \\
 J_n &= q\mu_n n E_n + qD_n \nabla n \\
 J_p &= q\mu_p p E_p - qD_p \nabla p
 \end{aligned} \tag{2-1}$$

where $R_{n/p}$ and $G_{n/p}$ are the electron/hole recombination and generation rate, ψ is the electrostatic potential, other parameters have their usual meaning. The optical generation rate is assumed to be gaussian for the impulse response and is given as

$$G_n = G_p = \frac{W_p}{h\nu} \alpha_{abs} \bullet \exp\left(-\frac{(t-t_0)^2}{\sigma_t^2}\right) \exp\left(-\frac{(x-x_0)^2}{\sigma_x^2}\right) \tag{2-2}$$

where W_p is the peak optical power density incident on the surface, $h\nu$ is photon energy, α_{abs} is the absorption coefficient. The carrier recombination rate can be modeled using Shockley-Hall-Read (SHR) theory. After assuming that excess carrier density exceeds the intrinsic carrier concentration we can get a simple form, $n/2\tau_n$ and $p/2\tau_p$.

We want to reduce the complexity for circuit-level model extraction. Since most of MSM photodetectors are working under a bias voltage which is larger than the flat-band voltage we can use $E_n=E_p=\psi/d$ instead of Poission's equation. Above equations plus infinite recombination, $(n,p(0,t)=n,p(L,t)=0)$, boundary conditions complete our mathematical model for MSM photodetector.

2.1.1.2.Simulation results

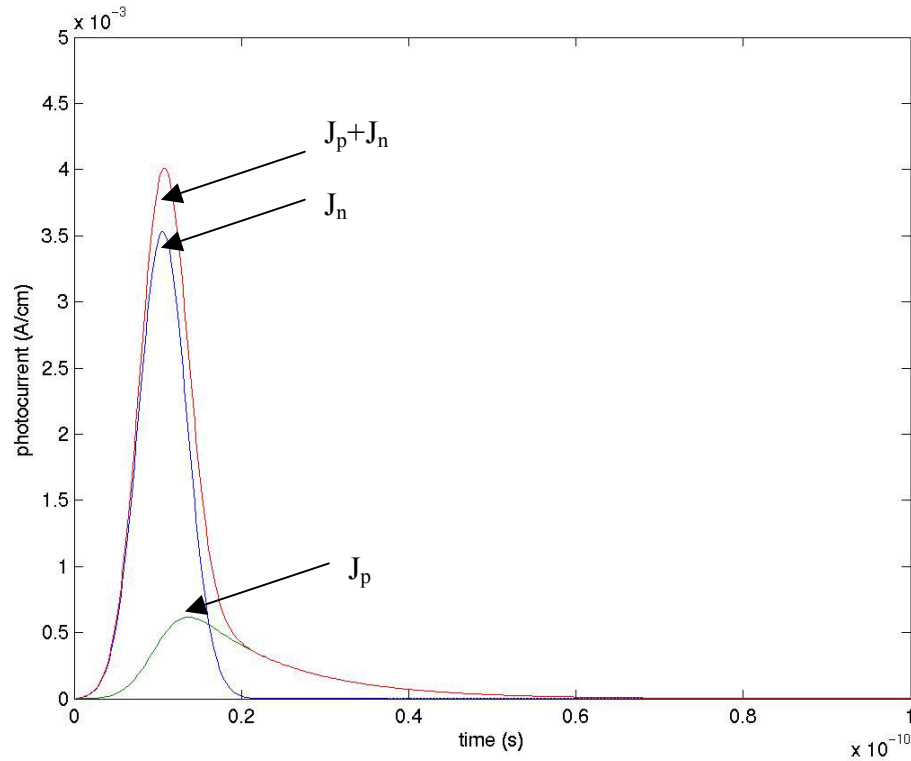


Fig. 2-1. Photocurrent in MSM photodetector

The model above can be solved by using the finite difference method. We chose a GaAs based MSM photodetector to describe the typical response of a MSM photodetector under a light impulse. The simulation results are shown below.

Fig 2-1 shown the photocurrent generated by the device. From the figures we can see that since the electrons are much faster than holes the tail of the holes photocurrent is mostly due to the holes.

2.1.2. Circuit-level model

2.1.2.1.Model setup

2.1.2.1.1. Steady state

In dc steady state under constant illumination, the photocurrent is proportional to the electron-hole pair generation rate as shown below

$$I_{ph} = w(1-R)(1-e^{-\alpha d}) \frac{\eta \cdot qP}{h\nu} \quad (2-3)$$

where I_{ph} is the photocurrent, w is the area ratio (area transparent to light/ area exposed to light), α is the absorption coefficient, d is the thickness of the absorption layer, η is the quantum efficiency, $h\nu$ is the photon energy, p is the incident light power

As the bias voltage is raised the behavior of MSM photodetector can be treated for two cases wherein the bias voltage is lower or higher than the flat-band voltage. When the bias voltage is lower than the flat-band voltage the potential barrier of the holes is lowered by the increased bias voltage, which results in rapid increase of the current. when the bias voltage reached the flat-band voltage, the hole barrier approaches its limiting magnitude, Schottky barrier height. Further increase in voltage will cause the current to increase slowly. Thus we use the following two formulas to model the photocurrent,

$$I_{dc} = I_0 \left(e^{\frac{qV(2V_{FB}-V)}{nKT}} - 1 \right) + I_{ph} \cdot A e^{\frac{B}{V}}, V < V_{FB} \quad (2-4)$$

$$I_{dc} = I_{ph} \cdot \left(1 + A e^{\frac{B}{V}} \right), V \geq V_{FB} \quad (2-5)$$

where I_{dc} is the total current, V is the bias voltage, V_{FB} is the flat-band voltage, T is the temperature, K is the Boltzmann constant, n , A , B , I_0 are fitting parameters.

We implemented this model using VHDL-AMS as following.

```

-----
-- The DC model of MSM_PD definition begins.....
-----
LIBRARY DISCIPLINES;
LIBRARY IEEE;

USE DISCIPLINES.ELECTROMAGNETIC_SYSTEM.ALL;
USE IEEE.MATH_REAL.ALL;

--entity declaration.
ENTITY MSMDC IS
  GENERIC ( T : REAL:=300.0;--k
            d : REAL:=1.0e-4;--cm
            ...
  );
  PORT(TERMINAL p,m: ELECTRICAL;
        quantity ph :real); --Interface ports.

```

```

END;

--architecture declaration.
ARCHITECTURE behav OF MSMDC IS
  --quantity declarations.
  constant q :real:=1.6e-19;--C
  constant hc :real:=6.6262e-34;--Js
  constant k :real:=1.3807e-23;--J/k

  QUANTITY Iph : REAL;
  QUANTITY I0 : REAL;
  QUANTITY v_in ACROSS i_out THROUGH p TO m;
BEGIN

  ph==0.9823e-6/10.0**1.5;--w
  Iph==w*(1.0-R)*(1.0-exp(-1.0*alfa*d))*eta*q*ph/hc/miu;
  I0==Iph/(exp(q*Vfb**2/n/k/T)-1.0);

  if v_in<Vfb use
  i_out==I0*(exp(q*v_in*(2.0*Vfb-v_in)/(n*k*T))-1.0)+Iph*A*exp(-1.0*B/v_in);
  else
  i_out==Iph*(1.0+A*exp(-1.0*B/v_in));
  end use;

END;

```

2.1.2.1.2. Transient response

The impulse response of MSM photodetector can be modeled as a finite Fourier sine series

$$J_{pulse} = J_p \cdot \sum_{n=1}^{\infty} \frac{2}{n\pi} \sin\left(\frac{n\pi}{2}\right) g_n(t-t_0) \quad (2-6)$$

$$g_n(t) = \lambda_n^2 \cdot e^{-\lambda_n^2 t}, \quad \lambda_n^2 = \frac{(n\pi)^2}{\tau} \quad (2-7)$$

where J_p is fitting parameter, τ is transit time.

The responses of other inputs can be described as the convolution of J_{pulse} with the incident light wave function.

$$J_{other} = J_{pulse} * ph(t) = J_p \cdot \sum_{n=1}^{\infty} \frac{2}{n\pi} \sin\left(\frac{n\pi}{2}\right) \int_0^t g_n(t-t_0) ph(t_0) dt_0 \quad (2-8)$$

where $ph(t)$ is incident light wave function.

2.1.2.2.Simulation results

To demonstrate the model we did simulation corresponding to the experiment data in reference [Krishnamurthy, 2000] and [Aliberti, 2002]. Fig 2-2 corresponded to the Fig 4 in [Krishnamurthy, 2000] and Fig 2-3 corresponded to Fig 1 in [Aliberti, 2002]. The parameters used for simulation are shown in the figures. Our simulation results matched those in [Krishnamurthy, 2000], [Aliberti, 2002].

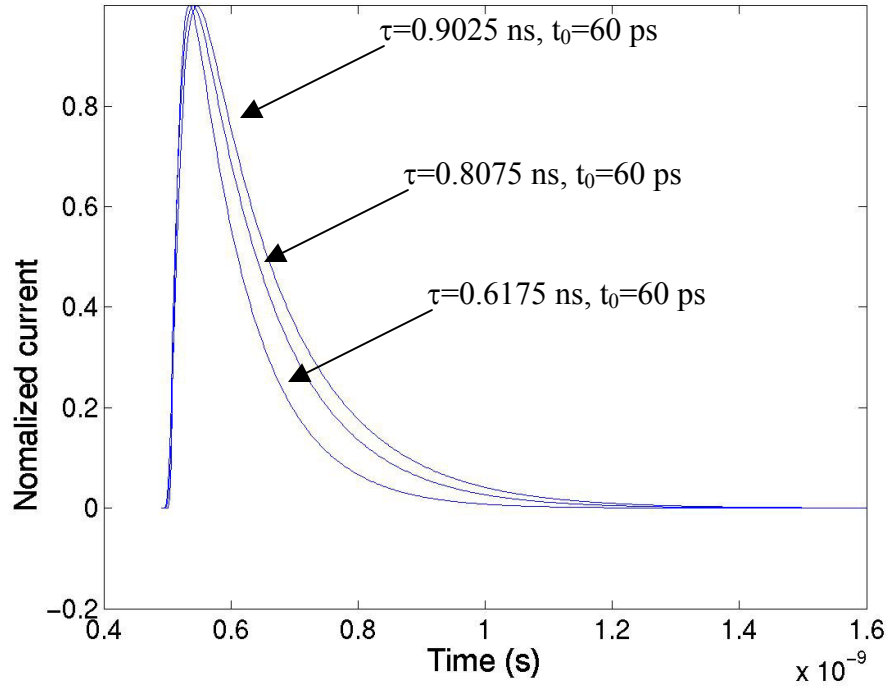


Fig 2-2. Simulation results of impulse response of MSM-PD in [Krishnamurthy, 2000]

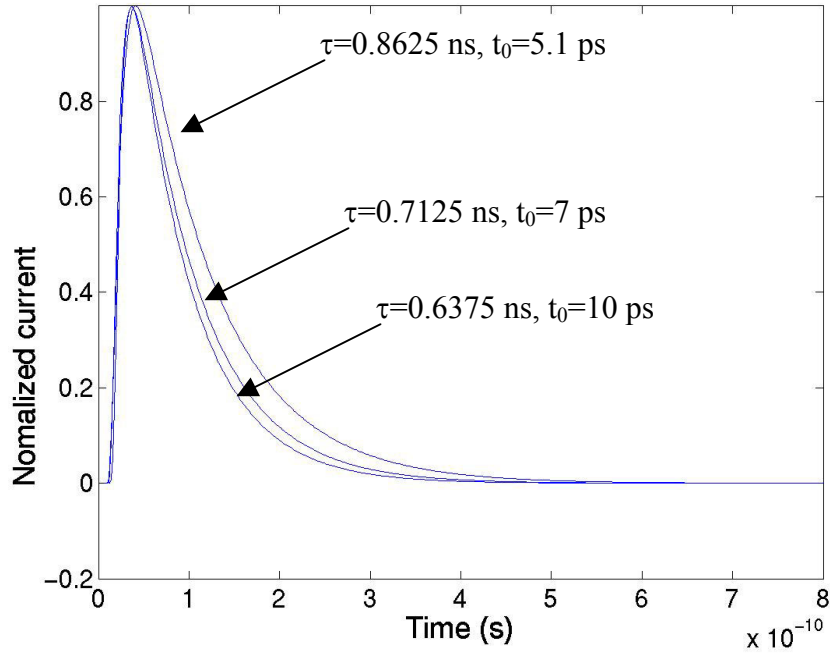


Fig 2-3. Simulation results of impulse response of MSM-PD in [Aliberti, 2002]

It should be noted that depending on the ability of the simulator we can change the time unit of the parameter to help the simulator converge to a correct numerical result.

The typical cases are the step and sinusoid responses. The simulation results are shown in Fig 2-4 and Fig 2-5. Because there is no published experimental data available, the parameters chosen in simulation do not correspond to the real devices. The transit time was chosen to be $19.6 \mu\text{s}$ in simulation for demonstration purpose.

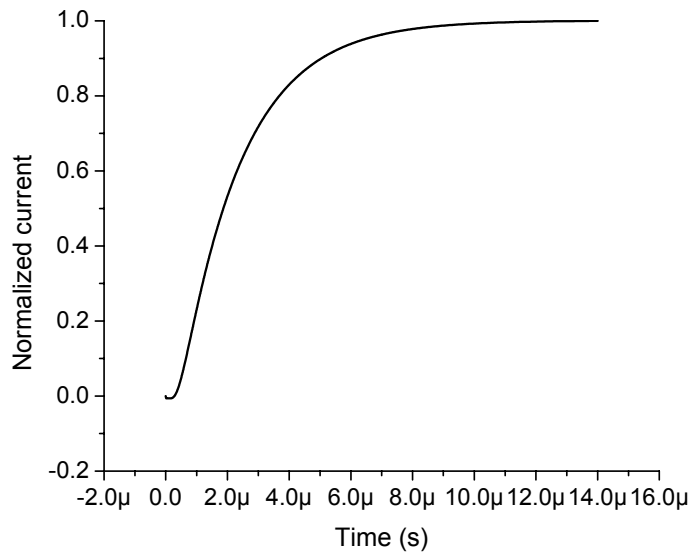


Fig 2-4. Simulation result of the MSM-PD response under step function input

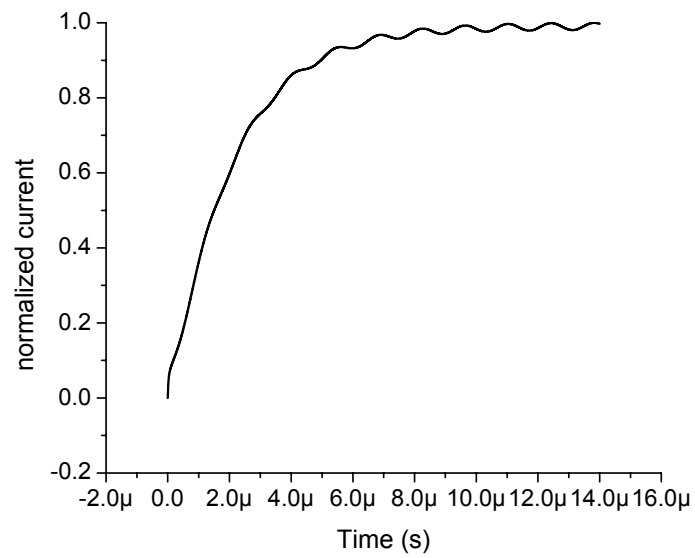


Fig 2-5. Simulation result of the MSM-PD response under sine function input

CHAPTER III

MODELING AND SIMUALTION OF EDFA

3.1. Model description

Most simply we can model EDFA as a three level laser system as Fig. 3-1. So we can write rate equations as following [Giles, 1991]:

$$\begin{aligned}\frac{dN_1}{dt} &= -R_{13}N_1 + R_{31}N_3 - W_{12}N_1 + W_{21}N_2 + A_{21}N_2 \\ \frac{dN_2}{dt} &= W_{12}N_1 - W_{21}N_2 - A_{21}N_2 + A_{32}N_3 \\ \frac{dN_3}{dt} &= R_{13}N_1 - R_{31}N_3 - A_{32}N_3\end{aligned}\tag{3-1}$$

We now consider the steady state regime where the populations are time invariant. From equations (3-1) we can get steady state solutions

$$\begin{aligned}N_1 &= \rho \frac{ab}{b(a + R_{13}) + aW_{12} + R_{13}A_{32}} \\ N_2 &= \rho \frac{R_{13}A_{32} + aW_{12}}{b(a + R_{13}) + aW_{12} + R_{13}A_{32}}\end{aligned}\tag{3-2}$$

where $\rho = N_1 + N_2 + N_3$; $a = R_{31} + A_{32}$ and $b = W_{21} + A_{21}$.

When a signal light beam with intensity I_s (power per area) at wavelength λ_s traverses a slice of laser medium of infinitesimal thickness dz and atomic population density N_1 (lower level) and N_2 (upper level), the intensity change dI_s is given by

$$dI_s = \left\{ \sigma_{21}(\lambda_s)N_2 - \sigma_{12}(\lambda_s)N_1 \right\} I_s dz\tag{3-3}$$

where $\sigma_{12}(\lambda_s)$ and $\sigma_{21}(\lambda_s)$ are the absorption and emission cross sections of the laser transition at λ_s , respectively. So gain g

$$g = \rho \left\{ \sigma_e(\lambda_s)(1 + D) - \sigma_a(\lambda_s)(1 - D) \right\} / 2\tag{3-4}$$

where $D = (N_2 - N_1)/\rho = (2N_2 - \rho)/\rho$, with $D = -1$ when all the laser ions are in the ground state; and $D = 1$ when they are all in the excited state.

As for $\sigma_e(\lambda_s)$ and $\sigma_a(\lambda_s)$ generally we can measure them by experiment data as well as McCumber relation,

$$\sigma_a(\nu) = \sigma_e(\nu) \exp\left\{\frac{h(\nu - \varepsilon)}{k_B T}\right\} \quad (3-5)$$

where $h\varepsilon$ represents the net thermodynamical free energy ΔF required to move one rare earth ion from the ground state to an excited state, while maintaining the lattice temperature T constant. With peak value of $\sigma_a(\lambda_s=1.53\mu\text{m})=7\text{e-}25 \text{ m}^2$ and $\sigma_e(\lambda_s=1.53\mu\text{m}) = 0.92\sigma_a(\lambda_s=1.53\mu\text{m})$. the Er^{3+} density is assumed to be $\rho=1\text{e}25 \text{ m}^{-3}$.

As for the pump power and signal power along the fiber we can use the following coupled differential equation to describe [Saleh, 1990].

$$\begin{aligned} \frac{dP_p^\pm(z,t)}{dz} &= \mp P_p^\pm \Gamma_p (\sigma_{pa} N_1 - \sigma_{pe2} N_2 - \sigma_{pe} N_3) \mp \alpha_p P_p^\pm \\ \frac{dP_s(z,t)}{dz} &= P_s \Gamma_s (\sigma_{se} N_2 - \sigma_{sa} N_1) - \alpha_s P_s \\ \frac{dP_a^\pm(z,t)}{dz} &= \pm P_a^\pm \Gamma_s (\sigma_{se} N_2 - \sigma_{sa} N_1) \pm 2\sigma_{se} N_2 \Gamma_s h\nu_s \Delta\nu \mp \alpha_s P_a^\pm \end{aligned} \quad (3-6)$$

The cross sections are σ , the loss term α represent internal loss of the amplifier, Γ are signal-to-core overlap and pump-to-core overlap.

Equations (3-1) through (3-6) can be called numerical model of EDFA developed by E. Densurvire et al.

There is another popular model developed by Saleh et al. [Giles, 1991] The simplified version should be [Calvez, 2001].

$$Q_k^{out} = Q_k^{in} \exp\left\{\frac{(\alpha_k + g_k^*)}{\zeta} (Q^{in} - Q^{out}) - \alpha_k L\right\} \quad (3-7)$$

$$Q_k^{out} = \sum_k Q_k^{in} \exp\left\{\frac{(\alpha_n + g_k^*)}{\zeta} (Q^{in} - Q^{out}) - \alpha_k L\right\} \quad (3-8)$$

Where photon flux $Q_k = P_k / h\nu_k$.

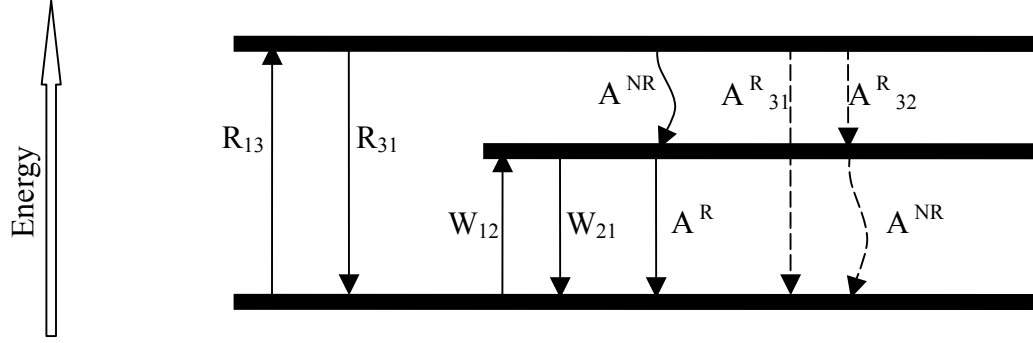


Fig. 3-1. Energy level diagram corresponding to a basic three-level laser system, where the laser transition occurs between levels 1 (ground) and 2 (metastable). The symbols R, W and A correspond to pumping rates, stimulated emission rates and spontaneous decay rates between related levels; superscripts R and NR refer to radiative and nonradiative emission, respectively.

3.2. Simulation results and discussion

We used equations (3-4), (3-5) to plot the gain coefficient vs. wavelength at different D in Fig. 3-2. It can be seen from the figure that for $D = -1$ all ions are in the ground state and the medium is absorbing at all signal wavelengths, as the gain is negative. As the relative inversion increases, however, a spectral region near the long wavelength side of the transition is characterized by a positive gain coefficient. For these wavelengths, the medium is amplifying, while for the rest of the spectrum, the medium is still absorbing. As D increases toward the maximum value, representing complete medium inversion, the region of positive gain coefficient widens to spread eventually over the whole spectral range.

Using equations (3-7) and (3-8) we simulated gain vs. fiber length and pump power that are shown in Figure 3-3 and 3-4 respectively.

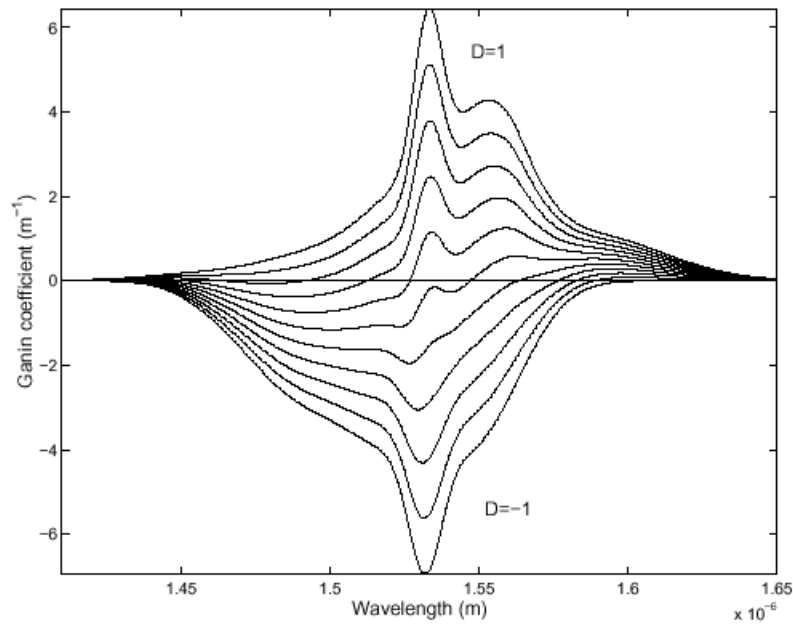


Fig. 3-2. Signal gain coefficient as a function of wavelength for different relative medium inversion D

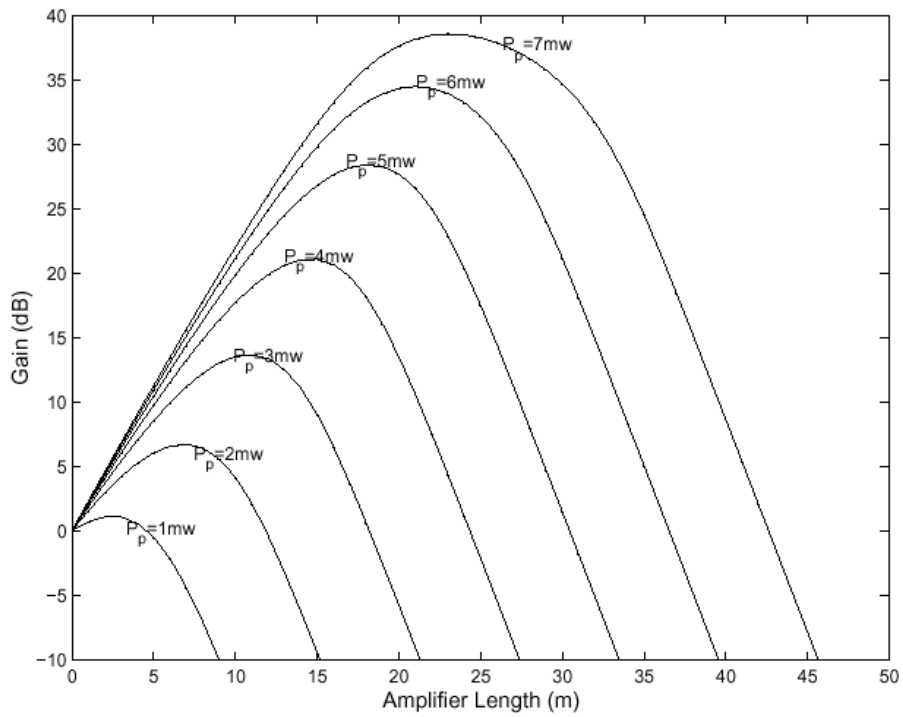


Fig. 3-3. Simulation results of gain vs. amplifier length under different pump powers

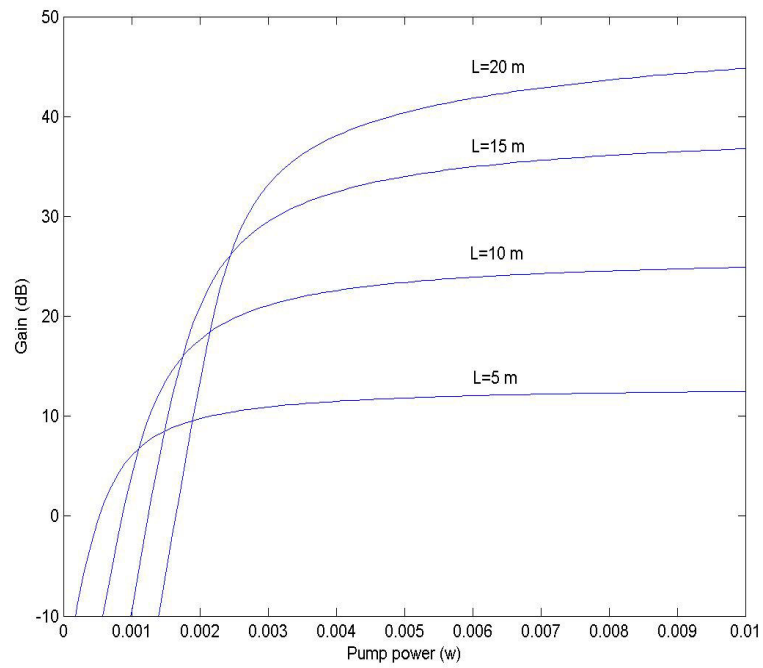


Fig. 3-4. Simulation result of gain vs. pump power under different amplifier lengths

CHAPTER IV

MODELING AND SIMUALTION OF RAMAN AMPLIFIER

4.1. Model description and simulation results

4.1.1. Forward pumping

The interaction between pumping source and signal wave can be described by following coupled equations [Agrawal, 2001]:

$$\frac{dI_p}{dz} = -\alpha_p I_p - \frac{\lambda_s}{\lambda_p} g_R(\lambda) I_p I_s \quad (4-1)$$

$$\frac{dI_s}{dz} = -\alpha_s I_s + g_R(\lambda) I_p I_s \quad (4-2)$$

Where I_p is the pump intensity, I_s is the signal intensity, $g_R(\lambda)$ is the Raman gain coefficient (material dependent), α_s and α_p are the losses at the signal and pump wavelengths. In general, $g_R(\lambda)$ depends on composition of the fiber core and can vary significantly using different dopants.

Decompose the intensities into axial and radial components

$$I = I^{rad}(r, \theta) \bullet I^{ax}(z) \quad (4-3)$$

So the optical power can be expressed as:

$$P(z) = 2\pi \int_0^\infty I(r, z) r dr = \langle I(r, z) \rangle \quad (4-4)$$

Integrate differential equations over the transverse dimensions:

$$\frac{dP_p}{dz} = -\alpha_p P_p - \frac{\lambda_s}{\lambda_p} \frac{g_R(\lambda)}{A_{eff}^R} P_p P_s \quad (4-5)$$

$$\frac{dP_s}{dz} = -\alpha_s P_s + \frac{g_R(\lambda)}{A_{eff}^R} P_p P_s \quad (4-6)$$

where

$$A_{eff}^R = \frac{\langle I_p^{rad} \rangle \cdot \langle I_s^{rad} \rangle}{\langle I_p^{rad} I_s^{rad} \rangle}$$

Assume pump depletion due to the stimulated process is negligible we have

$$\frac{dP_p}{dz} = -\alpha_p P_p \quad (4-7)$$

so

$$P_p = P_p(0)e^{-\alpha_p z} \quad (4-8)$$

$$\frac{dP_s}{dz} = -\alpha_s P_s + \frac{g_R(\lambda)}{A_{eff}^R} [P_p(0)e^{-\alpha_p z}] P_s \quad (4-9)$$

We integrated P_s over z

$$P_s(L) = P_s(0) \exp \left[\frac{g_R(\lambda)}{A_{eff}^R} P_p(0) L_{eff} - \alpha_s L \right] \quad (4-10)$$

where $L_{eff} = \frac{1}{\alpha_p} (1 - e^{-\alpha_p L})$ is the effective length.

I directly solved the coupled ordinary differential equations numerically. The calculation results are shown in Fig 4-1.

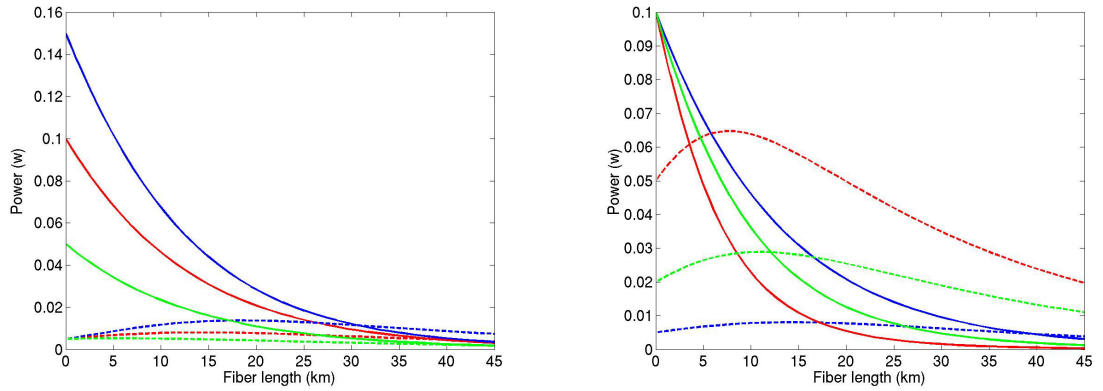


Fig 4-1. Simulation results of different input pump (left) and signal (right) power evolution in forward pumping DRA

4.1.2.Backward pumping

The differential equations for a backward traveling wave of the signal is given by [Mochizuki, 1985]

$$\frac{dP_s(z)}{dz} = [\gamma S_p(z) - \alpha_s] \cdot P_s(z) + \gamma \cdot h \nu_s \cdot S_p(z) \quad (4-11)$$

where

$$S_p(z) = \frac{P_p(L)}{S} \cdot \exp[\alpha_p(z - L)] \quad (4-12)$$

where $P_{s/p}$ is the signal/pump power. $S_{s/p} = P_{s/p}/S$ is the effective power. γ is the gain constant.

If neglect $\gamma \cdot h \nu_s \cdot S_p(z)$ term we can solve the function analytically and the solution is given by

$$P_s(z) = P_s(0) \exp \left\{ \frac{\gamma \cdot P_p(L)}{S \cdot \alpha_p} \cdot \exp(-\alpha_p L) \cdot [\exp(\alpha_p z) - 1] - \alpha_s z \right\} \quad (4-13)$$

Alternatively we can solve it numerically. Fig 4-2 shown the simulation results.

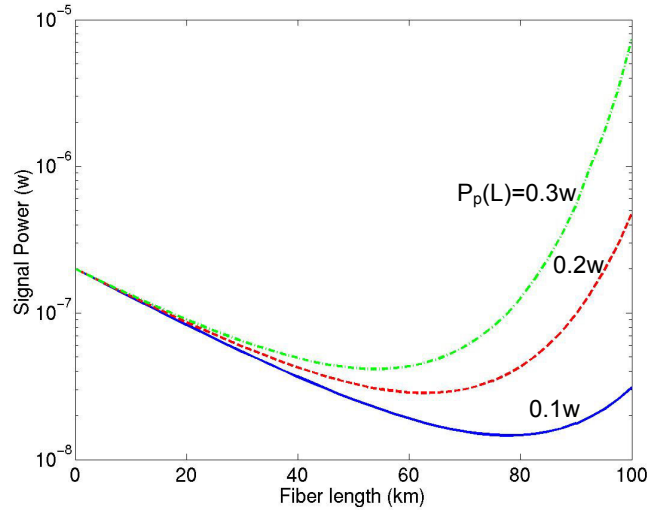


Fig 4-2. simulation results of different pumping input of backward pumping DRA

4.1.3. Bidirectional pumping

The models mentioned before are all uncompleted since many factors that must be considered in DRA design were neglected. They include double Rayleigh scattering (DRS), spontaneous Raman scattering. The most complete model for RA design is given by [Kidorf, 1999]. The following effects were included along with the capability of modeling any number of signals and pumps [Kidorf, 1999]:

- Spontaneous Raman emission and its temperature dependence;
- Rayleigh scattering including multiple directions;
- Stimulated Raman scattering;
- Amplification of the above;
- Arbitrary interaction between an unlimited number of pumps and signals from either direction: Pump–pump, pump–signal, and signal–signal interactions;
- High-order Stokes generation;
- Combinations of multiple fiber types, filters, isolators, etc., within a span.

The effects that were excluded are: anti-Stokes generation, polarization effects, time dependence, and nonlinear index effects. The computer model is given by following equations

$$\begin{aligned}
 \frac{dP^{\pm}(z, \nu)}{dz} = & \mp \alpha(\nu) P^{\pm}(z, \nu) \pm \gamma(\nu) P^{\mp}(z, \nu) \pm \sum_{\varsigma > \nu} \left\{ \frac{g_r(\nu - \varsigma)}{K_{eff} A_{eff}} \cdot [P^{\pm}(z, \varsigma) + P^{\mp}(z, \varsigma)] \cdot P^{\pm}(z, \nu) \right. \\
 & + h\nu \frac{g_r(\nu - \varsigma)}{A_{eff}} \cdot [P^{\pm}(z, \varsigma) + P^{\mp}(z, \varsigma)] \cdot \left[1 + \frac{1}{e^{h(\varsigma - \nu)/KT} - 1} \right] \cdot d\nu \} \\
 & \mp \sum_{\varsigma > \nu} \left\{ \frac{g_r(\nu - \varsigma)}{K_{eff} A_{eff}} \cdot [P^{\pm}(z, \varsigma) + P^{\mp}(z, \varsigma)] \cdot P^{\pm}(z, \nu) \right. \\
 & + 2h\varsigma \frac{g_r(\nu - \varsigma)}{A_{eff}} \cdot P^{\pm}(z, \nu) \cdot \left[1 + \frac{1}{e^{h(\nu - \varsigma)/KT} - 1} \right] \cdot d\varsigma \}
 \end{aligned} \tag{4-14}$$

In this equation (+) is refer to forward propagation direction and (-) is refer to backward propagation direction. $P_f(z, \nu)$ and $P_b(z, \nu)$ are forward propagation power backward propagation power. $\alpha(\nu)$ is the optical attenuation and $\gamma(\nu)$ is the Rayleigh scattering coefficient at frequency ν , h is the Plank's constant, k is the Boltzmann's constant, and T is the temperature of the fiber.

The simplest case is the DRA compose of one forward pumping source, one backward pumping source and one signal wave. The simulation result is shown in Fig 4-3

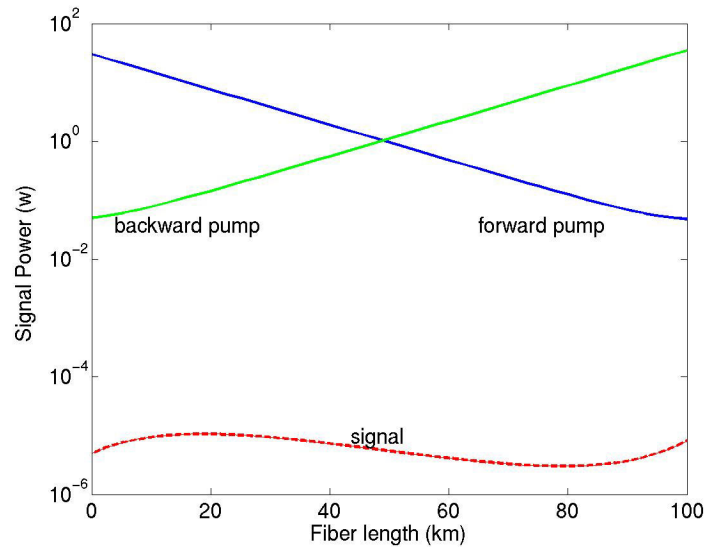


Fig 4-3. Simulation result of a bi-directional pumping DRA

Reference:

Agrawal, Govind P. (2001), *Nonlinear Fiber Optics, Third Edition*, Academic press, 2001

Aliberti, K. (2002), M. Wraback, M. Stead, P. Newman, and H. Shen, “Measurements of InGaAs metal-semiconductor-metal photodetectors under high-illumination conditions”, *Applied Physics letters*, vol. 80, No. 16, pp. 2848, 2002

Calvez, S. (2001), X. Rejeaunier, P. Mollier, J. –P. Goedgebuer and W. T. Rhodes, “Erbium-Doped Fiber Laser Tuning Using Two Cascaded Unbalanced Mach-Zehnder Interferometers as Intracavity Filter: Numerical Analysis and Experimental Confirmation”, *Journal of lightwave technology*, Vol. 19, No.6, June 2001, pp. 893

Chen, Leonard P. (1997), Melissa Y. Li, Connie J. Chang-Hasnain and Kam Y. Lau, "A low-power 1-Gb/s CMOS laser driver for a zero-biased modulated optical transmitter", *IEEE Photon. Technol. Lett*, vol.9, pp 997-999, July, 1997.

Desurvire, E (1996), “An Explicit Analytical Solution for the Transcendental Equation Describing Saturated Erbium-Doped Fiber Amplifiers”, *Optical Fiber Technology*, Vol. 2, 1996, pp. 367-377

Giles, C.Randy (1991) and Desurvire, E, “Propagation of Signal and Noise in Concatenated Erbium-Doped Fiber Optical Amplifiers”, *Journal of lightwave technology*, Vol. 9, No. 2, 1991, pp. 147

Giles, C.Randy (1991) and Desurvire, E, “Modeling Erbium-Doped Fiber Amplifiers”, *Journal of lightwave technology*, Vol. 9, No. 2, 1991, pp. 271

- Gustavsson, Johan S. (2002), A. Haglund, Jorgen Bengtsson, and Anders Larsson, "High-speed digital modulation characteristics of Oxide-confined vertical-cavity surface-emitting lasers--numerical simulations consistent with experimental results", *IEEE J. Quantum Electron*, vol.38, pp 1089-1096, Aug., 2002
- Saleh, A.A.M (1990), R. M. Jopson, J. D. Evankow, and J. Aspell, "Modeling of gain in erbium-doped single-mode fiber amplifiers," *IEEE Photon. Technol. Lett.*, Oct. 1990
- Iga, K. (1988), F. Koyama, and S. Kinshita, "Surface Emitting Semiconductor Lasers", *IEEE J. Quantum Electron*, vol.24, pp 1845-4855, Sept, 1988.
- Kidorf, H. (1999), K. Rottwitt, M. Nissov, M. Ma, and E. Rabarijaona, "Pump interactions in 100 nm bandwidth Raman amplifier," *IEEE Photon. Technol. Lett.*, vol. 11, pp 530-532, May 1999.
- Krishnamurthy, V. (2000), M. C. Hargis, and M.R. Melloch, "A 4-GHz Large-Area (160000 μm^2) MSM-PD on ITG-GaAs", *IEEE photonics technology letters*, vol. 12, No. 1, pp. 71, 2000
- Lauridsen, V. (1991), R. Tadayoni, A. Bjarklev, J. H. Povlsen and B. Pedersen, "Gain and noise performance of fiber amplifiers operating in new pump configurations", *Electron. Lett.*, vol 27, No. 4, 1991, pp. 327
- Man, W. M. (1998) and S. F. Yu, "Comprehensive modeling of diffused quantum-well vertical-cavity surface-emitting lasers", *IEEE J. Select. Topics Quantum Electron*, vol.4, pp 715-722, July/Aug, 1998.
- Mena, P. V. (1999), J. J. Morikuni, S. M. Kang, A. V. Harton and K. W. Wyatt, "A comprehensive circuit-level model of vertical-cavity surface-emitting lasers", *J. of Lightwave Technology*, vol 17, no. 12, 1999
- Mena, P. V. (1999), J. J. Morikuni, S. M. Kang, A. V. Harton, and K. W. Wyatt, "A simple rate-equation-based thermal VCSEL model", *J. Lightwave Technol.*, vol.17, pp 865-872, 1999.
- Mochizuki, Kiyofumi (1985), "Optical Fiber Transmission Systems Using Stimulated Raman Scattering: Theory", *J. of Lightwave Technol.*, vol LT-3, No 3, pp. 688-694, 1985
- Roudas, I. (1999), D. H. Richards, N. Antoniadis, J.L. Jackel and R. E. Wagner "An Efficient Simulation Model of the Erbium-Doped Fiber for the Study of Multiwavelength Optical Networks", *Optical Fiber Technology*, Vol. 5, 1999, pp. 363-389
- Sano, E (1990), "A Device Model for Metal-Semiconductor-Metal Photodetectors and its Applications to Optoelectronic Integrated Circuit Simulation", *IEEE Trans. On Electron Devices*, vol. 37, No.9, pp 1964, 1990

Selvakennedy, S. (1999), M.A. Mahdi, M.K. Abdullah, P. Poopalan, H. Ahmad, “Design optimization of erbium-doped fiber ring laser through numerical simulation”, *Optics Communications*, 170 (1999), pp. 247-253

SMASH User Manual Dolphin Integration, June, 2002

Sze, S M (1971), Coleman D J, Loya J R and Loya A “Current transport in metal–semiconductor–metal (MSM) structures”, *Solid-State Electron.*, vol. 14, pp.1209–18, 1971

Sze, S M (1981), *Physics of Semiconductor Devices* 2nd edition, (New York: Wiley), 1981